

## INFORMATION TO USERS

This manuscript has been reproduced from the microfilm master. UMI films the text directly from the original or copy submitted. Thus, some thesis and dissertation copies are in typewriter face, while others may be from any type of computer printer.

**The quality of this reproduction is dependent upon the quality of the copy submitted.** Broken or indistinct print, colored or poor quality illustrations and photographs, print bleedthrough, substandard margins, and improper alignment can adversely affect reproduction.

In the unlikely event that the author did not send UMI a complete manuscript and there are missing pages, these will be noted. Also, if unauthorized copyright material had to be removed, a note will indicate the deletion.

Oversize materials (e.g., maps, drawings, charts) are reproduced by sectioning the original, beginning at the upper left-hand corner and continuing from left to right in equal sections with small overlaps. Each original is also photographed in one exposure and is included in reduced form at the back of the book.

Photographs included in the original manuscript have been reproduced xerographically in this copy. Higher quality 6" x 9" black and white photographic prints are available for any photographs or illustrations appearing in this copy for an additional charge. Contact UMI directly to order.

# U·M·I

University Microfilms International  
A Bell & Howell Information Company  
300 North Zeeb Road, Ann Arbor, MI 48106-1346 USA  
313 761-4700 800 521-0600



**Order Number 9215866**

**Sensitivity and noise analysis of solenoidal coils for nuclear  
magnetic resonance microscopy**

**Peck, Timothy L., Ph.D.**

**University of Illinois at Urbana-Champaign, 1992**

**U·M·I**  
300 N. Zeeb Rd.  
Ann Arbor, MI 48106



**SENSITIVITY AND NOISE ANALYSIS  
OF SOLENOIDAL COILS  
FOR NUCLEAR MAGNETIC RESONANCE MICROSCOPY**

**BY**

**TIMOTHY L. PECK**

**B.S., Rochester Institute of Technology, 1986  
M.S., University of Illinois, 1988**

**THESIS**

**Submitted in partial fulfillment of the requirements  
for the degree of Doctor of Philosophy in Electrical Engineering  
in the Graduate College of the  
University of Illinois at Urbana-Champaign, 1992**

**Urbana, Illinois**

UNIVERSITY OF ILLINOIS AT URBANA-CHAMPAIGN

THE GRADUATE COLLEGE

DECEMBER 1991

WE HEREBY RECOMMEND THAT THE THESIS BY

TIMOTHY L. PECK

ENTITLED SENSITIVITY AND NOISE ANALYSIS OF SOLENOIDAL COILS

FOR NUCLEAR MAGNETIC RESONANCE MICROSCOPY

BE ACCEPTED IN PARTIAL FULFILLMENT OF THE REQUIREMENTS FOR

THE DEGREE OF DOCTOR OF PHILOSOPHY

*Richard L. Magin*

Director of Thesis Research

*Timothy M. Crick*

Head of Department

Committee on Final Examination†

*Richard L. Magin*

Chairperson

*Paul C. Lauterborn*

*J. J. Franke*

*Bruce C. Wheeler*

† Required for doctor's degree but not for master's

# SENSITIVITY AND NOISE ANALYSIS OF SOLENOIDAL COILS FOR NUCLEAR MAGNETIC RESONANCE MICROSCOPY

Timothy L. Peck, Ph.D.  
Department of Electrical and Computer Engineering  
University of Illinois at Urbana-Champaign, 1992  
R. Magin, Advisor

Conventional NMR studies involve sample volumes ( $v_s$ ) of several cubic millimeters and greater. Much recent interest is directed at the development of microscopic NMR systems for the analysis of smaller samples and the visualization of microscopic biological structures. The objective of the research summarized in this thesis is to extend the analysis of RF coils used for NMR to microscopic domains. Microscopic nuclear magnetic resonance suffers from an inherently low SNR, due to the small number of nuclei available to contribute to the signal. Decreasing the size of the RF receive coil provides better coupling between the sample being examined and the coil, i.e., it increases the sensitivity of the coil. We define the sensitivity of a coil as the magnitude of the RF magnetic field that is produced in the coil when a unit current is passed through the windings of the coil.

However, the sensitivity of the coil to detect signals is not the only consideration when determining the SNR, as the noise must also be considered. Noise originates primarily from the resistance of the coil. Electrical circuit models used to characterize large coils (diameters  $\geq 1$  mm) cannot be used for smaller coils, in which the wire diameter approaches one skin depth at the frequency of operation. Therefore, we extend the electrical circuit models which represent the coil to microscopic domains to characterize accurately the SNR performance of RF coils for submillimeter NMR. It is clear from our results that the loss in microcoils can be characterized accurately and that an accurate calculation of the SNR using microcoils can be achieved. Furthermore, the results demonstrate that an enhanced SNR can be achieved in NMR with microcoils as small as 38  $\mu\text{m}$ , and support the continued reduction of coil size for further enhancement in the SNR.

## ACKNOWLEDGEMENTS

The completion of this endeavor would not have been possible without the assistance and support of my family, friends, and the staff at the University of Illinois. I wish to extend a very special appreciation to Professor Richard Magin, for being a true advisor – for having enough confidence in me to permit me to fail occasionally, and for helping me to pursue my professional career without compromising my values. Special thanks go also to my Ph.D. committee: Professors Paul Lauterbur, Steve Franke, and Bruce Wheeler. Each of the committee members provided me with unlimited access to their laboratories and instrumentation, and willingly provided guidance when needed. I am grateful to Professor Lauterbur for proposing this study as a possible thesis topic.

I also wish to acknowledge the support of the staff of the Bioacoustic Research Laboratory: Billy McNeil for designing and building much of the instrumentation necessary to complete these experiments, Bob Cicone for providing computer resources, and Wanda Elliot for giving day-to-day direction and for making sure that all of the individual personalities of the laboratory functioned as a whole.

I am especially grateful to my wife Kim. It was her encouragement and emotional support, and her willingness to care for our new daughter by herself on many evenings while I was at the laboratory, that enabled me to complete my degree. This has represented a deeper statement of her love for me than mere words could say.

Finally, I want to thank my Father for His gift of life in our home, in the form of our daughter Leah, and for the way in which He has consistently provided for our needs.

## TABLE OF CONTENTS

	Page
1. INTRODUCTION.....	1
2. THEORY.....	4
2.1 Review of Classical NMR.....	4
2.2 Signal and Noise.....	9
2.2.1 Signal.....	9
2.2.2 Noise.....	16
2.2.3 Signal-to-noise ratio.....	60
2.3 Summary.....	66
2.4 References.....	67
3. EXPERIMENTAL METHODS AND RESULTS.....	69
3.1 Background.....	70
3.2 Methods.....	71
3.3 Results.....	71
3.3.1 Empirical verification of wire loss.....	71
3.3.2 Development of a computational model.....	81
3.3.3 Microcoil fabrication.....	84
3.3.4 Electrical testing.....	89
3.3.5 Verification using NMR.....	102
3.4 Summary.....	113
3.5 References.....	115
4. CONCLUSION.....	116
APPENDIX A. SAMPLE NOISE.....	119
A.1 References.....	122
APPENDIX B. ADDITIONAL CONCERNS.....	123
B.1 References.....	128
APPENDIX C. CONSTRUCTION OF MICROCOILS.....	129
C.1 References.....	138
APPENDIX D. MICROCOIL RESISTANCE MEASUREMENT.....	139
D.1 References.....	141
VITA.....	150

## 1. INTRODUCTION

Since its discovery in 1946, nuclear magnetic resonance (NMR) has rapidly advanced as an inter-disciplinary science which employs the principles of chemistry, physics, engineering, medicine, and biology. NMR spectroscopy now constitutes one of the major analytical techniques for elucidation of chemical structure in both the liquid and solid phase. In addition, NMR can also be used to study molecular dynamics, where it serves as a gauge for the measurement of diffusion gradients, perfusion, and other mass transport properties of liquids through porous media. With the addition of magnetic field gradients, NMR provides imaging capabilities, and routinely complements x-ray and ultrasound as diagnostic tools for the clinical radiologist.

Regardless of the particular application, an essential component of any NMR system is the radio-frequency (RF) coil used both to excite the sample and to receive the free induction decay (FID) as the sample magnetization relaxes back to equilibrium. As such, the RF coil can be considered, from an electrical engineering standpoint, to be a near-field antenna. The overall efficiency with which energy is exchanged between the experimental apparatus and the sample is dependent upon the characteristics of the RF coil (size, sensitivity, homogeneity, and noise). An efficient RF coil design is a critical part of an NMR system. For example, in NMR imaging, in which the geometric shape of the sample typically cannot be altered, customized RF coils which *wrap around* and conform to the sample are routinely used to provide an enhanced signal-to-noise ratio (SNR).

Conventional NMR studies involve sample volumes ( $v_s$ ) of several cubic millimeters and greater. Much recent interest is directed at the development of microscopic NMR systems for the analysis of smaller samples and the visualization of microscopic biological structures. The objective of the research summarized in this thesis is to extend the analysis of RF coils used for NMR to microscopic domains. Microscopic nuclear magnetic resonance suffers from an inherently low SNR, due to the small number of nuclei available to contribute to the signal. Decreasing the size of the RF receive coil provides better coupling between the sample being examined and the coil, i.e., it increases the sensitivity of the coil. We define the sensitivity of a coil as the magnitude of the RF magnetic field

that is produced in the coil when a unit current is passed through the windings of the coil. Of the common coil geometries used for NMR (e.g., saddle, birdcage, and solenoidal), solenoidal coils possess the best sensitivity and RF magnetic field homogeneity. Therefore, the coils used in this study are solenoidal coils.

However, the sensitivity of the coil to detect signals is not the only consideration when determining the SNR, as the noise must also be considered. Electrical circuit models are commonly employed to assist in characterizing signal detection for a given coil design and in determining the associated coil noise. These models are dependent on many factors, including the frequency of operation and the size of the wire used in winding the coil, and care must be exercised in choosing the proper model for a particular application. Traditional *macroscopic* models used to characterize large coils (diameters  $\geq 1$  mm) cannot be used for smaller coils, in which the wire diameter approaches one skin depth at the frequency of operation. Furthermore, the local electromagnetic field interaction between adjacent wires leads to an increase in the resistance of the coil and further complicates the model. For example, macroscopic models of RF coils are not able to characterize accurately the *proximity effect* for smaller coils.

Therefore, in this study we will extend the electrical circuit models which represent the coil to microscopic domains to characterize accurately the SNR performance of RF coils for submillimeter NMR. We classify RF coils with submillimeter diameters as "microdomain coils" or simply "microcoils." The design of microcoils is particularly aimed at both NMR spectroscopy and imaging applications. It should be clear from our results that the loss in microcoils can be characterized accurately and that an accurate calculation of the SNR using microcoils can be achieved. The results for a particular coil are dependent on its size and geometry, its frequency of operation, and the size of the wire used in winding the coil. We develop and test a quantitative theory that accurately predicts the interaction of these factors for microscopic NMR coils.

This study begins with an overview of NMR, including the development of the necessary mathematical framework. The signal and noise inherent in an NMR microscopy experiment are derived in Chapter 2. The sensitivity of solenoidal coils is well-defined, and the magnitude of the

received signal is readily calculated using well-established formulae. The noise, however, is not as well-understood. Therefore, models are developed to assist in the characterization of noise in microcoils. It is shown that special scaling laws apply which permit the noise characterization of larger coils at lower frequencies to be applied to microcoils at RF. Chapter 2 concludes with the theoretical equations representing the SNR that can be expected in NMR microscopy using microcoils. The results clearly demonstrate that microcoils provide an enhanced SNR (over that of larger coils) for microscopic NMR. Chapter 3 provides details of microcoil fabrication, testing, and verification. The resistance, inductance, and other electrical parameters of the microcoils are compared with the theoretical predictions. Chapter 3 concludes with a comparison of the SNR achieved using the microcoils for spectroscopic NMR at 200 MHz and the expected SNR calculated using the microcoil resistance models from Chapter 2. It should be clear that an improvement in the signal-to-noise ratio in NMR experiments is achieved using microcoils. Furthermore, the empirical results show good agreement with the theoretically calculated SNR and support the validity of the models used to represent the coil noise.

## 2. THEORY

Chapter 2 provides the theoretical basis for calculating the signal and noise intensities in an NMR experiment. In particular, it shows that approximations used in the derivation of noise for larger coils are not strictly valid for microcoils, and that careful consideration of these approximations must be made so as not to obtain misleading results. In Section 2.1, a general overview of the NMR phenomenon is presented. The equations which represent the signal and noise in an NMR experiment are derived in Section 2.2. The critical parameter of interest in determining the signal intensity is the sensitivity of the microcoil. This is determined using the expression for the magnetic field of a solenoidal coil at larger dimensions, and remains valid for microcoils, regardless of the exact form of the current distribution in the windings of the microcoil, due to the inherent symmetry afforded by the cylindrical geometry of the solenoid. The critical parameter of interest in determining the intensity of the noise is the resistance (i.e., loss) of the microcoil. This parameter is of particular concern, since the noise from the sample is insignificant in the size regime considered in this study. Models used to calculate the loss in larger coils cannot be applied to microcoils. Alternative models are developed which represent accurately the loss in microcoils, and are given in terms of a scaling parameter which permits the results to be applied to any microcoil, regardless of the coil size or intended frequency of operation. The results of Chapter 2 demonstrate that enhanced signal-to-noise ratios can be achieved by using microcoils when examining small sample volumes with NMR.

### 2.1 Review of Classical NMR

The reaction of a charged particle with a magnetic moment  $\mathbf{m}$  and angular momentum  $\mathbf{J}$ , when immersed in an external magnetic field  $\mathbf{B}_0$  is to attempt to align  $\mathbf{m}$  with  $\mathbf{B}_0$ . (In the remainder of this thesis,  $\mathbf{B}$  and  $\mathbf{H}$  are used somewhat interchangeably to represent the magnetic field.) The magnetic flux density is represented by  $\mathbf{B}$  (Wb/m<sup>2</sup>, or T) and  $\mathbf{H}$  represents magnetic field intensity (A/m), the two being related by the permeability  $\mu$  of the medium through which the magnetic field threads,

$B = \mu H$ . The value of permeability in free space is  $\mu_0 = 4\pi \times 10^{-7}$  (H/m). The angular momentum  $J$  will cause the spin axis of the particle to move in a direction perpendicular to the plane defined by the vectors  $m$  and  $B_0$ , resulting in a circular motion about the axis of the field  $B_0$ . This phenomenon is known as precession, and it is not confined to magnetic systems, with perhaps the most common example being the circular motion of a spinning top as it tries to align with the earth's gravitational field as shown in Figure 1.

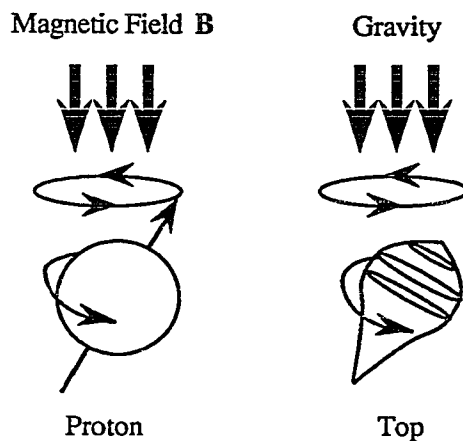


Figure 1 Precession.

In the absence of an externally applied magnetic field, the individual magnetic moments in a sample composed of such particles are equally distributed, with half oriented "spin up" and half oriented "spin down" as shown in Figure 2. The two spin states are said to be *degenerate*, that is, of equal energy. In an NMR spectroscopy or imaging experiment, the sample is immersed in an external, homogeneous, high strength static magnetic field  $B_0$  (typically 0.1 T - 10 T in magnitude). Those nuclei within the sample which have a net magnetic moment try to align with  $B_0$ , and a natural precession occurs analogous to that shown in Figure 1. The frequency ( $\omega_0$ ) at which the precession occurs is proportional to the magnitude of the static field,  $\omega_0 = -\gamma B_0$ , the constant of proportionality ( $\gamma$ ) being the gyromagnetic ratio of the nuclei. This is known as the Larmor equation.

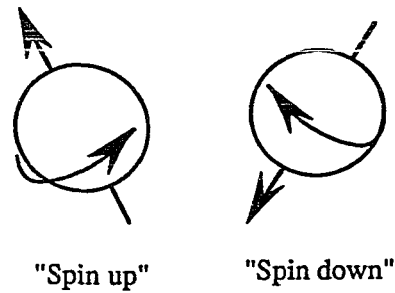


Figure 2 Orientation of magnetic moments in the absence of an external magnetic field.

Macroscopically, the collective magnetic moment of the sample is represented in Figure 3 by the vector  $\mathbf{m}_s$ , and is aligned statically along the  $\mathbf{B}_0$  axis.

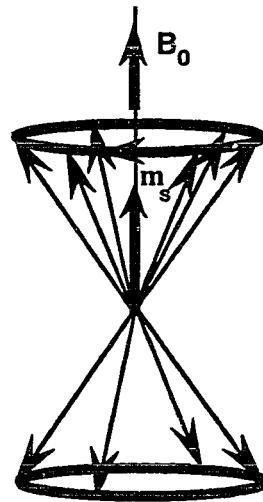


Figure 3 The net magnetic moment of the sample ( $\mathbf{m}_s$ ) when placed in an external, static magnetic field.

The net difference in population of the individual magnetic moments aligned with  $\mathbf{B}_0$  and those aligned against  $\mathbf{B}_0$  is extremely small, typically less than 0.001%. As shown in Figure 3, the individual magnetic moments are randomly distributed around the "cone of precession," and are not phase coherent.

An RF magnetic field ( $\mathbf{B}_1$ ) coil tuned to frequency  $\omega_0$  and directed perpendicular to  $\mathbf{B}_0$  can supply energy to the spin system. As energy is supplied to the system, an increasing number of magnetic moments are "promoted" to an excited state, directed antiparallel to  $\mathbf{B}_0$ . Simultaneously, they become phase coherent as they track the oscillating magnetic field of the RF coil. As shown in Figure 4, the magnetic moments now form a precessing bundle, and the collective magnetic moment  $\mathbf{m}_s$  exhibits a component  $\mathbf{m}_{s_{xy}}$  in the direction perpendicular to  $\mathbf{B}_0$  and a component  $\mathbf{m}_{s_z}$  in the direction of  $\mathbf{B}_0$ . It is the perpendicular component ( $\mathbf{m}_{s_{xy}}$ ) which is aligned with the coil and which can be detected by the coil.

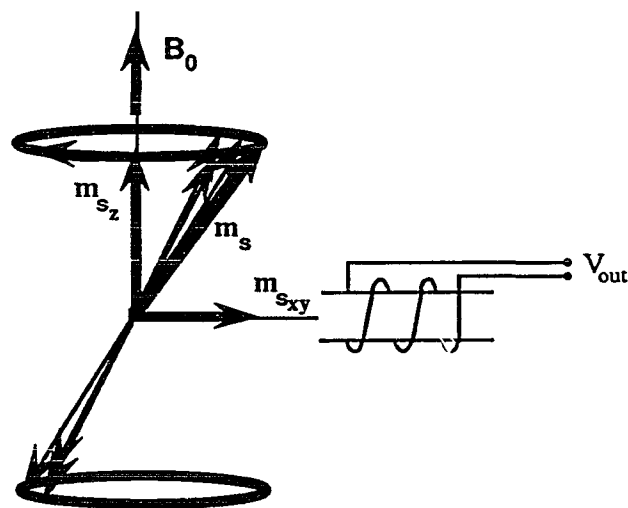


Figure 4 Upon application of the RF magnetic field, the individual magnetic moments of the sample become phase coherent. Simultaneously, the cone of precession will begin to precess about the axis of the RF magnetic field.

Classically, the "promotion" of the magnetic moments to an excited state can be understood by considering the net magnetization vector  $\mathbf{m}_s$ . If viewed from a "rotating frame" in which the coordinate axes of the plane perpendicular to  $\mathbf{B}_0$  are rotating with  $\mathbf{m}_s$  at frequency  $\omega_0$ ,  $\mathbf{m}_s$  begins to precess about the applied RF magnetic field  $\mathbf{B}_1$  (which now appears time invariant), tracing out a circle in a plane perpendicular to the plane defined by  $\mathbf{B}_0$  and  $\mathbf{B}_1$ . In the standard (laboratory) frame,

precession occurs simultaneously about both  $B_0$  and  $B_1$ , and  $m_s$  traces out a "spiral" as shown in Figure 5. As the energy being delivered to the sample by  $B_1$  is increased, the "tip angle" ( $\alpha$ ) representing the inclination of  $m_s$  away from  $B_0$  increases, with  $|m_{s_{xy}}| = |m_s|$  and  $|m_{s_z}| = 0$  when  $\alpha = \pi/2$ .

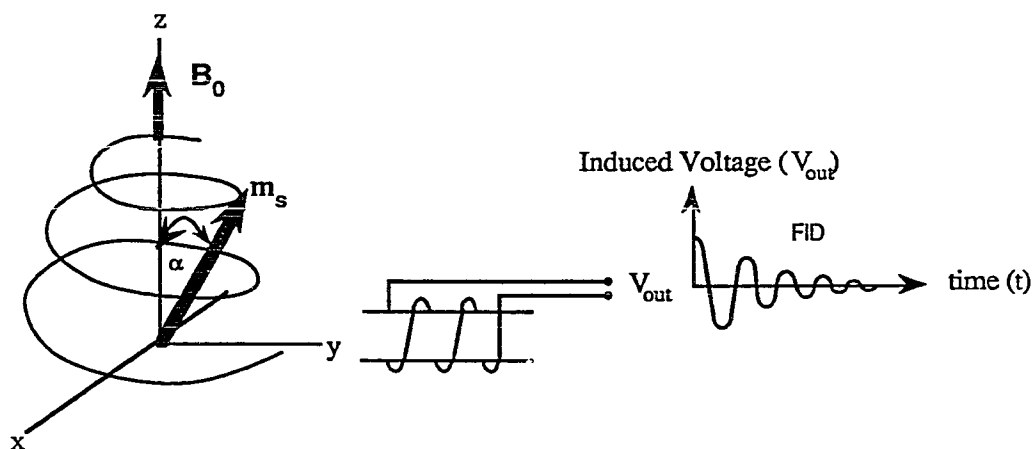


Figure 5 Precession of  $m_s$  as viewed from the laboratory frame of reference.

With the sample in an excited state, the  $B_1$  field is switched off, and the sample magnetization begins to relax back toward equilibrium as governed by the time constants  $T_1$  and  $T_2$ . The time constant associated with the loss of energy to the surroundings as the sample relaxes back toward its equilibrium state is  $T_1$ , whereas  $T_2$  is the time constant governing the dephasing of the individual magnetic moment contributions, i.e., the loss of phase coherence. The RF coil detects  $m_{s_{xy}}$ , which induces a time-harmonic voltage at the terminals of the coil. The complex time-dependent signal induced in the receive coil is called the "free induction decay" (FID), the real part of which is shown in Figure 5. The FID provides information about the molecular structure and dynamics of the nuclear species.

## 2.2 Signal and Noise

### 2.2.1 Signal

Of paramount importance in the NMR experiment is the efficiency with which energy can be exchanged between the excitation magnetic field ( $B_1$ ) and the sample. A standard with which to gauge the overall effectiveness of the experimental system is the SNR. One of the first published derivations of the SNR in an NMR experiment was by Hoult and Richards,<sup>1</sup> in which they considered the noise to be dominated by the Brownian motion of electrons in the receiving antenna coil. Hoult and Lauterbur<sup>2</sup> later expanded this derivation to account for the eddy current losses which result from dielectric coupling between conducting samples and the antenna coil. The derivation of the signal induced in the receiving antenna begins with reaction and reciprocity, electromagnetic principles obtained directly from Maxwell's equations. Maxwell's equations characterize the interaction of the local magnetic field (and flux linkage) throughout the solenoid with the current distribution in the windings, and are given as

$$\begin{aligned}
 \nabla \times \mathbf{H} &= j\omega\mathbf{D} + \mathbf{J} \\
 \nabla \times \mathbf{E} &= -j\omega\mathbf{B} - \mathbf{M} \\
 \nabla \cdot \mathbf{D} &= \rho \\
 \nabla \cdot \mathbf{B} &= 0
 \end{aligned}
 \tag{1}$$

where  $\omega$  is the frequency of interest,  $\mathbf{D} = \epsilon\mathbf{E}$  represents electric flux density ( $C/m^2$ ),  $\mathbf{E}$  represents electric field intensity ( $V/m$ ), and  $\epsilon$  is the permittivity of the medium. The electric and magnetic current densities are represented by  $\mathbf{J}$  and  $\mathbf{M}$ , respectively, and  $\rho$  represents static charge. Consider a time harmonic *source* C, denoted by electric and magnetic currents  $\mathbf{J}_c$  and  $\mathbf{M}_c$ , in an electric and magnetic *field*  $\mathbf{E}_s$  and  $\mathbf{B}_s$  which has been produced by some time harmonic current *source* S, denoted by  $\mathbf{J}_s$  and

$\bar{M}_s$  as shown in Figure 6. The interaction of source c with field s may be characterized by  $\langle c,s \rangle$  where

$$\langle c,s \rangle = \int_{\nu} d\nu (J_c \cdot E_s - M_c \cdot B_s) \quad (2)$$

Note that when either the source or field is zero, the reaction is zero. The integration is over the volume  $\nu$  of the region containing the source c. Reciprocity states that

$$\langle c,s \rangle = \langle s,c \rangle = \int_{\nu'} d\nu' (J_s \cdot E_c - M_s \cdot B_c) \quad (3)$$

for an isotropic medium, where integration is now over the volume  $\nu'$  of the region containing source s.

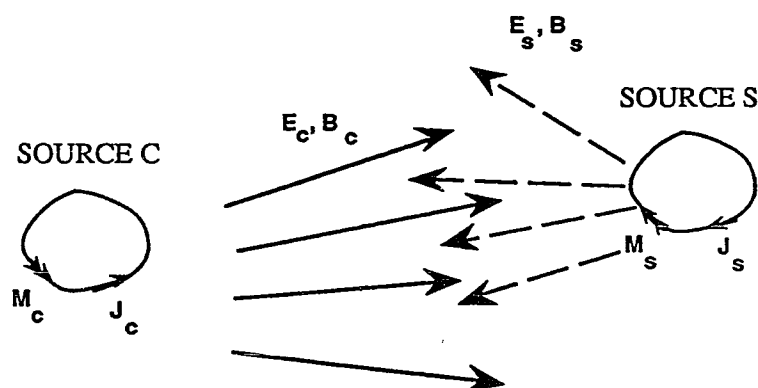


Figure 6 The electric field ( $E$ ) and magnetic field ( $B$ ) produced by sources of electric current ( $J$ ) and magnetic current ( $M$ ).

Applying reaction and reciprocity to NMR, source S represents the magnetic dipole moments with magnetic current  $M_s$ , where  $J_s = 0$  in the sample volume  $\nu$ . The magnetic current produces fields  $E_s$  and  $B_s$ . Source C represents the receive coil ( $B_1$ ) with current  $J_c$  flowing through it

( $M_c = 0$ ), producing fields  $E_c$  and  $B_c$ . The expression for the reaction of the receiving coil to the fields produced by the nuclear magnetic dipoles in the sample can now be calculated. Referring to Eq. (2), this reaction is given by

$$\langle c, s \rangle = \int_V dV (J_c \cdot E_s)$$

where  $M_c = 0$  in the volume  $v$  of the coil region. This calculation would require knowledge of the spatial distribution of the electric field produced at the receiver coil by the nuclear magnetic moments distributed within the sample as well as the value of the electric current induced in the receiver coil, clearly a nontrivial calculation. However, the process is significantly simplified through the use of reciprocity. By reciprocity,

$$\langle c, s \rangle = \langle s, c \rangle = - \int_V dV (M_s \cdot B_c) \quad (4)$$

where now the integration is over the sample volume  $v$  where  $J_s = 0$ . Equation (4) is fundamental to the derivation of the received signal in NMR, and it is important to consider its implications. In simple terms, it says that the reaction of the receiver coil to the field produced by a group of nuclear magnetic moments can be found by first passing a unit current through the coil and measuring the magnetic field  $B_c (= B_1)$  produced in the sample region. In effect, this provides a measure of the sensitivity of the coil to various points in the sample volume. By weighting the magnetic dipole contributions of the nuclei by the coil sensitivity, via the dot product, and integrating over the volume of the sample, the reaction of the receiving coil to the field is obtained. The conventional notation is to represent the density of the magnetic moment (i.e., the magnetization density) by  $M_0$  and the magnetic field (per unit current) in the receiving coil by  $B_1$ .

We have loosely referred to the *reaction* of the receiving coil to the magnetic field produced by the nuclear magnetic moments without defining the physical quantity represented by the reaction. Consider an arbitrary magnetic moment  $\mathbf{m}$  from a single magnetic dipole, represented by a loop of wire carrying unit current ( $I = 1$ ) with cross-sectional area ( $S$ ) as shown in Figure 7. This magnetic dipole will produce lines of magnetic flux given by

$$d\Psi = \int \mathbf{B} \cdot \hat{\mathbf{a}}_m dS = \mathbf{B} \cdot \hat{\mathbf{a}}_m S = \mathbf{B} \cdot \mathbf{m} \quad (5)$$

where  $\mathbf{B}$  is the dipole magnetic field and  $d\Psi$  is the flux of the dipole coupled to itself. One would expect that the introduction of a second magnetic system, e.g., a second loop of wire, would result in some *reaction* between the two systems. From the theory outlined above and simple unit analysis, it is evident that the reaction equation between the two systems is representative of the mutually coupled flux, given by

$$d\Psi = \mathbf{B}_1 \cdot \mathbf{m}$$

where  $\mathbf{B}_1$  is the magnetic field that would be produced by a unit current in the second loop of wire. Generalizing, the reaction of the second (receive) coil to a group of magnetic dipoles is

$$\begin{aligned} \langle c, s \rangle = \langle s, c \rangle = -\Psi &= -\int d\Psi = -\int_{\mathcal{V}} (\mathbf{B}_1 \cdot \mathbf{m}) \\ &= -\int_{\mathcal{V}} (\mathbf{B}_1 \cdot \mathbf{M}_0) \end{aligned}$$

where the individual magnetic dipole moment ( $\mathbf{m}$ ) has been replaced by the collective magnetic moment (per unit volume) of the sample, i.e., the magnetization density ( $\mathbf{M}_0 = \mathbf{m}_s/\mathcal{V}$ ), with  $\mathcal{V}$  being the volume containing the dipole sources shown in Figure 8.

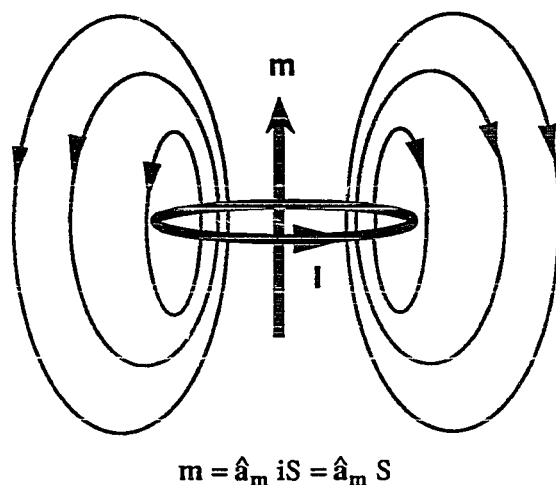


Figure 7 The magnetic field produced by an elemental current loop.

From Faraday's law, the electromotive force (emf) induced in a coil is numerically equal to the negative time rate of change of magnetic flux coupled to the coil. Hence, the emf induced in the receiver coil by tipping the bulk sample magnetization vector into alignment with the coil must be given by

$$\text{emf} = -\frac{d\Psi}{dt} = -\frac{d\langle c, s \rangle}{dt} = -\int_V \frac{d}{dt} (\mathbf{B}_1 \cdot \mathbf{M}_0) dV \quad (6)$$

The amount of energy required from  $\mathbf{B}_1$  to tip the sample magnetization vector by  $90^\circ$ , into alignment with the receive coil, is commonly referred to as a " $\pi/2$  pulse" or " $90^\circ$  pulse." A  $\pi/2$  pulse insures that a maximum value of magnetization is available for detection by the RF coil. An "xy" subscript is attached to the coil magnetic field,  $\mathbf{B}_{1,xy}$ , to signify a transverse oriented RF coil. The peak signal induced in an NMR coil immediately following a  $\pi/2$  pulse is given by Eq. (6), and can be used in the calculation of the signal-to-noise ratio .

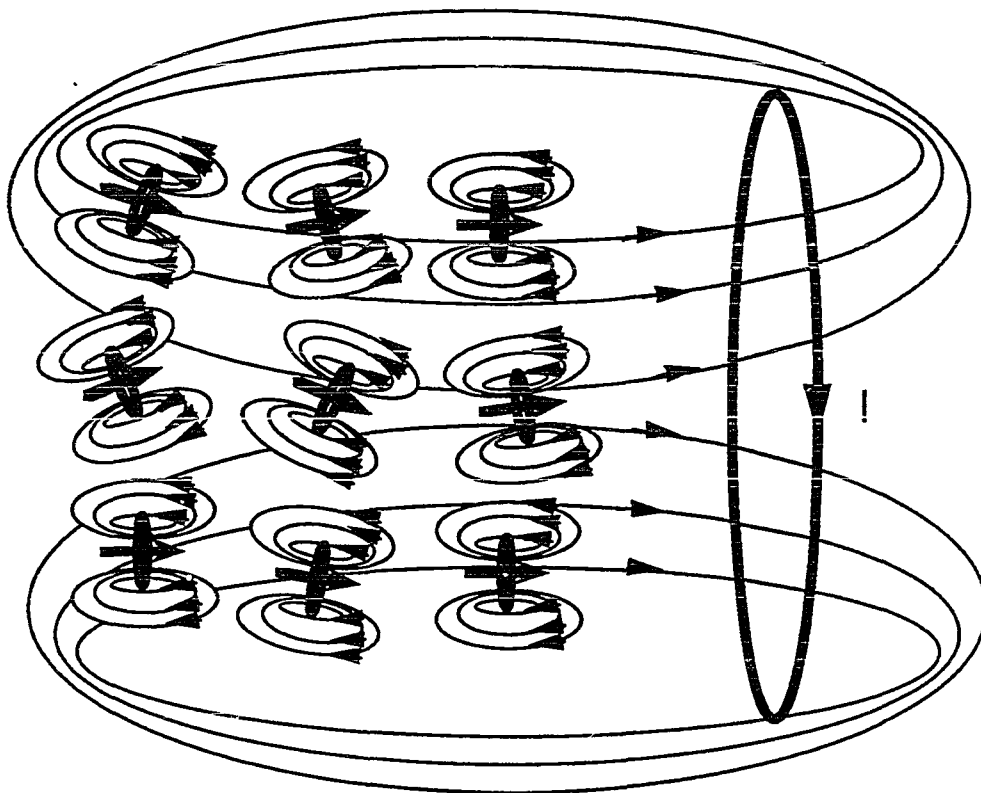


Figure 8 The time rate of change of the magnetic field produced by the individual magnetic dipoles as they relax back toward equilibrium (following excitation) induces a current in the RF receive coil.

Equation (6) can be further simplified. The expression for the equilibrium magnetization,  $M_0$ , is derived using statistical and quantum mechanics and the equipartition theorem. Abragam<sup>3</sup> provides an elegant mathematical derivation of  $M_0$ . Consider the spin populations of the energy levels which result when a sample is placed in static magnetic field  $B_0$ . The number of energy levels ( $q$ ) is dependent upon the value of the nuclear spin quantum number ( $i$ ). The populations of the energy levels ( $P_q$ ) is proportional to

$$P_q = e^{-\frac{E_q}{k_B T_s}} = e^{-\frac{\gamma \hbar q B_0}{k_B T_s}}$$

where the Hamiltonian operator has been used to determine the magnetic energies ( $E_q$ ). The net magnetization ( $M_0$ ) of a sample containing  $N$  nuclear spins per unit volume is therefore

$$M_0 = N\gamma\bar{h} \frac{\sum_{q=-i}^i q e^{-\frac{E_q}{k_B T_s}}}{\Gamma}$$

where

$$\Gamma = \sum_q e^{-\frac{E_q}{k_B T_s}}$$

is the partition function. However, the ratio given by

$$\frac{\gamma\bar{h}B_0}{k_B T_s}$$

is a very small number, much less than 1. Therefore, a linear expansion of the exponential can be performed to yield

$$M_0 = N\gamma\bar{h} \frac{\sum_{q=-i}^i q \left(1 + \frac{\gamma\bar{h}qB_0}{k_B T_s}\right)}{\sum_{q=-i}^i \left(1 + \frac{\gamma\bar{h}qB_0}{k_B T_s}\right)} \cong N\gamma\bar{h} \frac{\sum_{q=-i}^i \frac{\gamma\bar{h}q^2 B_0}{k_B T_s}}{\sum_{q=-i}^i 1} = N \frac{\gamma^2 \bar{h}^2}{k_B T_s} \frac{\sum_{q=-i}^i q^2}{2i+1}$$

Therefore,

$$M_0 = \frac{N \gamma^2 \bar{h}^2 i(i+1) B_0}{3k_B T_s}$$

where  $k_B$  is Boltzmann's constant,  $\hbar = h/2\pi$  is Planck's constant,  $T_s$  is the sample temperature, and  $i$  is the nuclear spin. For most coils,  $B_1$  may be considered to be relatively homogeneous over the volume of interest and can be treated as a constant. Therefore, the signal induced in the receiving coil following excitation of a sample of volume  $v_s$  (and ignoring the effects of relaxation) is given by

$$S(t) = \frac{k_0 B_{1xy} v_s N \bar{\gamma}^2 i(i+1) \omega_0^2}{3k_B T_s} \cos(\omega_0 t) \quad (7)$$

where the time dependence has been reintroduced, the  $90^\circ$  phase shift (from time differentiation) ignored, and only the real part of the complex time function ( $\cos[\omega_0 t] = \text{Re}[e^{i\omega_0 t}]$ ) retained. A factor  $k_0$  has been added to account for inhomogeneity in the  $B_{1xy}$  field, and the Larmor equation has been used to eliminate  $B_0$ .

### 2.2.2 Noise

The contribution of noise to the NMR experiment must be considered. Electric current, electromagnetic radiation, and other seemingly "continuous" quantities in nature have been shown to be composed of large numbers of discrete particles.<sup>4</sup> Each of these discrete particles behaves independently and exhibit random fluctuations in addition to being able to respond to a commonly applied, external stimulus. As the term implies, "random" fluctuations occur regardless of any net particle movement, and therefore represent "noise" to the measurement process. We define noise as any extraneous electrical disturbance tending to interfere with the "desired" measurement of net particle movement, i.e., the signal. Statistical mechanics are employed to assist in characterizing noise, with the two most common calculations being the mean and the variance. The mean is a measure of the statistical average fluctuation, whereas the variance represents the extent to which the individual fluctuations differ from the average value, and is a measure of the dispersion.

There are three common categories into which random noise is grouped: thermal (Johnson) noise, shot noise, and flicker (1/f) noise. Thermal noise is due to the random motion of charge carriers in a conducting medium whose temperature is above absolute zero. Shot noise describes the noise occurring from discrete events, such as the emission of electrons by a thermionic cathode. Flicker noise describes a special category of noise that has a spectral power density that varies inversely with frequency. Typically, the consideration of flicker noise is merited only at frequencies below tens of KHz. In NMR, the noise process is dominated by thermal noise generated in the coil and in the sample. In 1928 Nyquist, using the equipartition law of Boltzmann and Maxwell, derived his expression for the (mean) thermal noise voltage in a resistive circuit using the same method that Rayleigh had used (in 1900) to describe black-body radiation.<sup>4,5</sup> Thermal noise is frequency independent, that is, it has a uniform power spectral density. Nyquist's derivation in terms of the maximum noise power ( $P_{\text{noise}}$ ) available (to a matched load) per unit bandwidth ( $\Delta f$ ) is given as

$$P_{\text{noise}} = \frac{(V_{\text{rms}}^2 / 4R)}{\Delta f} = k_B T$$

where  $R$  is the resistance of the conducting medium and  $T$  is its temperature. Solving for the rms noise voltage,

$$V_{\text{noise}_{\text{rms}}} = \sqrt{4k_B T R \Delta f} \quad (8)$$

In an experiment published in the same journal issue as Nyquist's formula, Johnson quantitatively validated Nyquist's expression for thermal noise in an electrical circuit, and consequently thermal noise is often referred to as "Johnson noise." To assist in the characterization of thermal noise, a Thevenin equivalent circuit model (shown in Figure 9) can be used. In the Thevenin model, the resistance producing the noise is replaced by an ideal voltage source with magnitude equal to the noise voltage

given by Eq. (8). A "noiseless" (ideal) resistor is placed in series with the noise voltage source, from which the amount of thermal noise power delivered to the load may be determined.

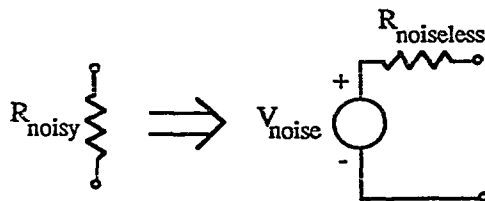


Figure 9 A noise model for a resistor.

The focus of this thesis is submillimeter NMR. It can be shown that the sample-induced noise is negligible relative to the noise inherent to the coil itself when considering biological samples and submillimeter coils.<sup>6</sup> A more detailed look at sample noise is provided in Appendix A. Furthermore, the thermal noise of the coil dominates the other coil noise processes in NMR. Hence, an understanding of coil resistance is imperative to the theoretical characterization of the SNR in submillimeter NMR.

### 2.2.2.1 Loss in alternating current conductors

When determining  $R_c$ , one must consider the effects of alternating current and the linkage of flux which results throughout the local region of the coil. The fundamental rule-of-thumb in understanding alternating current effects is that a net flow of electrons will occur in those regions of the conductor which exhibit the lowest impedance to their movement. For example, the interior of the wire from which the solenoid is wound will contain magnetic flux which links a fraction of the total current. The establishment of a linkage of flux results in an inductive reactance which serves to impede current flow. At sufficiently large wire diameters and high frequency, all current is assumed to flow on the outer perimeter of the wire, where the fewest flux linkages exist. This effect is termed "skin effect." In actuality the current density and electric field intensity decrease exponentially from the

surface of the wire toward the center. The distance into the wire at which the current density and electric field intensity are decreased to  $e^{-1} = 36.8\%$  of their value at the surface is termed the "skin depth," given by

$$\delta = \frac{1}{\sqrt{\mu\pi f\sigma}}$$

where  $\sigma$  is the wire conductivity. The distortion of the current distribution from uniform results in a reduced effective cross-sectional area for current flow and is termed "current crowding." Current crowding leads to an increased effective coil resistance. Similarly, in addition to the linkage of magnetic flux within the wire itself, there will be magnetic flux which extends beyond the wire and which may link neighboring conductors and vice versa. This also results in a distortion of the current distribution and an increased effective resistance for the solenoid. This effect is appropriately termed "proximity effect."

In traditional NMR (with samples and coils with dimensions greater than 1 mm) a "macroscopic model" is frequently employed to theoretically calculate  $R_c$ , accounting for skin effect and proximity effect by the inclusion of a skin effect factor ( $\delta$ ) and a proximity effect factor ( $\xi$ ). This model is derived by taking the limiting values of the complete solutions to Maxwell's equations (Eq. (1)). However, many of the assumptions made in the macroscopic model are compromised at smaller dimensions, and a retreat to the complete theoretical description is required to produce a microscopic model for smaller dimensions. As we shall show, the terms "macroscopic model" and "high-frequency model" can be used interchangeably, as can the terms "microscopic model" and "low-frequency model," because  $R_c$  depends on both the frequency and the wire size.

The effect of an increased loss in conductors which carry alternating currents was examined as early as 1886 by Raleigh<sup>5</sup> and was pursued by many authors into the early 1900s.<sup>7-13</sup> However, the first complete and concise summary of this effect was by Butterworth in 1926.<sup>14</sup> In a series of four papers he presented a methodology for determining the losses inherent in such conductors, and laid a

foundation from which this theory could be applied to almost any geometrical configuration. There are really two approaches that one may take in determining the losses in conductors at alternating frequencies. The first is to consider the wire as a guiding structure, down which the impinging electromagnetic field is propagating. This requires the complete solution to Maxwell's equations, the objective being to determine both the loss in the conductor as well as the form of the electromagnetic field in the local region of the coil. This approach is computationally intensive, and was nearly impossible before the advent of the computer. The second approach, the one chosen by Butterworth, is to first assume that the current distribution in the wire is uniform and well-defined, as would be the case for a static electromagnetic field. From this, the static wire losses are determined. The effects of a slowly alternating field are then considered by calculating the eddy currents which would flow within the wire due to the time-varying flux present in the wire. The eddy currents alter the current distribution which would exist if the field were not time-varying. The eddy current losses are added to the static losses to yield the total loss in the wire. The losses which result from wires being placed in close proximity to one another are handled in a similar manner. At higher frequencies, the loss in the wire is determined by using the limiting values of the mathematical relationships obtained for the low-frequency case. While both approaches must result in the same conclusion, the latter method is less mathematically cumbersome and is sufficient to determine the current distribution in the wire, and hence the loss. As shown in Eq. (8), the determination of the wire loss (i.e., resistance) is crucial for evaluating the SNR in microdomain coils. The first method would directly provide the form of the electromagnetic field throughout the region of the coil. However, the symmetries afforded by the solenoidal coil geometry will provide a relatively uniform field throughout the central region of the coil even through the current distribution in the individual wires is nonuniform.

Butterworth's treatise<sup>14</sup> has been used routinely to determine the loss in conductors which carry high-frequency alternating currents and to provide a quantitative model to predict the frequency dependence of such loss. However, fewer applications have arisen in which the theory has been used to predict the losses in the conductor at a fixed frequency of operation but in which the wire diameter has been reduced to several skin depths or less. An understanding of the functional dependence of

both frequency and wire size on alternating current losses in conductors is imperative to the development of a quantitative model to predict the loss in microcoils. The equations which follow are derived from Butterworth's treatise and are used to determine the loss which occurs in microdomain solenoidal coils.

The alternating current losses in microcoils can be divided into two components: 1) straight-wire losses, and 2) coiled-wire losses.

#### 1) Straight-wire losses

The first loss to consider is the loss which would occur in a perfectly straight wire. There is a resistive loss associated with the forced movement of electrons through the lattice structure of the wire. The lattice resists the flow of electrons, and this loss would occur regardless of whether the current is oscillating or not. Considering a typical cross section of wire, all regions represent an equal impedance to the transport of electrons, and consequently the current distribution in the wire is uniform. Hence, if one were to consider a 4-turn solenoidal coil and neglect all other losses, a cross-sectional view of the current distribution in the coil would appear as in Figure 10.

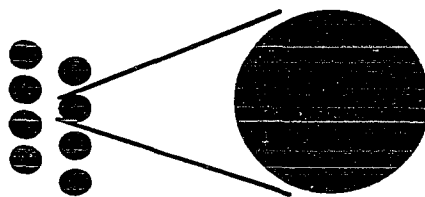


Figure 10 The current distribution in a straight wire where the only loss considered is that due to the lattice resistance.

A second component of straight-wire loss arises from the effects of alternating current and results in a redistribution of the current in the wire. It is a fundamental principle of electromagnetic induction that when the lines of force of a varying magnetic field thread through *any* conducting mass there is induced in that mass a circulating (eddy) current.<sup>14</sup> The eddy currents require energy for their maintenance, which must be supplied to the mass from the current producing the varying field, and

thus the effective resistance of the coil carrying this current is increased. This is manifest by a reduced cross-sectional area over which the current flows. Consider a typical cross section of wire shown in Figure 11 where the direction of alternating current ( $I$ ) is assumed to be out of the page. The lines of magnetic force within the wire obey Ampere's law,

$$\int \mathbf{H} \cdot d\mathbf{l} = I$$

with direction determined by the right-hand rule. Now consider a wedge AB in the cross section as shown in Figure 12. The flux lines penetrate the wedge, inducing an emf in accordance with Faraday's law,

$$\text{emf} = - \frac{d\phi}{dt}$$

which will, in turn, give rise to an induced eddy current ( $I_s$ ) within the wedge. The direction of eddy current flow will be such that the magnetic field ( $H_s$ ) produced by the eddy current opposes the main magnetic field ( $H$ ) resulting from the main current flow ( $I$ ). Therefore,  $I_s$  flows against  $I$  at the central regions of the wire and flows with  $I$  at the outer regions of the wire as shown in Figure 13. The eddy current goes and returns inside the conductor and does not add to the net current flow through the wire. However, it does distort the current distribution by enhancing  $I$  in the outer regions of the wire and diminishing  $I$  in the inner regions.



Figure 11 There is an alternating magnetic field established within the wire due to the alternating current flowing through the wire.

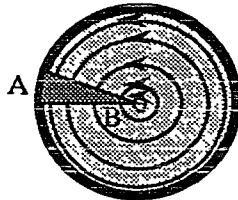


Figure 12 The alternating magnetic field induces eddy currents which flow in a plane perpendicular to the magnetic field lines within the wire.

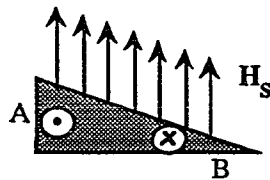


Figure 13 A typical path of eddy current flow which results from the alternating magnetic field within the wire.

The total loss within the straight conductor is now found by adding the loss due to  $I$  and the loss due to  $I_s$ . The main current loss is

$$P = \frac{1}{2} I^2 R$$

where  $I$  is the *peak* value of the main current and  $R$  is the resistance of the wire. To consider the eddy current loss, let  $V_s$  be the spatially averaged, peak-induced emf throughout the wedge. Furthermore, assume that the frequency is sufficiently low so that the resistance of the eddy current path ( $R_s$ ) dominates the inductive reactance ( $\omega L_s$ ) of the eddy current path. The eddy current loss is then given by

$$P_s = \frac{1}{2} \frac{|V_s|^2}{R_s}$$

The first step in determining  $P_s$  is to determine  $V_s$ . The magnetic field  $H$  which induces the emf is found by Ampere's law to be

$$H = \frac{\left(\frac{I r^2}{a^2}\right)}{2\pi r}$$

where  $a$  is the total wire radius, and  $r$  is the radial position at which  $H$  is being determined. Therefore, the flux passing through wedge AB is

$$\begin{aligned}\phi &= \int B \cdot dS \\ &= \int_{r=0}^{r=a} \mu \frac{\left(\frac{I r^2}{a^2}\right)}{2\pi r} (l \, dr) \\ &= \frac{\mu I l}{4\pi}\end{aligned}$$

The length of the wedge (into the paper) is represented by  $l$ . By Faraday's law,

$$|\text{emf}| = \left| -\frac{d\phi}{dt} \right| = | -j\omega\phi | = \frac{\omega\mu I l}{4\pi}$$

The magnetic field  $H$  within the wire is not uniform but varies radially in intensity. Similarly, the induced emf ( $V_s$ ) will vary across the width of the wedge. There are actually a number of infinitesimal eddy current paths throughout the wedge, with the path at the perimeter of the wedge encircling the total flux and having the highest induced emf. The emf for the remainder of the eddy current paths will be somewhat less, reducing to near zero for an infinitesimally small path at the center of the wedge with near-zero radius. As a simple approximation, we assume a single eddy current path for the wire. The wire is divided into two concentric conductors, similar in shape to a coaxial transmission line but

with no space between the inner and outer conductors. For this eddy current path, it is safe to assume a spatial *average* value of one half of the emf found above. Therefore,

$$|V_s| = \frac{\omega\mu I l}{8\pi}$$

The resistance of the eddy current path ( $R_s$ ) must now be found. By assuming a spatially averaged emf, the cross-sectional area of the two conductors must be the same, half that of the total wire, to meet the necessary boundary conditions that no eddy current leave the region. Each conductor would thus have a resistance  $2R$ , and the round-trip eddy current path would have a resistance  $R_s = 4R$ . Therefore,

$$P_{s0} = \frac{1}{2} \frac{|V_s|^2}{R_s} = \frac{\left(\frac{\omega\mu I l}{8\pi}\right)^2}{4R} = \frac{(\omega\mu I l)^2}{512\pi^2 R}$$

The estimates of an *average* emf and of the simple eddy current path for calculating  $R_s$  can be expected to have a finite degree of error. The coefficient requires a correction of 4/3 for accuracy,<sup>14</sup> giving

$$P_s = \frac{(\omega\mu I l)^2}{384\pi^2 R} \quad (9)$$

The total loss in the wire is the sum of the two losses.

$$\begin{aligned} P_w = P + P_s &= \frac{1}{2} I^2 R + I^2 \left[ \frac{\omega^2 \mu^2 l^2}{384\pi^2 R} \right] \\ &= \frac{1}{2} I^2 R \left[ 1 + \frac{\omega^2 \mu^2 l^2}{192\pi^2 R^2} \right] \end{aligned} \quad (10)$$

We can define an effective alternating current wire resistance  $R_w$  as

$$R_w = R \left[ 1 + \frac{\omega^2 \mu^2 l^2}{192 \pi^2 R^2} \right]$$

The dc resistance ( $R$ ) for a straight wire can be easily calculated by

$$R = \frac{\rho l_{\text{conductor}}}{A_{\text{cross section}}} \quad (11)$$

with  $A_{\text{cross section}} = \pi d^2/4$ , where  $d = 2a$  is the diameter of the wire, giving

$$\begin{aligned} R_w &= R \left[ 1 + \frac{\omega^2 \mu^2}{3072 \rho^2} d^4 \right] \\ &= R [1+F] \end{aligned} \quad (12)$$

where the first term ( $R$ ) represents the main, or dc loss, and the second term ( $R_{\text{skin}} = RF$ ) represents the eddy current, or skin effect loss due to the alternating current.

The overall resistance of (and loss in) the wire is seen to be increased by the addition of eddy current effects. We can massage  $F$  into a more useful form by setting

$$F = \frac{z^4}{768} \quad (13)$$

where  $z = d(\mu\pi f\sigma)^{1/2} = d/\delta$ ;  $\mu$  is the permeability of the wire,  $\sigma$  is the wire conductivity,  $f = \omega/2\pi$  is the frequency of operation, and  $\delta$  is the skin depth of the wire. We see then that the loss contribution arising from circulating eddy currents within the wire and due to the field established by the main

current in the wire is proportional to  $z^4$  where  $z$  is the diameter of the wire relative to one skin depth. The factor  $z$  is perhaps the most relevant scaling parameter for the design of microscopic coils. In essence, the presence of  $z$  in Eq. (13) implies that one cannot separate the consideration of proper wire diameter from the frequency of interest for applications requiring alternating current conductors. Hence the terms "low frequency" and "small wire" need to be further qualified, for when one is stated, an inference to the other is made.

From Eq. (13) we see that the loss arising from the self-induced eddy current in a straight wire is less pronounced at smaller wire sizes. The relative magnitude of the eddy current (relative to the main current) may be found by applying Ohm's law,

$$|I_s| = \frac{|V_s|}{R_s} = \frac{\left(\frac{\omega\mu I l}{8\pi}\right)}{4R} = \frac{\omega\mu I l}{32\pi R}$$

Therefore,

$$\left|\frac{I_s}{I}\right| = \frac{\omega\mu l}{32\pi R} = \frac{\omega\mu d^2}{128\rho} \propto \omega d^2 \quad (14)$$

From this we see that at lower frequencies the relative magnitude of the eddy current is reduced, with the severity of skin effect proportional to the frequency. As to variation in wire diameter, the skin effect is seen to be more heavily influenced by wire diameter than by frequency, increasing in severity as wire diameter squared. Thus the presence of the circulating eddy current leading to the skin effect is quickly diminished as the wire diameter is reduced, with a true quasi-static uniform current distribution resulting in small wires as shown in Figure 10. Such small wires are necessary for the construction of microdomain coils. Therefore, a coil resistance formula which simply assumes a uniform current distribution around the perimeter of the wire within one skin depth is incorrect at microscopic dimensions.

In the derivation above, the assumption of "low frequency" is really a statement of the magnitude of  $z$ . Hence, the form of  $F$  shown in Eq. (13) is valid for small  $z$  only, e.g.,  $z \leq 2$ . In the limiting case of large  $z$  (high frequency and large wire diameters), the assumptions made for low  $z$  (e.g.,  $R_s \gg \omega L_s$ ) are no longer valid, and some intuition will prove beneficial. Physically, it is well-known that at commonly used wire sizes and very high frequencies, all of the net current can be assumed to flow on the perimeter of the wire within one skin depth  $\delta$ . Therefore, the cross-sectional view of the current distribution in a 4-turn solenoid (Figure 10) is modified as shown in Figure 14.

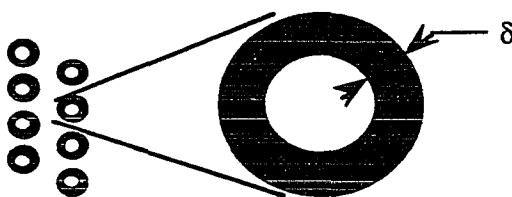


Figure 14 The current distribution in a straight wire at large values of  $z$ , where the loss in the wire arises from both the main current and the eddy currents due to the alternating magnetic field within the wire.

The resistance of a straight wire,  $R_w$ , can be easily calculated by using Eq. (11) with a modified effective cross-sectional area for current flow given by  $A_{\text{eff}} = \pi a^2 - \pi(a-\delta)^2$  where  $a$  is the wire radius. Equation (11) can be used (even at high frequencies) provided that the physical dimensions of the coil are maintained at much less than one wavelength, i.e., the overall coil reactance is kept very small. The restriction of coil size validates the use of a quasi-static electromagnetic field analysis for the coil. Quasi-static electromagnetic conditions are equivalent to ignoring retardation and radiation effects. Consequently, the NMR coil can be considered a near-field device, and the radiation resistance (and associated noise) is negligible. Assuming  $a \gg \delta$ ,

$$R_w \Big|_{z \text{ large}} = \frac{\rho l}{2\pi a \delta} \quad (15)$$

The resistance ratio of a wire is generally defined as  $(\bar{R}_{ac} + \bar{R}_{dc})/\bar{R}_{dc}$ , and is representative of the ratio of the total loss in the wire to the loss which would result from a direct current only. In the present case, the skin effect is the only alternating current effect being considered, and the resistance ratio is given as  $R_w/R = R(1+F)/R = 1+F$ .

$$\left. \frac{R_w}{R} \right|_{z \text{ large}} = 1+F = \frac{\left[ \frac{\rho l}{\pi d \delta} \right]}{\left[ \frac{4\rho l}{\pi d^2} \right]} = \frac{d}{4\delta} = \frac{z}{4}$$

Therefore,

$$\left. F \right|_{z \text{ large}} = \frac{z}{4} - 1$$

The functional dependence of  $F$  on  $z$ , for larger values of  $z$ , is reduced from a fourth-power dependence to a linear dependence. Dimensional analysis reveals that  $F$  is a pure number and a function of  $z$  alone. The general form of  $F$  can be written as a series

$$F = f(z) = \sum A_N (z^N)$$

where  $0 \leq N \leq 4$ . The high-frequency form of  $F$  is given by  $F = A_0 + A_1 z$ , where  $A_0 = -1$  and  $A_1 = 1/4$  for infinitely large  $z$ , and the lower terms ( $N = 0, 1$ ) of the series dominate. For large  $z$  ( $z > 7$  but  $z < \infty$ ), a slight adjustment is made to  $A_0$  to account for the curvature of the wire. The depth of penetration in a wire with a finite radius of curvature is somewhat less than that which would

be obtained for a perfectly flat surface. Summarizing, the value of  $F$  at high values of  $z$  is given by

$$F = \begin{cases} \frac{1}{4} z - 1 & z = \infty \\ \frac{1}{4} z - \frac{3}{4} & 7 < z < \infty \end{cases} \quad (16)$$

The low-frequency form of  $F$  is given by  $F = A_4 z^4$ , where  $A_4 = 1/768$ , and the highest term ( $N = 4$ ) of the series dominates. There remains a range ( $2 \leq z \leq 7$ ) for which the value of  $F$  is more difficult to evaluate, as a greater number of terms in the series expansion must be retained. A graph of  $F$  and  $1+F$  (i.e., resistance ratio) values for  $0.1 \leq z \leq 150$  is given in Figure 15, with interpolated values for the regime  $2 \leq z \leq 7$  as suggested by Rosa and Grover.<sup>7</sup> From the graph, it is evident that the total loss in a straight wire approaches that of the static case for small  $z$ , and that the large  $z$  loss is primarily due to the eddy currents (skin effect). If we restrict our attention to microdomain coils ( $d_{\text{coil}} < 1$  mm), the high values of  $z$  can be neglected. For example,  $\delta_{\text{copper}} = 4.66 \mu\text{m}$  at 200 MHz. The copper wire used to wind a microdomain coil will typically be much less than  $100 \mu\text{m}$  ( $\cong 20$  skin depths) and may be less than  $12 \mu\text{m}$  ( $\cong 2^{1/2}$  skin depths). Therefore, the "knee" of the curve is of particular interest, and is shown expanded in Figure 16. It is important to consider Figure 16 when designing microdomain coils with small wires, for it is within this regime that straight-wire losses shift from being dominated by the eddy currents (macroscopic model) to being dominated by the fundamental (and irreducible) dc resistance (microscopic model).

We have shown that one must consider both wire diameter and frequency when determining the form of the losses in a straight wire. In the next section, we will show that this is also true of the losses in a coiled wire. Hence the models which are to be used in characterizing wire losses will depend on both wire size and frequency of operation. Congruent with this fact, the terms given to the models are "high-frequency" or "macroscopic" and "low-frequency" or "microscopic" for  $z > 7$  and  $z \leq 2$ , respectively. We assume a fixed frequency of precession as a reference for the calculation of SNR, with the coil and wire size variable.

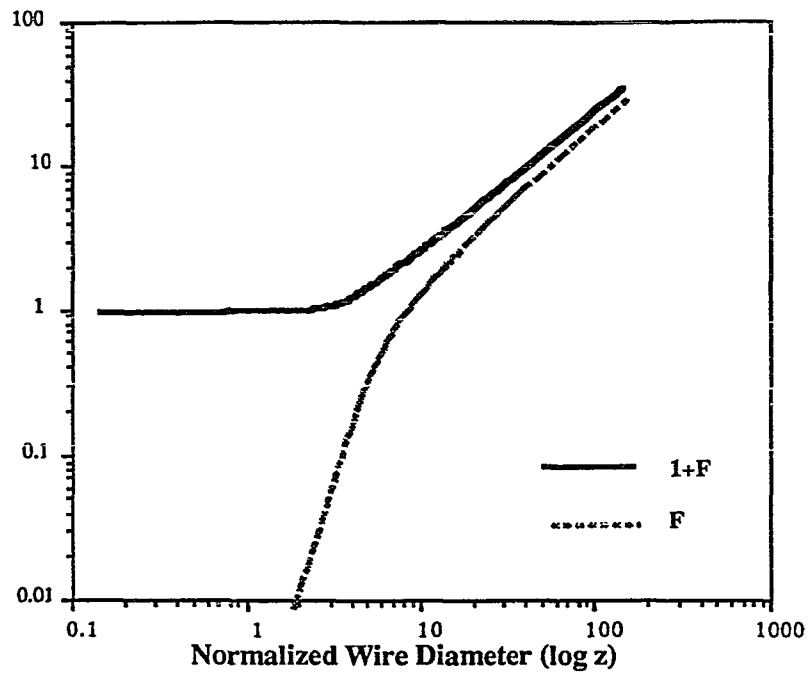


Figure 15 The resistance ratio and skin effect factor for a straight wire.

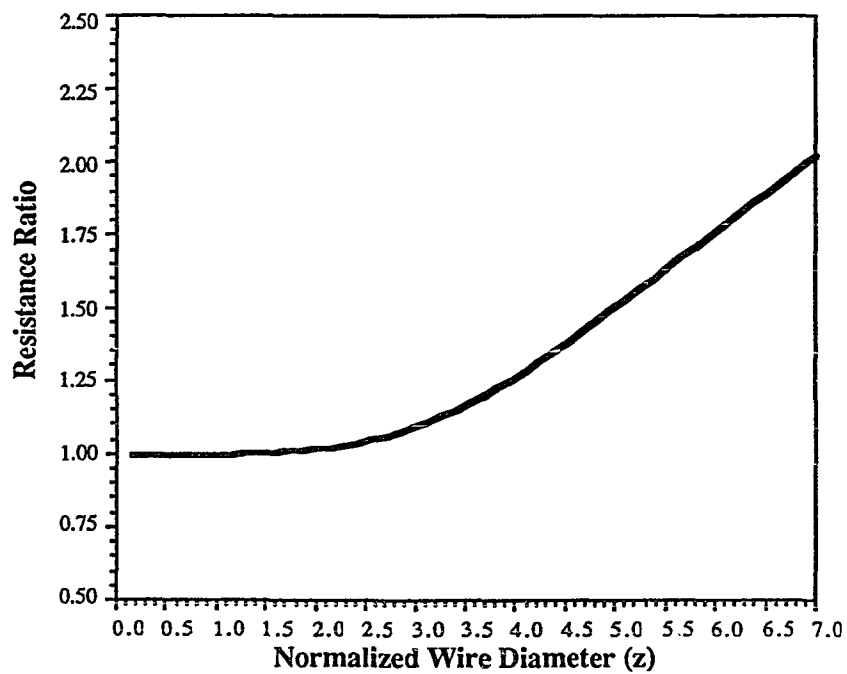


Figure 16 The resistance ratio for a straight wire ( $2 \leq z \leq 7$ ).

Therefore we will use the terms macroscopic and microscopic when describing the coil models. One should remember however that it is the parameter  $z = d/\delta$  that must ultimately be determined when considering the specific coil model to use.

Summarizing, the losses in a straight-wire go from being dominated by eddy current losses to direct current losses as the diameter of the wire is reduced below several skin depths ( $z = d/\delta \leq 7$ ) at the frequency of interest. From Eq. (14) we see that the eddy current losses rapidly diminish in the low  $z$  regime ( $z = d/\delta \leq 2$ ), with smaller wires only exaggerating the dominance of the dc losses, for not only is the value of  $z$  smaller, but also the dependence on  $z$  is much greater (increasing from a direct dependence to a fourth-power dependence as  $z$  decreases in the regime  $2 \leq z \leq 7$ ). It is important to note that straight-wire losses generally increase as the wire size decreases, regardless of the regime. Consider the limiting cases of  $z$ . From Eq. (12), the total resistance in the wire varies as

$$R_w \propto \frac{1}{d^2} [1+F] \quad (17)$$

For small values of  $z$  ( $z \leq 2$ ),  $F \propto z^4 \propto d^4$ . However, the absolute magnitude of  $F$  in this regime is seen from Figure 14 to be  $F \ll 1$  so that

$$R_{w_{\text{small } z}} \propto \frac{1}{d^2} \quad (18)$$

For large values of  $z$  ( $z > 7$ ),  $F \propto z \propto d$ , and the magnitude of  $F$  is clearly  $F \gg 1$ . Thus,

$$R_{w_{\text{large } z}} \propto \frac{1}{d} \quad (19)$$

The resistance (and loss) in the straight wire is seen to increase with decreasing wire diameter regardless of the size regime, with the dependence being stronger at small  $z$ .

Last, consider the assumption made at the beginning of the derivation that the resistive component of the eddy current path impedance dominates the reactive component at both low frequency and at small wire diameters. As a test of validity, consider the ratio  $X_s/R_s$ . The internal inductance per unit length of a straight wire (and of the eddy current path) remains relatively insensitive to changes in wire diameter so that the ratio can be written

$$\frac{X_s}{R_s} = \frac{\omega L_s}{4R} = \frac{\omega \lambda l}{4 \left[ \frac{4\rho l}{\pi d^2} \right]} \propto \omega d^2$$

where  $\lambda$  is the inductance per unit length of the eddy current path. The validity of the assumption made in quantitating the severity of the eddy current effect scales identically as the severity of the effect. Therefore, the assumption that the resistive component of the eddy current path impedance dominates that of the reactive component is increasingly valid not only at lower frequencies but also at smaller wire diameters. Similarly, at large  $z$ ,  $X_s \gg R_s$ . The relative eddy current magnitude is found by

$$\frac{|V_s|}{\omega L_s} = \frac{\left[ \frac{\omega \mu I}{8\pi} \right]}{\omega(\lambda l)} = \frac{\mu I}{8\pi \lambda} = |I_s|$$

At infinite values of  $z$ , all of the current in the center of the wire is cancelled by the eddy current, with  $I_s = I$ , and the value of  $\lambda$  is readily found.

$$\left| \frac{I_s}{I} \right| = \frac{\mu}{8\pi \lambda} = 1 \Rightarrow \lambda = \frac{\mu}{8\pi}$$

The inductance per unit length herein derived is the established formula for the self inductance of a straight wire found in many textbooks on basic electromagnetic theory,<sup>15,16</sup> and supports the validity of the model we have chosen to use.

## 2) Coiled-wire losses

A solenoid is formed by coiling several turns of straight wire. There are losses which result from the wire being coiled, with the turns placed in close proximity to one another. The magnetic field lines from a given turn of a solenoidal coil affect adjacent turns, inducing eddy currents in them and distorting the current distribution in the wire from that shown in Figure 10. These losses are appropriately termed "proximity effect losses."

Consider a typical cross section of wire immersed in an external magnetic field  $H_{ext}$  as shown in Figure 17 where the direction of current flow is arbitrarily assumed to be out of the paper. By similar arguments as in the previous section, the time-dependent flux cutting through the wire induces an emf which results in eddy currents with net magnitude  $I_p$  flowing within the wire where  $I_p \propto H_{ext}$ . The losses incurred by the circulating eddy currents are proportional to  $I_p^2$  and consequently to  $H_{ext}^2$ . Dimensional analysis reveals that the form of the term which represents the proximity effect loss ( $P_p$ ) must be

$$P_p = \frac{1}{2} I_p^2 R_p = \frac{1}{2} k_G G H_{ext}^2 ( ) ( )$$

$\begin{matrix} \nearrow A^2 & \nearrow \Omega & \nearrow (A/m)^2 & \nearrow m^2 & \nearrow \Omega \\ \nwarrow & \nwarrow & \nwarrow & \nwarrow & \nwarrow \\ & \text{Unless scaling factor} & & & \end{matrix}$

where  $G$  is a numerical quantity depending only on  $d$ ,  $f$ ,  $\sigma$ , and  $\mu$ , that is,  $G = f(z)$ . In the above equation, the total resistance of the eddy current path is  $R_p = 4R$ . This is obtained by assuming that the wire is divided into equal hemispheres, with the current flowing out one side and returning back via the other side, and a total round-trip path length of  $2(l)$ . The total resistance of the proximity effect current path is therefore  $R_p = (2R)(2) = 4R$ . However, we wish to define the total loss in terms of

the wire resistance ( $R$ ) to preserve the form of Eq. (10) when including the proximity effect loss in the total wire loss ( $P_w$ ). Similarly, we wish to use the wire diameter ( $d$ ) for the "area" term in the above expression. The scaling factor  $k_G$  absorbs the necessary constants to preserve the equality.

$$P_p = \frac{1}{2} \left[ k_G G H_{\text{ext}}^2 d^2 \right] R \quad (20)$$

The task now becomes to define  $G$ , using procedures analogous to those used to determine  $F$  in the previous section.

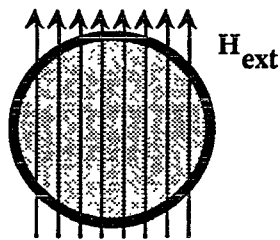


Figure 17 The alternating magnetic field lines of a neighboring wire can affect the wire of interest by inducing eddy currents within the wire.

The magnitudes of the eddy currents induced at low frequencies are small and we may neglect any effect from the eddy current magnetic field in comparison to the main field. This is identical to assuming that the resistive component of the eddy current path impedance is large relative to the reactive component. In the previous section the validity of this assumption was shown for both low frequency and small wire diameters. Therefore, the total loss in the wire  $P_p = |V_p|^2/R_p$  is found and set equal to Eq. (20) from which  $G$  is then determined.

To determine the magnitude of the induced emf, consider a plane  $CD$  in the wire cross section as shown in Figure 18. Assume the current in the wire to be flowing out of the page and the direction of  $H_{\text{ext}}$  as shown. The emf generated is found by Faraday's law and supports an eddy current  $I_p$  within the plane. As the magnetic field from the eddy current must oppose  $H_{\text{ext}}$ , the eddy currents

flow in the direction shown, enhancing  $I$  in the right hemisphere of the wire and diminishing  $I$  in the left hemisphere. The flux enclosed by a given differential eddy current path is

$$\begin{aligned}\phi &= \int_{l'=0}^{l'=l} \mathbf{B}_{\text{ext}} \cdot d\mathbf{S} \\ &= \int_{l'=0}^{l'=l} \mu \mathbf{H}_{\text{ext}} \cdot (2x \, dl') \\ &= 2\mu \mathbf{H}_{\text{ext}} \cdot x l\end{aligned}$$

Therefore, the emf is given by

$$|emf| = \left| -\frac{d\phi}{dt} \right| = | -j\omega\phi | = 2\omega\mu \mathbf{H}_{\text{ext}} \cdot x l \quad (21)$$

The value of  $\mathbf{H}_{\text{ext}}$  is assumed to be uniform across the cross section of the wire. Therefore, the emf induced in each differential eddy current path is given by Eq. (21).

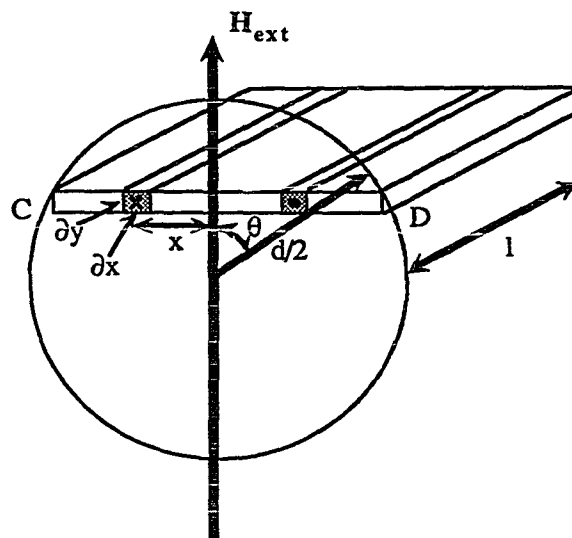


Figure 18 A differential eddy current path within the cross section of the wire.

The resistance of the differential eddy current path is

$$R_{\text{eddy}} = \frac{\rho (2l)}{\partial x \partial y}$$

and the differential loss in a given eddy current path is

$$P_{\text{eddy}} = \frac{i}{2} \frac{i e m \mu l^2}{R_{\text{eddy}}} = \frac{i}{2} \frac{(2 \omega \mu H_{\text{ext}} x l)^2}{\left( \frac{2 \rho l}{\partial x \partial y} \right)} = \frac{\omega^2 \mu^2 H_{\text{ext}}^2 x^2 l}{\rho} \partial x \partial y$$

To find the total loss in the wire, a change of coordinate systems is useful. Let  $x = r \sin \theta$  and  $y = r \cos \theta$ . The total loss is found by integrating the individual losses from each of the differential eddy current paths over the cross section of the wire.

$$\begin{aligned} P_p &= \int_{\theta=0}^{\theta=\pi} \int_{r=0}^{r=d/2} \frac{\omega^2 \mu^2 H_{\text{ext}}^2 l}{\rho} (r^2 \sin^2 \theta) r dr d\theta \\ &= \frac{\omega^2 \mu^2 H_{\text{ext}}^2 l}{\rho} \int_{\theta=0}^{\theta=\pi} \sin^2 \theta d\theta \int_{r=0}^{r=d/2} r^3 dr \\ &= \frac{\omega^2 \mu^2 H_{\text{ext}}^2 l \pi}{128 \rho} d^4 \end{aligned} \quad (22)$$

By substituting the dc resistance  $R$  into Eq. (20),

$$P_p = \frac{1}{2} k_G G H_{\text{ext}}^2 d^2 \left[ \frac{4 \rho l}{\pi d^2} \right] = \frac{2 k_G G H_{\text{ext}}^2 \rho l}{\pi} \quad (23)$$

Comparing Eqs. (22) and (23),

$$\begin{aligned} k_G G &= \frac{\pi^2 \omega^2 \mu^2 \sigma^2}{256} d^4 = 4\pi^2 \left[ \frac{\pi^2 f^2 \mu^2 \sigma^2}{256} \right] \\ &= 4\pi^2 \left[ \frac{z^4}{256} \right] \end{aligned}$$

where  $z$  is defined in the previous section to be  $z = d/\delta$ . Therefore,

$$\begin{aligned} k_G &= 4\pi^2 \\ G &= \frac{z^4}{256} \end{aligned} \tag{24}$$

This form of  $G$  is valid for the low  $z$  regime ( $z \leq 2$ ).

Similar to  $F$ , the functional dependence of  $G$  on  $z$  is reduced from a fourth-power dependence to a linear dependence for larger values of  $z$ . At large  $z$ , the induced eddy currents are sufficiently powerful to annul the field inside the wire and the lines of  $H_{\text{ext}}$  curve around the wire. Unlike the skin effect, the current due to the proximity effect is asymmetrically distributed about the perimeter of the wire, being greatest in the regions corresponding to the largest value of  $H_{\text{ext}}$ . However, similar to the skin effect, the depth of current penetration due to the proximity effect is independent of the diameter of the wire. Hence, the cross-sectional area of current flow is proportional to the perimeter of the wire, and the *form* of the wire resistance is that of Eq. (15). The general form of  $G$  can be written as a series,

$$G = g(z) = \sum B_N (z^N)$$

where  $0 \leq N \leq 4$ . The high-frequency form of  $G$  is given by  $G = B_0 + B_1 z$ , where  $B_0 = 0$  and  $B_1 = 1/8$  for infinitely large  $z$ , and the lower terms ( $N = 0, 1$ ) of the series dominate. For large  $z$

( $z > 7$  but  $z < \infty$ ), a slight adjustment is made to  $B_0$ , and the value of  $G$  at high values of  $z$  is given by<sup>7,14</sup>

$$G = \begin{cases} \frac{z}{8} & z = \infty \\ \frac{1}{8} z - \frac{1}{8} & 7 < z < \infty \end{cases} \quad (25)$$

The low-frequency form of  $G$  is given by  $G = B_4 z^4$ , where  $B_4 = 1/256$ , and the highest term ( $N = 4$ ) of the series dominates. As with  $F$ , the exact form of  $G$  for  $2 \leq z \leq 7$  is complicated. A graph of  $G$  for  $0.1 \leq z \leq 150$  is given in Figure 19, with the knee of the curve ( $1 \leq z \leq 7$ ) expanded and shown in Figure 20.

It is useful to further quantify Eq. (23). The total loss due to the circulating eddy currents induced in a wire by the magnetic field from a neighboring wire in close proximity is given by  $P_p \propto G H_{\text{ext}}^2 \propto (\omega^2 d^4) H_{\text{ext}}^2$ . The external magnetic field ( $H_{\text{ext}}$ ) can be expressed in terms of the magnitude of current ( $I_{\text{ext}}$ ) flowing in an adjacent wire and the distance of separation ( $r_{\text{sep}}$ ) between the two wires as shown in Figure 21. From Ampere's law,

$$H_{\text{ext}} = \frac{I_{\text{ext}}}{2\pi r_{\text{sep}}}$$

Therefore,

$$P_p \propto (\omega^2 d^4) \left[ \frac{I_{\text{ext}}^2}{r_{\text{sep}}^2} \right] = \omega^2 \left[ \frac{d}{r_{\text{sep}}} \right]^2 d^2 I_{\text{ext}}^2 \quad (26)$$

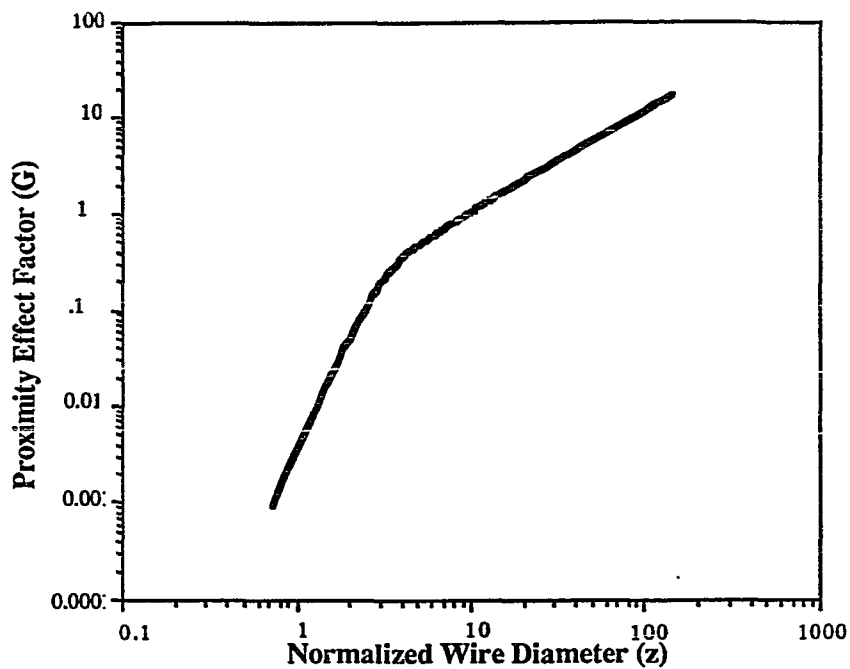


Figure 19 Proximity effect factor (G) for  $0.14 \leq z \leq 140$

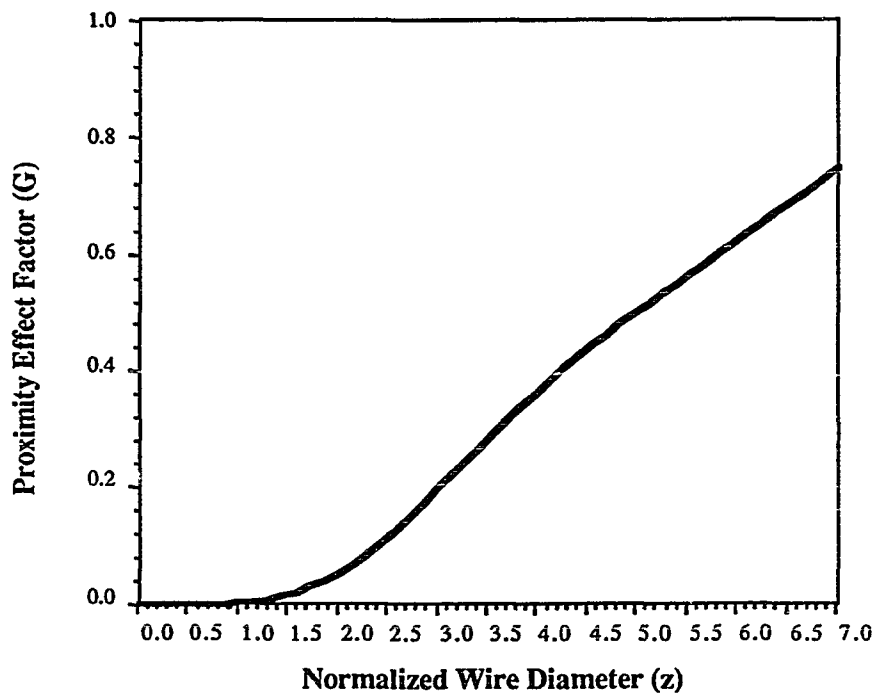


Figure 20 Proximity effect factor (G) for  $0.14 \leq z \leq 7$

The proximity effect (coiled-wire) losses are seen to vary directly with the square of the frequency and the wire diameter *and* inversely with the square of the relative wire spacing, that is, the number of wire diameters between adjacent wires. Thus, unlike straight-wire losses, coiled-wire losses are less pronounced at smaller wire sizes. Additionally, coiled-wire losses are equally dependent on the relative wire spacing and increase drastically when the distance of separation (relative to the wire diameter) is reduced.

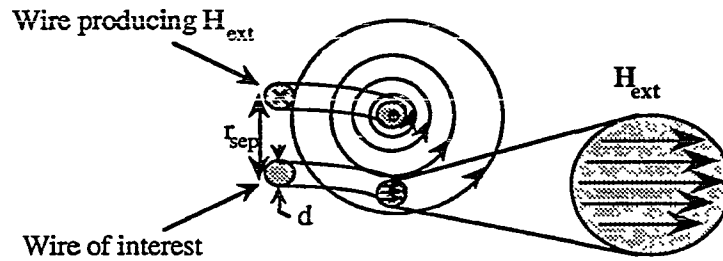


Figure 21 The degree of influence of the magnetic field from adjacent wires on the wire of interest is proportional to the distance of separation between the two wires.

Consider the special case of a 2-turn solenoidal coil with diameter sufficiently large to ignore the field produced by current flowing in the opposite side of the coil. The magnitude of the current flowing in an adjacent turn ( $I_{ext}$ ) will be the same as the current flowing in the wire of interest ( $I$ ). We can then calculate the relative magnitude of the eddy current. From Eqs. (20), (23), and (24),

$$I_p = \frac{\sqrt{k_G G} H_{ext} d}{4} = \left[ \frac{2\pi d^2}{64\delta^2} \right] \left[ \frac{I}{2\pi r_{sep}} \right] d$$

Therefore,

$$\left| \frac{I_p}{I} \right| = \frac{d^2}{64\delta^2} \left[ \frac{d}{r_{sep}} \right] \propto \omega d^2 \left[ \frac{d}{r_{sep}} \right] \quad (27)$$

where the relationship  $R_p = 4R$  has been used. The severity of the proximity effect is proportional to frequency and the square of the wire diameter. Additionally, it is inversely proportional to the inter-turn spacing (number of wire diameters between turns). Hence, if one were interested solely in reducing the severity of proximity effect in a 2-turn solenoid (at a given frequency of operation), one would use extremely small wire and an infinite wire separation. The total power loss in the 2-turn coil can be found by adding the proximity effect loss ( $P_p$ ) to the dc and skin effect losses ( $P$  and  $P_s$ , respectively), in the wire.

$$\begin{aligned}
 P_w &= P + P_s + P_p \\
 &= \frac{1}{2} I^2 R \left[ 1 + \frac{\omega^2 \mu^2 l^2}{192 \pi^2 R^2} \right] + \frac{1}{2} I_p^2 R_p \\
 &= \frac{1}{2} I^2 R \left[ 1 + \frac{\omega^2 \mu^2 l^2}{192 \pi^2 R^2} + \frac{\omega^2 \mu^2 l^2}{64 \pi^2 R^2} \left[ \frac{d}{2 \pi r_{sep}} \right]^2 \right] \\
 &= \frac{1}{2} I^2 R \left[ 1 + F + k_G G \left[ \frac{d}{2 \pi r_{sep}} \right]^2 \right]
 \end{aligned} \tag{28}$$

and the total effective resistance of the wire can now be written as

$$\begin{aligned}
 R_w &= R \left[ 1 + F + k_G G \left[ \frac{d}{2 \pi r_{sep}} \right]^2 \right] \\
 &= R_{dc} + R_{skin} + R_{prox}
 \end{aligned} \tag{29}$$

where one must remember that  $R$  now represents the total dc loss in the 2-turn solenoid and is twice that of a single loop of wire of the same diameter.

The assumption made in Eq. (29) is that the inter-turn spacing is sufficiently large so that the shape of the magnetic field affecting a given turn ( $H_n$ ) is not distorted by the magnetic field produced by the induced eddy currents. As the wires are moved to within 1.5 wire diameters, the proximity

effect term requires some modification. The proximity effect term in Eq. (29) is actually an infinite series of which only the first term has been included.<sup>14</sup> The complete series is of the form

$$\left[ \frac{d}{2\pi r_{\text{sep}}} \right]^2 \Rightarrow \sum_{j=1}^{\infty} g^{j-1}(z) \left[ \frac{d}{2\pi r_{\text{sep}}} \right]^{2j}$$

where  $g(z)$  can be expressed as a series of Bessel functions and is plotted in Figure 22. This series is a geometrical progression with a common ratio  $\eta$  which never exceeds a magnitude of 0.25.

$$\eta = g(z) \left[ \frac{d}{2\pi r_{\text{sep}}} \right]^2$$

Hence, the limiting form of Eq. (29) becomes

$$R_w = R \left[ 1 + F + \frac{k_G G \left[ \frac{d}{2\pi r_{\text{sep}}} \right]^2}{1 - g(z) \left[ \frac{d}{2\pi r_{\text{sep}}} \right]^2} \right] \quad (30)$$

for small inter-turn spacings ( $r_{\text{sep}} \cong d$ ).

When a solenoid with more than 2 turns is considered, the field affecting a given turn will be comprised of contributions from each of the other turns with the relative contribution from a given turn proportional to its distance from the turn of interest. Consider the 4-turn solenoid in Figure 23<sup>17</sup> where the magnetic field lines of the solenoid are shown.

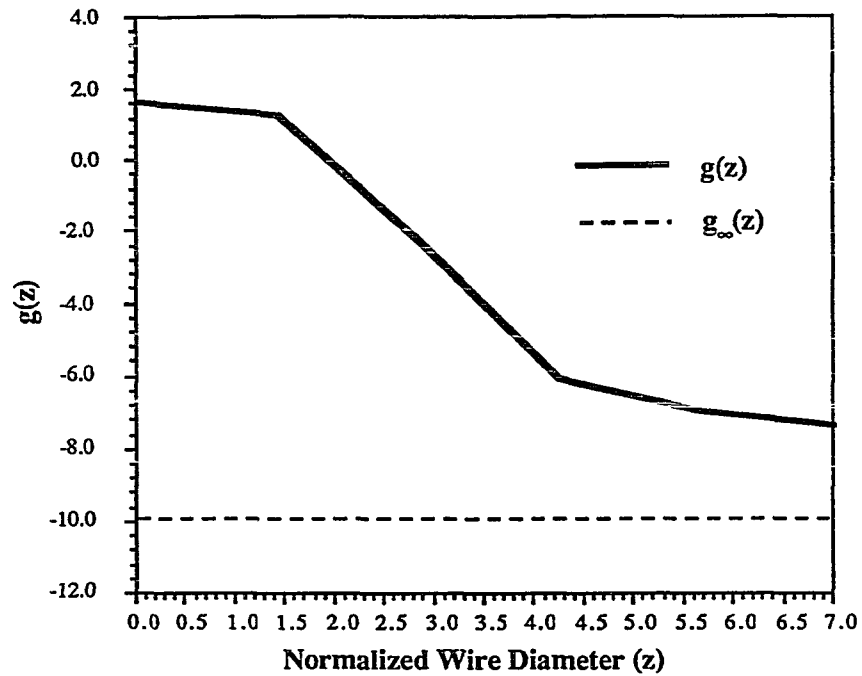


Figure 22 The parameter  $g(z)$  is required to be included with the proximity effect term of Eq. (29) when the wire separation is within 1.5 wire diameters.

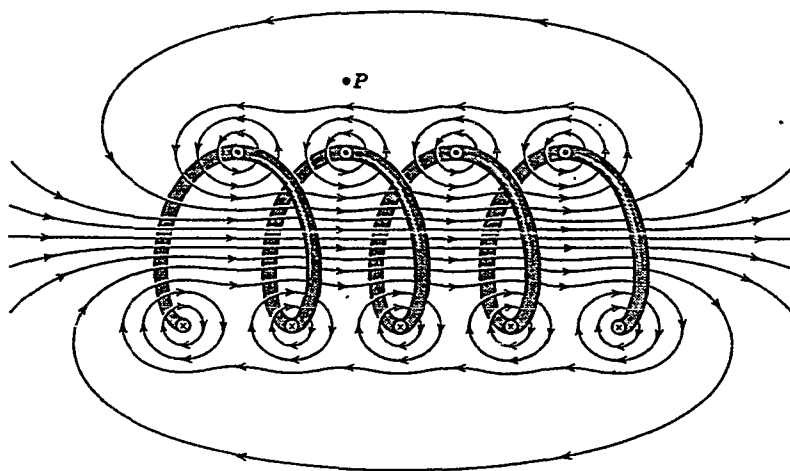


Figure 23 The magnetic field lines of a 4-turn solenoidal coil.

From Ampere's law, the magnetic field affecting a given turn  $n'$  is given by

$$H_{n', \text{total}} = \sum_{i=1}^{n=n'} \frac{I}{2\pi r_{n'i}}$$

In this formula, an approximation is made that the only differential current elements contributing to  $H_{n'}$  are those above and below  $n'$ , separated by a distance  $r_{n'i}$  from the  $i^{\text{th}}$  turn. This is equivalent to assuming that the magnetic field lines through any given turn are completely parallel to the coil axis as shown in Figure 24.

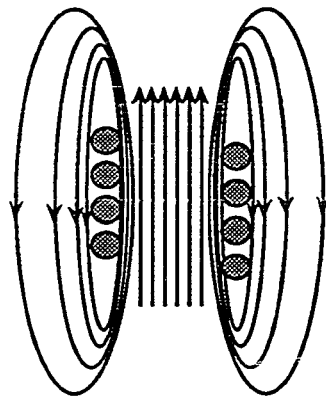


Figure 24 The external magnetic field affecting a particular section of the conductor for a "short" solenoid is dominated by the magnetic field produced by the current flowing in adjacent turns, above and below the point of interest, with minimal effect from the current flowing on the opposite side of the coil.

In reality, for smaller diameter coils the magnetic field  $H_{\text{ext}}$  affecting a differential section of a coil turn would consist of contributions from the entire coil, including contributions from adjacent sections of the same turn. In this case, the net result is that the flux lines would be forced toward the exterior of the coil. The magnetic field through a given turn is now comprised of both a radial component and an axial component as shown in Figure 25. Both components would need to be calculated for every incremental section of the coil, a cumbersome mathematical exercise best left to a

computer. Typically the coil diameter is much greater than the inter-turn spacing so that only the field from the adjacent turns need be considered in determining  $H_n$ . This will be especially true for the turns nearer the center of the coil, as the distance of separation between two outer turns will approach distances equal to the coil diameter for coils that have  $d_{\text{coil}} \cong h$ .

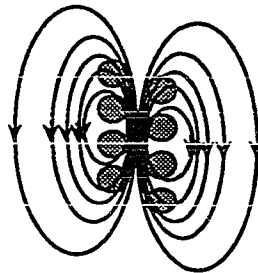


Figure 25 The external magnetic field affecting a particular section of the conductor for a "long" solenoid is composed of contributions from adjacent turns, above and below the point of interest, as well as from the opposite side of the coil.

Consider the magnetic field affecting the second turn of the solenoid, with the separation distances shown in Figure 26. The magnetic field affecting the second turn,  $|H_2|$ , is found by the superposition of contributions from each of the other turns.

$$\begin{aligned}
 H_2 &= \sum_{i=1}^{n \neq i} \frac{I}{2\pi r_{2i}} = \frac{I}{2\pi} \left[ \frac{1}{r_{21}} + \frac{1}{r_{23}} + \frac{1}{r_{24}} \right] \\
 &= \frac{I}{2\pi} \left[ \frac{1}{r_{\text{sep}}} + \frac{-1}{r_{\text{sep}}} + \frac{-1}{2r_{\text{sep}}} \right] \\
 \Rightarrow |H_2| &= \frac{I}{4\pi r_{\text{sep}}}
 \end{aligned}$$

Similarly,

$$|H_1| = |H_4| = \frac{11I}{12\pi r_{sep}}$$

$$|H_3| = |H_2| = \frac{I}{4\pi r_{sep}}$$

The overall field of the solenoid  $H_{\text{sol ext}}$  can then be approximated by the mean-square field.

$$\begin{aligned} |H_{\text{sol ext}}|^2 &= \frac{|H_1|^2 + |H_2|^2 + |H_3|^2 + |H_4|^2}{4} \\ &= \frac{\left[\frac{I}{2\pi r_{sep}}\right]^2 \left[2\left(\frac{11}{6}\right)^2 + 2\left(\frac{1}{2}\right)^2\right]}{4} \\ &= \left[\frac{I}{2\pi r_{sep}}\right]^2 \left[\frac{65}{36}\right] \\ &= |H_{\text{ext}}|^2 [u] \end{aligned}$$

where  $u$  serves as a scaling factor. The scaling factor  $u$  represents the ratio of the actual mean-square magnetic field affecting an arbitrary turn of the solenoid, considering the contributions from all adjacent turns but neglecting the influence from turns on the opposite side of the coil, to that which would be obtained from a single adjacent wire. The value of  $u$  can be determined for a solenoid with an arbitrary number of turns in the same manner as that demonstrated above for a 4-turn solenoid. A plot of  $u$  values for single-layer solenoidal coils with  $n$  turns is given in Figure 27. The limiting value of  $u$  for an infinite number of turns is found by integration to be  $u_\infty = \pi^2/3$ .

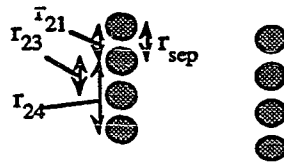


Figure 26 The inter-turn separation of a 4-turn solenoid.

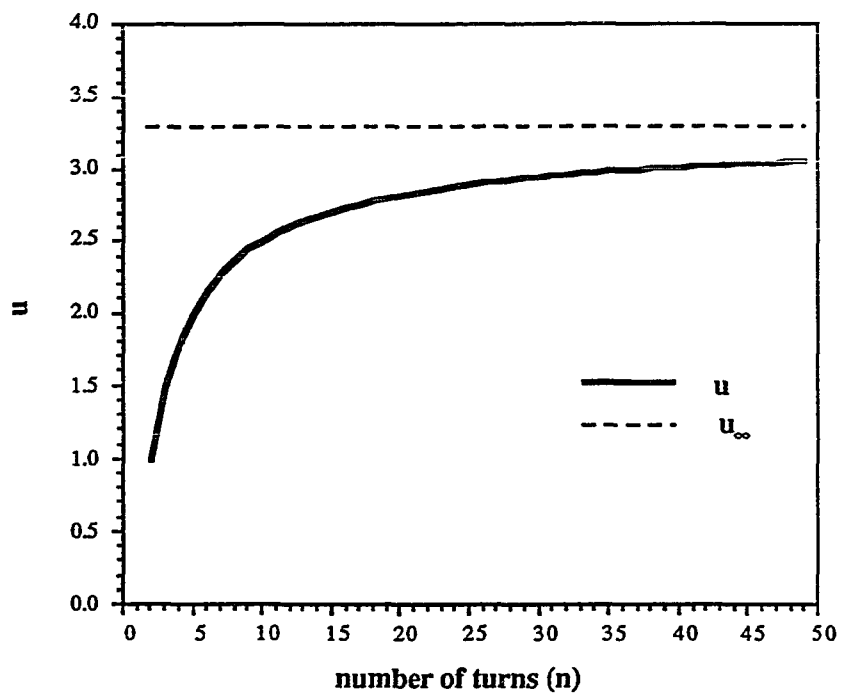


Figure 27 The scaling parameter  $u$  for a solenoidal coils with  $n$  turns.

The total mean-square magnetic field ( $|H_{sol\_ext}|^2$ ) must be used in Eq. (23) for calculating the total coiled-wire loss in the solenoid. The total loss in the wire used in winding the solenoid is found by including the factor  $u$  in Eq. (28).

$$P_w = \frac{1}{2} I^2 R \left[ 1 + F + u k_G G \left[ \frac{d}{2\pi r_{sep}} \right]^2 \right] \quad (31)$$

The total wire resistance is determined from Eq. (29) as

$$R_w = R \left[ 1 + F + uk_G G \left[ \frac{d}{2\pi r_{sep}} \right]^2 \right] \quad (32)$$

where  $R_{prox}$  for the solenoid is given by

$$R_{prox} = u R k_G G \left[ \frac{d}{2\pi r_{sep}} \right]^2 \quad (33)$$

Similarly, for coils with smaller inter-turn spacings ( $r_{sep}/d < 1.5$ ), Eq. (30) is modified as

$$R_w = R \left[ 1 + F + \frac{uk_G G \left[ \frac{d}{2\pi r_{sep}} \right]^2}{1 - g(z) \left[ \frac{d}{2\pi r_{sep}} \right]^2} \right] \quad (34)$$

If the diameter of the coil is small, the flux cuts radially through the turns of the solenoid as shown in Figure 25, and the contribution to  $H_{sol_{ext}}$  from the opposite side of the solenoid cannot be neglected. To account for this, the values of  $u$  are scaled so that the form of the above equations remains unchanged. A modified scaling factor  $u'$  can be defined as the ratio of the actual mean-square field affecting an arbitrary turn of the solenoid, considering both the contribution from adjacent turns and the contribution from the opposite side of the coil, to that which would be obtained from a single adjacent wire.

Consider the on-axis magnetic field produced by a solenoidal coil of  $n$  turns, well inside the coil.<sup>18</sup>

$$H_{\text{sol}} = \frac{n I}{d_{\text{coil}} \sqrt{1 + [h/d_{\text{coil}}]^2}} \quad (35)$$

where  $h$  is the coil length (height). The field outside can be assumed to be approximately zero. Considering a single turn in an infinitely long coil with small diameter, far from either end of the solenoid, the magnetic field intensity varies from  $H_{\text{sol}}$  to zero as one traverses the wire from the inside of the coil to the outside. The spatially averaged magnetic field intensity ( $H'_{\text{sol,ext}}$ ) experienced by the wire can be approximated as  $H'_{\text{sol,ext}} = H_{\text{sol}}/2$ . The scaling factor  $u'$  is therefore defined as

$$u' = \frac{|H'_{\text{sol,ext}}|^2}{|H_{\text{ext}}|^2} = \frac{\left[ \frac{n I}{2 d_{\text{coil}} \sqrt{1 + [h/d_{\text{coil}}]^2}} \right]^2}{\left[ \frac{I}{2\pi r_{\text{sep}}} \right]^2} = \pi^2 \left[ \frac{[h/d]^2}{1 + [h/d]^2} \right] \quad (36)$$

where the relationship  $r_{\text{sep}} = h/(n-1) \cong h/n$  ( $n \gg 1$ ) has been used to account for the winding pitch. From Eq. (36), the limiting value of  $u'_{[h/d_{\text{coil}}]=\infty}$  for an infinitely long coil is  $\pi^2$ . For solenoids of finite length and larger diameter, the magnetic field intensity at the outer perimeter of the sensitive volume of the coil, nearer the turns, is reduced from the value of the on-axis magnetic field given by Eq. (35). Consequently, the value of  $u'$  for finite length solenoidal coils is reduced from that obtained for solenoids of infinite length and predicted by Eq. (36). In the limiting case of a short solenoidal coil, the magnetic field distribution is that of Figure 24, with the proximity effect losses dominated by the magnetic field from adjacent turns rather than the solenoidal magnetic field. Hence, the limiting value of  $u'$  for short coils with many turns is given by  $u'_{[h/d_{\text{coil}}]=0} = u_{n=\infty} = \pi^2/3$ , rather than  $u'_{[h/d_{\text{coil}}]=0} = 0$  as predicted by Eq. (36). The values of  $u'$  for a solenoidal coil with many turns and

$0 \leq h/d_{\text{coil}} \leq 10$  are given as a function of  $h/d_{\text{coil}}$  in Figure 28, approaching a limiting value of  $u'_{[h/d_{\text{coil}}]=0} = u_{n=\infty} = \pi^2/3$  for short coils ( $d_{\text{coil}} \gg h$ ) and  $u'_{[h/d_{\text{coil}}]=\infty} = 3u_{n=\infty} = \pi^2$  for long coils as shown above. For a solenoidal coil of fewer turns, the values of  $u'$  given in Figure 28 can be approximated by scaling by  $u_n/u_{\infty}$  where  $n$  is the number of turns. It should be noted that the degree of error in the calculation of  $H'_{\text{sol}_{\text{ext}}}$  will be higher for those turns nearer to the ends of the coil, as the value of  $H_{\text{sol}}$  is reduced from that which is achieved well inside the coil (and predicted by Eq. (35)). Furthermore, as is evident from Figure 25, the magnetic field intensity for turns near the ends of the coil does *not* vary from  $H_{\text{sol}}$  to zero as one traverses the wire from the inside of the coil to the outside, and the spatially averaged magnetic field intensity ( $H'_{\text{sol}_{\text{ext}}}$ ) experienced by a turn near the ends of the coil *cannot* be approximated as  $H'_{\text{sol}_{\text{ext}}} = H_{\text{sol}}/2$ . Accordingly, the error due to the *end effect* is increased for longer coils (with larger values of  $h/d_{\text{coil}}$ ), particularly those with fewer turns (i.e., wrapped using larger diameter wires and larger inter-turn separation). For shorter coils (smaller values of  $h/d_{\text{coil}}$ ), especially those that are more tightly wound and with a greater number of turns, the magnetic field from the opposite side of the solenoid does not have as great an effect, and the magnetic field affecting a given turn is dominated by the field from adjacent turns, with minimal error due to the end effect. Hence, it should be expected that the proximity effect loss predicted using the above approach will be higher than the actual loss, especially for coils with larger values of  $h/d_{\text{coil}}$ . The overall coil loss, including the proximity effect contribution from the opposite side of the solenoid as well as the proximity effect from adjacent turns, is of the form given by Eq. (32), with  $u$  replaced with  $u'$ .

$$R_w = R \left[ 1 + F + u' k_G G \left[ \frac{d}{2\pi r_{\text{sep}}} \right]^2 \right] \quad (37)$$

If the inter-turn spacing of the coil is small, the form of the loss is given by Eq. (34), with  $u'$ .

$$R_w = R \left[ 1 + F + \frac{u' k_G G \left[ \frac{d}{2\pi r_{sep}} \right]^2}{1 - g(z) \left[ \frac{d}{2\pi r_{sep}} \right]^2} \right] \quad (38)$$

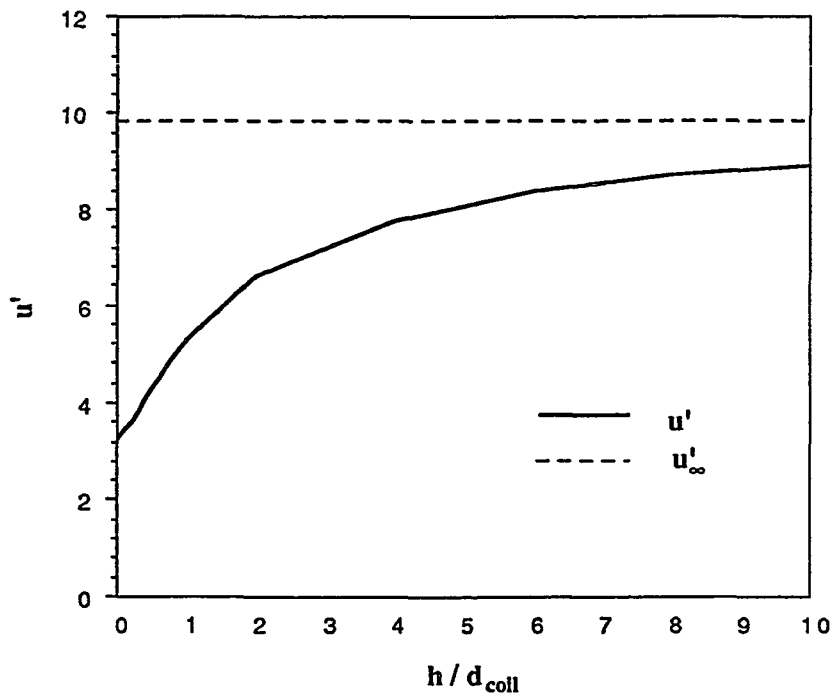


Figure 28 The scaling parameter  $u'$  for a solenoidal coil with a height-to-diameter ratio between 0 and 10.

Summarizing, the total solenoidal coil losses are comprised of the straight-wire losses (dc and skin effect) and coiled-wire losses (proximity effect). Straight-wire losses increase as the diameter is decreased, with the dependency increasing from  $1/d$  to  $1/d^2$  as  $z$  decreases from infinitely large values

toward zero.

$$R_{w_{\text{straight}}} \propto \frac{1}{d^2} [1+F] \propto \begin{cases} \frac{1}{d^2} & z \leq 2 \\ \frac{1}{d} & z > 7 \end{cases} \quad (39)$$

Coiled-wire losses decrease for smaller wires, varying linearly with wire diameter at larger values of  $z$  and increasing to the fourth-power of wire diameter for smaller  $z$ .

$$R_{w_{\text{coiled}}} \propto \frac{1}{d^2} \left[ G \left[ \frac{d}{r_{\text{sep}}} \right]^2 \right] \propto \begin{cases} d^4 & z \leq 2 \\ d & z > 7 \end{cases} \quad (40)$$

Similarly, the straight-wire losses can be represented by skin effect losses at larger values of  $z$  and by dc losses at smaller values of  $z$ . However, due to its dependence on both  $z$  and wire separation, the proximity effect term does not permit such a generalization, and can be significant at low values of  $z$  as well as high values of  $z$ .

### 2.2.2.2 Solenoidal coil resistance models

There are two regimes in which the coil losses are well-behaved. In the macroscopic regime ( $z > 7$ ), both  $F$  and  $G$  vary proportionally to  $z$ , whereas in the microscopic regime ( $z \leq 2$ ), both vary as  $z^4$ . For these two extremes, a more general coil resistance model may be obtained from which the coil noise (Eq. (8)) and the SNR for microcoils may be determined. Such models, while less accurate than the complete model (represented by Eqs. (37) and (38)), are useful when the coils under consideration do not differ substantially in their size, shape, or frequency of operation, and have been used in the past to describe the coil noise when determining the SNR in an NMR experiment.<sup>1,2</sup> It should be emphasized, however, that a complete description of coil loss requires Eq. (37) or

Eq. (38). In the following sections, the limiting regimes ( $z > 7$  and  $z \leq 2$ ) will be considered independently. It will be shown that there is a theoretical advantage in SNR when using microdomain coils for NMR microscopy, regardless of the size regime.

### Macroscopic solenoidal coil resistance model

In the past, the models used to describe coil loss in NMR experiments have included scaling factors to account for the alternating current effects (e.g., skin, proximity, and end effects).<sup>1,2,19</sup> The purpose of this section is to show how these models are derived using the theory outlined above, and to use the models to predict the overall variation in the SNR that can be expected when using such coils for NMR. It has been shown that  $F \gg 1$  in the macroscopic regime. This implies that the current flows uniformly on the perimeter of the wire with a penetration of one skin depth as shown in Figure 14, resulting in a straight-wire resistance given by Eq. (15).

$$R_w \Big|_{z \text{ large}} = \frac{\rho l}{2\pi r \delta} = \frac{\rho l}{\pi d \delta}$$

The determination of the actual coil resistance  $R_c$  requires some knowledge of the coil geometry as both the actual wire length and the increase in resistance due to proximity effect must be included. Consider a 4-turn solenoid with appreciable inter-turn spacing ( $r_{sep}/d > 1.5d$ ) as shown in Figure 29. The form of the coil resistance is given by Eq. (37),

$$R_w = R_{dc} \left[ 1 + F + u' k_G G \left[ \frac{d}{2\pi r_{sep}} \right]^2 \right]$$

where  $R_{dc}$  is the dc coil resistance.

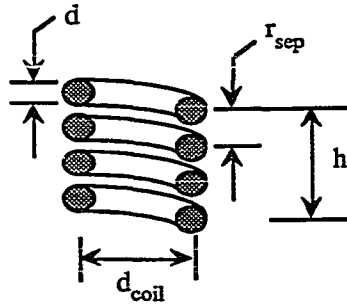


Figure 29 A 4-turn solenoidal coil with diameter  $d_{\text{coil}}$ , height  $h$ , inter-turn separation  $r_{\text{sep}}$  and wound with wire of diameter  $d$ .

The expression for  $R_w$  can be simplified using Eqs. (16) and (25).

$$R_c = R_{dc} \left[ \frac{z}{4} + u' \left[ \frac{z}{8} \right] \left[ \frac{d}{r_{\text{sep}}} \right]^2 \right] \quad (41)$$

The quality factor of the coil is defined as  $Q_c = \omega L/R_c$ . The quality factor is used to gauge the coil's performance with a perfect coil having no loss, i.e.,  $Q_c = \infty$ . It has been shown (Eqs. (39) and (40)) that the straight-wire losses vary inversely with the coiled-wire losses with regard to wire diameter. Hence, there will be an optimal wire diameter which will provide minimum resistance and optimal  $Q$ . For a fixed frequency  $f$ , Eq. (41) can be rewritten in terms of the wire diameter ( $d$ ).

$$\begin{aligned} R_c &= \frac{4\rho l}{\pi d^2} \left[ \frac{d}{4\delta} + \frac{d}{8\delta} u' \left[ \frac{d}{r_{\text{sep}}} \right]^2 \right] \\ &\propto \frac{1}{d} \left[ 1 + \frac{1}{2} u' \left[ \frac{d}{r_{\text{sep}}} \right]^2 \right] \\ &= \frac{1}{d} + \frac{1}{2} u' \frac{d}{r_{\text{sep}}^2} \end{aligned} \quad (42)$$

The optimal wire diameter will be achieved when the rate of increase in straight-wire loss equals the rate of decrease in coiled-wire loss, and is approximately equal to the diameter at which the two terms in Eq. (42) are equal.

$$\frac{1}{d} = \frac{1}{2} u' \frac{d}{r_{sep}^2}$$

$$\Rightarrow \frac{d}{r_{sep}} = \sqrt{\frac{2}{u'}}$$

Considering a spherical sample volume, let  $d_{coil} = h$  so that an optimal filling factor with minimum wire length (and loss) may be achieved. From Figure 28,  $u'_{[h/d_{coil}] = 1} = 5.29$ , assuming an infinite number of turns. The value of  $u'_{[h/d_{coil}] = 1}$  for a 4-turn solenoid is determined as

$$u'_{n=4} \Big|_{d_{coil}=h} = u' \Big|_{d_{coil}=h} \cdot \left( \frac{u_{n=4}}{u_{\infty}} \right)$$

$$= 5.29 \cdot \left( \frac{1.8}{3.29} \right)$$

$$= 2.89$$

Therefore,

$$\frac{d}{r_{sep}} = \sqrt{\frac{2}{2.89}} = 0.832$$

Hence, the optimal inter-turn spacing for a 4-turn solenoid will be  $r_{sep} \cong 1.2$  wire diameters or 2.4 wire radii. For coils with many more than 4-turns but with  $d_{coil} = h$  ( $u'_{[h/d_{coil}] = 1} = 5.29$ ), the optimal inter-turn spacing is approximately 3 wire radii. This value of inter-turn spacing is often quoted as the one which yields an optimal  $Q_c$  for solenoidal coils, and most solenoidal coils are

constructed in this manner.<sup>19</sup> In the present work we have chosen to use 5-turn solenoids with

$$u'_{n=5} = 5.29 \left( \frac{2.01}{3.29} \right) = 3.23$$

for which the optimal inter-turn spacing is  $d/r_{sep} = 0.78$  ( $r_{sep} = 1.3d = 2.6$  wire radii).

The resistance ratio (i.e., the total loss normalized to  $R_{dc}$ ) for a 4-turn solenoidal coil (with  $r_{sep} \cong 1.5d$ ) is given by Eq. (38) and plotted in Figures 30 and 31. For larger values of  $z$ , the proximity effect loss is proportional in magnitude to the skin effect loss. Hence, in the macroscopic solenoid resistance model,  $R_c$  is often derived by first considering only skin effect losses, with proximity effect losses represented by the inclusion of a proximity effect factor  $\xi$ , where  $1 \leq \xi \leq 3$ . Referring to Figure 29, the height of the coil can be expressed in terms of wire diameter as

$$h = (n-1) r_{sep} = (n-1) \left( \frac{3d}{2} \right)$$

Therefore,

$$d = \frac{2h}{3(n-1)}$$

and the length of wire ( $l$ ) given by  $l = n\pi d_{coil}$ . By substituting this value of wire diameter into Eq. (15),

$$\begin{aligned} R_{w \text{ straight wire}} &= \frac{\rho n \pi d_{coil}}{\pi d \delta} = \frac{\rho n d_{coil}}{\left( \frac{2h\delta}{3(n-1)} \right)} \\ &= \frac{3\rho n(n-1)d_{coil}}{2h\delta} \end{aligned}$$

Including  $\xi$  to account for the proximity effect,

$$R_{c_{\text{macroscopic}}} = \frac{3\rho n^2 d_{\text{coil}} \xi}{2h\delta} \quad n \gg 1 \quad (43)$$

Equation (43) is the traditional expression for the high-frequency resistance of a solenoidal coil with  $n \gg 1$ . Note that for the optimum Q coil geometry ( $r_{\text{sep}} = 1.5d$  and  $d_{\text{coil}} = h$ ),  $R_c$  remains insensitive to variations in coil diameter, provided that the number of turns remains constant.

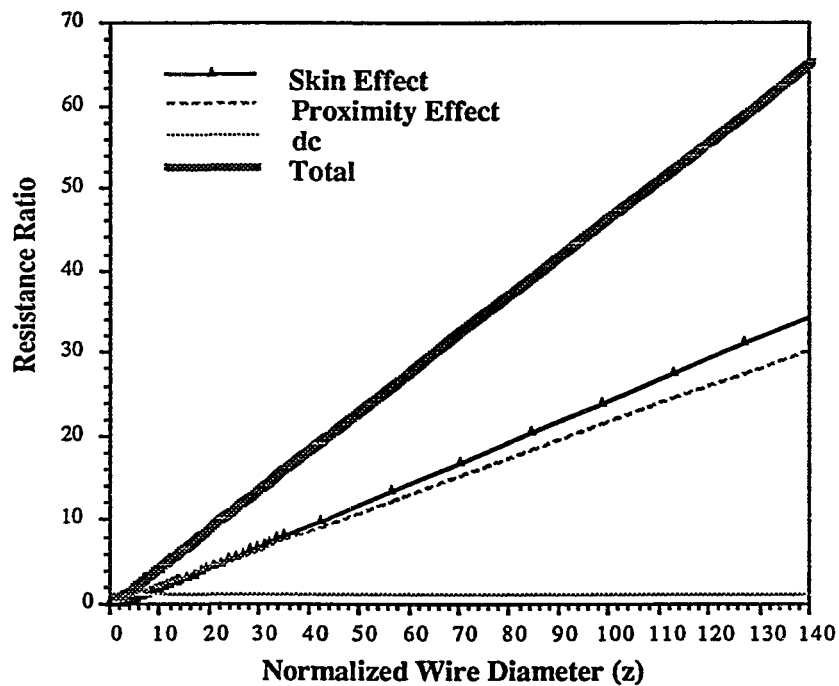


Figure 30 The resistance ratio of a 4-turn solenoidal coil with inter-turn spacing of  $1.5d$  and with coil height equal to coil diameter. Both straight-wire and coiled-wire losses are shown, for  $0.14 \leq z \leq 140$ .

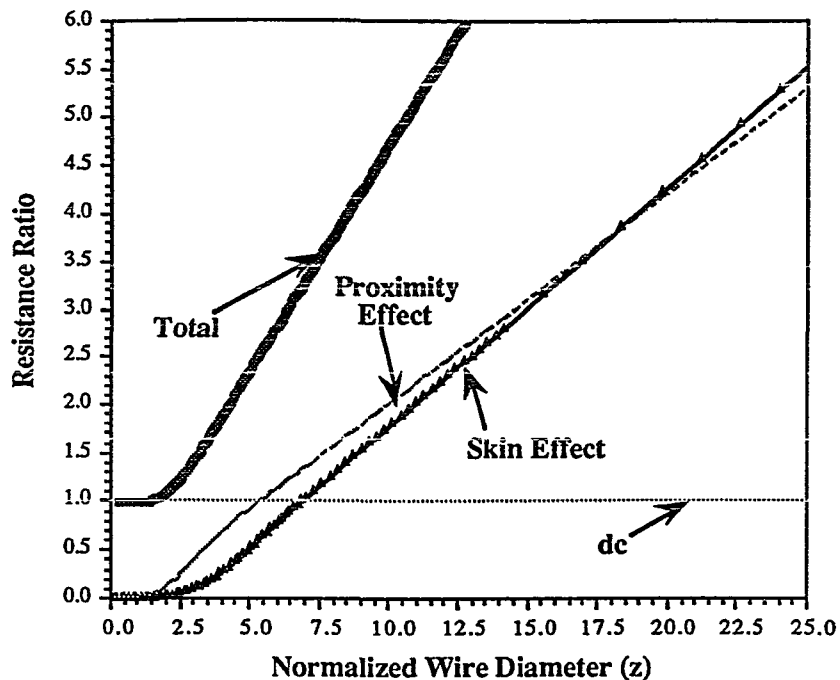


Figure 31 The resistance ratio of a 4-turn solenoidal coil with inter-turn spacing of  $1.5d$  and with coil height equal to coil diameter. Both straight-wire and coiled-wire losses are shown, for  $0.14 \leq z \leq 25$ .

### Microscopic Solenoidal Coil Resistance Model

In the microscopic limit, the current distribution in the solenoid approaches a uniform static (dc) distribution as shown in Figure 10. For this condition,  $F \ll 1$  and straight-wire losses are dominated by the dc losses.

$$R_{w \text{ straight wire}} \Big|_{z \text{ small}} = \frac{4\rho l}{\pi d^2} = R_{dc}$$

The coiled-wire losses must be considered, however, even though  $G \ll 1$ , due to the dependence on the inter-turn spacing. For coils with  $d_{\text{coil}} = h$  and substantial spacing ( $r_{\text{sep}} \geq 1.5d$ ), the coiled-wire

losses may be neglected in the microscopic regime as shown in Figure 31. However, at smaller values of inter-turn spacing, the coiled-wire losses will be larger and may be significant. One could calculate the point at which coiled-wire losses become significant for an extremely small inter-turn spacing. Suppose that  $r_{sep} = 1.1d$  with the turns of the coil nearly touching. Further assume that the coiled-wire losses are counted "significant" when they equal 10% of the dc losses. Equation (38) can be used as an iterative approach to the problem. From Figures 27 and 30, the value of  $z$  at which  $R_{w_{coiled\ wire}} = 0.1R_{w_{straight\ wire}}$  is  $z \cong 2.2$ . Thus, for the microscopic regime ( $z \leq 2$ ),

$$R_c = R_{w_{straight\ wire}} = \frac{4\rho l}{\pi d^2}$$

For purposes of comparison to the macroscopic model, assume the geometry of Figure 29 with  $r_{sep} = 1.5d$  and  $d_{coil} = h$ . The microscopic solenoidal coil resistance is

$$R_{c_{microscopic}} = \frac{9\rho n^3 d_{coil}}{h^2} \quad n \gg 1 \quad (44)$$

Equation (44) is the traditional expression for the static (dc) resistance of a solenoidal coil with  $n \gg 1$ . Contrary to the macroscopic solenoidal resistance (Eq. (40)),  $R_{c_{microscopic}}$  varies with coil diameter, increasing as  $1/d_{coil}$  for coils with  $d_{coil} = h$ .

### 2.2.3 Signal-to-noise ratio

The theoretical SNR achievable using microdomain solenoidal coils and small sample volumes may now be determined. The combination of Eqs. (7) and (8) yields the expression for the SNR

immediately following a  $\pi/2$  pulse

$$\text{SNR} = \frac{\text{rms signal}}{\text{rms noise}} = \frac{k_0 B_1 v_s N \gamma \hbar^2 i(i+1) \omega_0^2 / 3kT_s}{\sqrt{8k_B T_c R_c \Delta f}} \quad (45)$$

where an additional factor of  $1/\sqrt{2}$  has been included in the numerator to account for the rms value (rather than the peak value) of the induced signal. The variation of the SNR in the limiting regimes of  $z \leq 2$  and  $z > 7$  can be determined by Eq. (45), where  $R_c$  is given by Eqs. (43) and (44), and  $\Delta f$  is the bandwidth of the receiver. Equation (45) assumes that a deterministic signal, i.e., a continuous time sinusoid (or group of sinusoids), is being received by the receiving coil. In actuality, the NMR signal is decreasing exponentially in magnitude in accordance with the relaxation of the perturbed system toward its equilibrium state, governed by  $T_1$  and  $T_2$ . Therefore, Eq. (45) is strictly valid only at the instant *immediately* following excitation ( $t = 0^+$ ).

The primary objective of this thesis has been to determine the SNR in an NMR experiment using microcoils. Therefore, in addition to being able to accurately characterize the exact SNR for a given coil under a specific set of experimental and geometric constraints, it is also important to understand the overall variation in SNR as the size of the coil is reduced. By factoring out the experimental constants in the above equation, the SNR is seen to be dependent on the static field precession frequency ( $\omega_0$ ), the RF magnetic field strength ( $B_1$ ), the sample volume ( $v_s$ ), and the coil resistance ( $R_c$ ).

$$\text{SNR} \propto \frac{\omega_0^2 B_1 v_s}{\sqrt{R_c}}$$

It is apparent that a reduction in sample volume ( $v_s \propto b^3$ ) from  $1 \text{ mm}^3$  to  $1 \text{ }\mu\text{m}^3$  yields a signal which is smaller by a factor of  $10^9$  due to the smaller number of nuclei which contribute to the signal.

This loss in signal poses a formidable challenge to microscopic NMR. One can express the SNR normalized per unit sample volume as

$$\text{SNR}_{\text{puv}} \propto \frac{\omega_0^2 B_1}{\sqrt{R_c}} \quad (46)$$

Furthermore, the sensitivity (i.e., the magnetic field produced by a unit current) of a finite length solenoid of  $n$  turns is obtained from Eq. (35) as

$$(B_1/I) = \mu_0 H_{\text{sol}} / I = \frac{\mu_0 n}{d_{\text{coil}} \sqrt{1 + [h/d_{\text{coil}}]^2}} \quad (47)$$

The current ( $I$ ) has been included to further reinforce the definition of sensitivity – it is the magnitude of the magnetic field produced by passing a unit current through the windings of the coil. By reciprocity, sensitivity can also be considered to be the magnitude of the impinging magnetic field required to induce a unit current in the coil. The "per-unit-current" notation will be suppressed throughout the remainder of this thesis, and the symbol  $B_1$  used to represent sensitivity, with an inference to a unit current.

### 2.2.3.1 $\text{SNR}_{\text{puv}}$ ( $d_{\text{coil}} = h$ )

For the optimal Q geometry, Eq. (47) reduces to

$$B_1 \propto \frac{n}{d_{\text{coil}}}$$

The sensitivity of the solenoid is enhanced for smaller coils, varying inversely with coil diameter. A smaller coil couples more strongly to the flux produced by the precessing nuclei of the sample, and is more sensitive to receiving the FID. The number of turns used in wrapping the coil is typically fixed by the sample size and the size of the wire used.

The expression for the resistance of the solenoid ( $R_c$ ) is given by Eqs. (43) and (44). At larger wire sizes and higher frequencies Eq. (46) reduces to

$$\text{SNR}_{\text{puv}} \propto \frac{\omega_0^2 \left[ \frac{n}{d_{\text{coil}} \sqrt{1 + [h/d_{\text{coil}}]^2}} \right]}{\sqrt{\frac{n^2 d_{\text{coil}}}{h}}} \quad (48)$$

$$\propto \frac{1}{d_{\text{coil}}}$$

for the optimal Q geometry and a fixed precession frequency  $\omega_0$ . Hence, the conclusion to be drawn from this analysis is that for a fixed volume of interest, fixed static magnetic field strength, and solenoidal coils in the macroscopic region of operation ( $z > 7$ ), the SNR per unit volume is inversely related to coil diameter and is enhanced for smaller coils.

At smaller wire sizes and lower frequencies Eq. (44) is representative of the coil losses. For this regime, the  $\text{SNR}_{\text{puv}}$  is given as

$$\text{SNR}_{\text{puv}} \propto \frac{\omega_0^2 \left[ \frac{n}{d_{\text{coil}} \sqrt{1 + [h/d_{\text{coil}}]^2}} \right]}{\sqrt{\frac{n^3 d_{\text{coil}}}{h^2}}} \propto \frac{1}{\sqrt{nd_{\text{coil}}}} \quad (49)$$

$$\propto \frac{1}{\sqrt{d_{\text{coil}}}}$$

where the optimal Q geometry and a fixed frequency of precession have again been assumed. Additionally, the number of turns was assumed to be constant over the range of variation in coil diameter. The conclusion to be drawn is that for a fixed volume of interest, fixed static magnetic field strength, and solenoidal coils in the microscopic region of operation ( $z \leq 2$ ), the SNR per unit volume is inversely related to the square root of coil diameter, and is enhanced for smaller coils.

The  $\text{SNR}_{\text{puv}}$  increases as coil diameter is decreased, varying inversely to coil diameter in the macroscopic regime ( $z > 7$ ). The rate of variation decreases in the microscopic regime ( $z \leq 2$ ) to  $1/\sqrt{d_{\text{coil}}}$ . Thus a theoretical improvement in signal-to-noise can be achieved by decreasing the dimensions of the coil so that it wraps around the sample with the highest possible filling factor. While the scaling advantage in  $\text{SNR}_{\text{puv}}$  is most pronounced for larger coils (i.e., coils wound with larger wires and used at higher frequencies) with  $z > 7$ , there is merit in reducing the coil size into the microscopic regime for smaller samples.

For the inter-turn spacing of coils in the microscopic regime, the "optimal Q" spacing of 3 wire radii is not consistent with the microscopic coil model. It has been shown that for  $z \leq 2$  the dc losses dominate all other losses regardless of wire spacing, and increase for smaller wires. Consider a coil in which the turns were nearly touching, e.g.,  $r_{\text{sep}}/d = 1.1$  (see Figure 29). Such a coil would permit the maximum diameter wire to be used while still retaining  $d_{\text{coil}} = h$  for an optimum fit to the spherical sample. For this case,  $h = nd$  and

$$R_{\text{c}_{\text{microscopic}}} \Big|_{r_{\text{sep}}=1.1d} = \frac{4\rho (n\pi d_{\text{coil}})}{\pi (h/n)^2} = \frac{4\rho n^3 d_{\text{coil}}}{h^2}$$

which results in the same  $\text{SNR}_{\text{puv}}$  scaling advantage as before (Eq. (49)) but with an absolute  $\text{SNR}_{\text{puv}}$  greater by a factor of 9/4.

### 2.2.3.2 SNR<sub>puv</sub> (d<sub>coil</sub> ≠ h)

There are instances in which it may be advantageous to use a long or short coil (e.g., with cylindrical samples). It is worthwhile to consider the variation in SNR<sub>puv</sub> as the coil diameter is reduced while maintaining coil height. For this case,

$$\text{SNR}_{\text{puv}} \Big|_{h \neq d_{\text{coil}}} \propto \begin{cases} \sqrt{\frac{h}{d_{\text{coil}}^3 (1+[h/d_{\text{coil}}]^2)}} & z > 7 \\ \sqrt{\frac{h^2}{d_{\text{coil}}^3 (1+[h/d_{\text{coil}}]^2)}} & z \leq 2 \end{cases}$$

For  $h \gg d_{\text{coil}}$ ,

$$\text{SNR}_{\text{puv}} \Big|_{h \gg d_{\text{coil}}} \propto \begin{cases} \frac{1}{\sqrt{d_{\text{coil}} h}} & z > 7 \\ \frac{1}{\sqrt{d_{\text{coil}}}} & z \leq 2 \end{cases}$$

In both the macroscopic and microscopic regimes, the SNR<sub>puv</sub> scales inversely to the square root of the coil diameter when h is fixed and  $h \gg d_{\text{coil}}$ . Similarly, for  $h \ll d_{\text{coil}}$ ,

$$\text{SNR}_{\text{puv}} \Big|_{h \ll d_{\text{coil}}} \propto \begin{cases} \sqrt{\frac{h}{d_{\text{coil}}^3}} & z > 7 \\ \frac{h}{\sqrt{d_{\text{coil}}^3}} & z \leq 2 \end{cases}$$

Again the  $\text{SNR}_{\text{puv}}$  scales equally in both the microscopic and macroscopic regimes, at a rate slightly greater than that obtained when  $d_{\text{coil}} = h$ .

### 2.3 Summary

It has been shown that the signal and noise intensities in an NMR experiment can be theoretically predicted, and that there is an increase in the signal-to-noise ratio that can be achieved from a sample of unit volume using microdomain coils over that which would be obtained using larger coils. Furthermore, the scaling advantage in signal-to-noise afforded by smaller coils continues indefinitely, with the exact relationship dependent on the height-to-diameter ratio of the coil and on the ratio of the wire diameter used in winding the coil to the skin depth of the coil at the frequency of interest. It should be noted, however, that the radius of curvature of the wire must always remain substantially greater than the wire radius. The mechanical stress associated with sharp bending of the wire results in a higher wire resistance and wire loss. Furthermore, the magnetic field in a solenoidal coil with a sharp radius of curvature (i.e., where the diameter of the coil is comparable to several wire diameters) would be nonuniform, as the local magnetic field at a particular point in the sensitive volume of the solenoid would be strongly influenced by the individual turns within close proximity rather than by the collective magnetic field from all of the turns. This implies that there is a minimum diameter coil that can be fabricated, determined by the smallest wire available to wind the coil. Sub-micron conductors can be fabricated using a silicon wafer substrate. The conductor is diffused into the silicon, or evaporated onto the surface, with a typical thickness of  $0.1 \mu\text{m}$ . The lower limit to the width of conductors is dependent upon the lithographic technique employed to replicate the mask pattern onto the photoresist. With conventional light lithography, significant diffraction of the light occurs at the pattern edges, as the wavelength of light is approximately  $0.5 \mu\text{m}$ . Hence, a lower limit to the conductor width using this technique is roughly  $1 \mu\text{m}$ . A greater resolution can be achieved using electron beam lithography, where conductor widths of  $0.05 \mu\text{m}$  have been realized. Technological advancements in microelectronic fabrication will provide the capability of even finer

resolutions; however, a reduction in coil size of two orders of magnitude over that realized in this study is possible using established techniques.

We have characterized the coil signal and noise, and have calculated the signal-to-noise ratio that can be expected using microcoils. The reduced sample volume has a detrimental effect on the SNR. There are many other factors which must be considered in submillimeter NMR. A list of a few of the more fundamental factors is included in Appendix B. Chapter 3 provides a description of the experimental design, construction, and testing of microdomain solenoidal coils. A series of 5-turn solenoidal microcoils with height-to-diameter ratios of  $0.5 \leq h/d_{\text{coil}} \leq 2.0$  has been constructed. The theory presented in this chapter is verified experimentally for these coils, and results are presented which compare the theory with experimental data. The experimental SNR obtained using the microcoils in an NMR spectroscopy experiment at 4.7 T (200 MHz) for  $^1\text{H}$  is presented and compared with the theoretically predicted SNR from Eq. (45).

## 2.4 References

- <sup>1</sup>D. Hoult and R. Richards, "The Signal-to-Noise Ratio of the Nuclear Magnetic Resonance Experiment," J. Magn. Reson. **24**, 71 (1976).
- <sup>2</sup>D. Hoult and P. Lauterbur, "The Sensitivity of the Zeugmatographic Experiment Involving Human Samples," J. Magn. Reson. **34**, 425 (1979).
- <sup>3</sup>A. Abragam, Principles of Nuclear Magnetism (Oxford University Press, Oxford, 1961).
- <sup>4</sup>D. Bell, Electrical Noise (D. Van Nostrand Company, LTD, London, 1960).
- <sup>5</sup>Raleigh, Phil. Mag. **382** (1886).
- <sup>6</sup>Z. Cho, C. Ahn, S. Juh, and H. Lee, "Nuclear Magnetic Resonance Microscopy with 4  $\mu\text{m}$  Resolution: Theoretical Study and Experimental Results," Med. Phys. **15** (6), 815 (1988).
- <sup>7</sup>Rosa and Grover, Bureau of Standards Bulletin, Scientific Paper No. 169, 226 (1912).
- <sup>8</sup>S. Mead, "Wave Propagation Over Tubular Conductors: The Alternating Current Resistance," Bell System Technical Journal **327** (1912).
- <sup>9</sup>A. Kennelly, F. Laws, and P. Pierce, "Experimental Researches on Skin Effect in Conductors," Trans. A.I.E.E. **1953** (1915).

- <sup>10</sup>H. Dwight, "Proximity Effect in Wires and Thin Tubes," Trans. A.I.E.E. 850 (1923).
- <sup>11</sup>P. Turner, "H.F. Resistance," Wireless Engineer 24, 134 (1926).
- <sup>12</sup>F. Terman, "Some Possibilities for Low-Loss Coils," Proc. I.R.E. 23, 1069 (1935).
- <sup>13</sup>R. Medhurst, "H.F. Resistance and Self-Capacitance of Single-Layer Solenoids," Wireless Engineer 24, 35, 80 (1947).
- <sup>14</sup>S. Butterworth, "Effective Resistance of Inductance Coils at Radio Frequency," Wireless Eng. 3 203, 302, 417, and 483 (1926).
- <sup>15</sup>W. Hayt, Jr., Engineering Electromagnetics (McGraw-Hill Book Company, New York, 1981).
- <sup>16</sup>D. Cheng, Field and Wave Electromagnetics (Addison-Wesley Publishing Company, Inc., Reading, 1991).
- <sup>17</sup>D. Halliday and R. Resnick, Physics (John Wiley & Sons, New York, 1978), p. 756.
- <sup>18</sup>J. Kraus, Electromagnetics (McGraw-Hill Book Company, New York, 1953).
- <sup>19</sup>F. Terman, Radio Engineers' Handbook (McGraw-Hill Book Company, New York, 1943).

### 3. EXPERIMENTAL METHODS AND RESULTS

The focus of this thesis has been to consider what is perhaps the most crucial technical challenge which exists in the examination of microscopic structures using nuclear magnetic resonance: obtaining an adequate signal-to-noise ratio. Observation of microscopic processes and structures has in the past been restricted to optical microscopy, electron microscopy, or other nonNMR modalities. NMR complements these existing methods by providing the capability of examining the internal structure of an object noninvasively without damaging the specimen being examined. However, the NMR signal received from a microscopic sample volume is extremely weak due to the relatively few number of nuclei and the inherently low sensitivity of nuclear magnetic resonance. Larger coils do not possess sufficient sensitivity to detect these weak signals. Therefore, the design of smaller, more sensitive coils is required for signal reception in NMR microscopy. Chapter 2 has examined the signal-to-noise ratio for NMR microscopy and has shown the theoretical advantage of using microcoils to examine small sample volumes. Chapter 3 provides a description of the experimental plan for designing, constructing, and testing microcoils with diameters between 38  $\mu\text{m}$  and 1.8 mm. Following a brief overview of previous research using small coils with diameters greater than 1 mm, the theoretical models derived in Chapter 2 are empirically verified. A computer program which uses these coil models has been developed to assist in the prediction of microcoil behavior, with some computational results given. The details of microcoil construction are presented and electrical results (e.g., inductance, high-frequency resistance, and coil Q) are provided. Finally, the results obtained by using microcoils in NMR experiments at 200 MHz (4.7 T) for  $^1\text{H}$  are given. It will be shown that the empirical SNR compares well with the theoretical expectations, and that further enhancement to the SNR should be possible using microcoils with diameters less than 38  $\mu\text{m}$ . The construction of such microcoils requires microelectronic fabrication technology and is not included in this thesis.

### 3.1 Background

Odeblad<sup>1</sup> successfully employed microcoils for NMR spectroscopy as early as 1966. In his study he used solenoidal microcoils with diameters of several millimeters to obtain line spectra of secretions from single glandular units in the human uterine cervix. The small coil sizes provided improved filling factor and enhanced sensitivity for examination of the small sample volume.

Clark et al.<sup>2-4</sup> investigated microcoils for applications in both nonresonant (swept frequency) NMR spectroscopy and low-frequency electron spin resonance (ESR) spectroscopy. Solenoidal coils with diameters less than 1 mm and lengths exceeding 1 mm were used to measure magnetic susceptibility and relaxation times of small polycrystalline samples at low temperatures ( $T \approx 20\text{K}$ ). Along with providing an improved filling factor, the small coils were broadband. A broadband coil with a high filling factor was preferred in this application because of the need to cover a wide frequency range in swept frequency NMR.

In NMR imaging, image resolution is limited by the available SNR for a given voxel in the region of interest.<sup>5</sup> Hedges<sup>6</sup> reported the use of a 1.8 mm diameter solenoidal microcoil in conjunction with 7.2 G/cm gradient field coils for imaging an aquatic snail of less than 1 mm diameter with an isotropic resolution of  $35 \times 35 \times 125 \mu\text{m}$ . The microcoil was designed to provide an enhanced sensitivity to the low-level signal. This was one of the first attempts at microscopic imaging, demonstrating the advent of the NMR imaging microscope.

Aguayo et al.<sup>7</sup> used microcoils with high strength gradient field coils ( $G \approx 20 \text{ G/cm}$ ) for imaging a single African toad ovum. Good sensitivity was obtained using a 5 mm diameter solenoidal microcoil with a 9.5 T high field magnet. The image produced exhibited a  $10 \mu\text{m}$  in-plane resolution (and a  $250 \mu\text{m}$  slice thickness). This was one of the first studies to attempt NMR imaging of a single (isolated and quite large) cell.

In more recent studies, Cho et al.<sup>8</sup> used microcoils (diameters to 1 mm) in conjunction with ultrahigh strength gradient field coils ( $\approx 800 \text{ G/cm}$ ) at 7.05 T to obtain images of rat embryos with  $15 \mu\text{m}$  in plane resolution (using a  $100 \mu\text{m}$  slice thickness). However, the highest recorded isotropic

resolution attained by NMR microscopic imaging techniques was reported by Zhou et al.<sup>9</sup> By using a 2.9 mm diameter microdomain receive coil in conjunction with 10 G/cm gradient field coils, an image voxel resolution of  $(6.37 \mu\text{m})^3$  was recorded. The object imaged was a  $24.7 \mu\text{m}$  (volume =  $7890 \mu\text{m}^3$ ) polystyrene bead in a  $\text{CuSO}_4$ -doped agarose gel.

## 3.2 Methods

All of the microcoil NMR research projects described above used small coils with diameters of  $1000 \mu\text{m}$  or greater to enhance the signal-to-noise ratio during signal reception from the volume of interest. We have developed and tested new coils with diameters as small as  $38 \mu\text{m}$ , roughly two orders of magnitude smaller than those presently used. We begin with empirical verification of the theory derived in Chapter 2, from which a computer model has been written to assist in the prediction of microcoil performance. The method of constructing the microcoils is described, and results of electrical testing of the microcoil parameters (e.g., resistance, inductance, and quality factor) is provided. Finally, experimental verification of the SNR using microcoils in  $^1\text{H}$  NMR spectroscopy at 200 MHz ( $B_0 = 4.7 \text{ T}$ ) is provided, in which good agreement is obtained with the theoretically predicted SNR in Chapter 2. The results demonstrate that there is an advantage in the SNR achieved at submillimeter dimensions when using microdomain RF coils.

## 3.3 Results

### 3.3.1 Empirical verification of wire loss

Some assumptions were made in the derivation of the coil resistance models in Chapter 2, particularly in the proximity effect loss term, where an approximate "mean square" magnetic field is used in calculating the losses. Therefore, the coil-loss models must be empirically verified before they are implemented into the computer program. This requires the experimental determination of the losses

in the wires used to wind the microcoils. The microcoils used in the present work were wound using copper and gold wires with diameters of  $12 \mu\text{m} \leq d \leq 65 \mu\text{m}$ . Testing of such wires to determine their losses at alternating frequencies should cover the regime  $0.1 \leq z \leq 20$  in order to insure adequate verification of both the microscopic and macroscopic regimes. For the smaller wires, this would require frequencies in excess of 1 GHz. There are substantial difficulties in testing coils at such high frequencies. Parasitic effects from stray electric and magnetic fields can lead to measurement inaccuracies. Specially designed test fixtures to minimize stray fields are expensive and were not readily available for the present research. In addition, the coil Q (i.e., the ratio of the reactive component of the coil impedance to the resistive component) scales linearly with frequency. At high frequencies, the coil impedance is mostly reactive. As such, the resolution with which the resistive component can be measured is severely reduced and is often inaccurate. While Q meters have been designed for such measurements at lower frequencies, these instruments are not available for measurements above several hundred MHz.

The theoretical wire losses derived in Chapter 2 involve the scaling parameter  $z = d/\delta$  where  $d$  is the diameter of the wire used in winding the coils and  $\delta$  is the skin depth at the frequency of interest. An advantage in using such a scaling parameter is that the experimental verification of the losses in the coils can be performed at lower frequencies using larger wires. Therefore, the verification of the losses was accomplished using 16 ga copper wire, where the regime  $0.1 \leq z \leq 20$  corresponds to  $26 \text{ Hz} \leq f \leq 1 \text{ MHz}$ . At these lower frequencies, the coil Q is lower, and sophisticated instrumentation is available to accurately characterize coil resistance.

The geometry of the larger solenoids must mimic that of the microcoils if the losses in the two are to be compared. The microcoils used in this research consisted of 5-turn solenoidal coils with an inter-turn spacing of  $r_{\text{sep}} = 2d$ . The microcoils were wound using 42 ga copper wire and 50 and 56 gauge gold wire, with a ratio of coil height to coil diameter given by:  $0.25 \leq h/d_{\text{coil}} \leq 2.5$ . At the frequency of interest (200 MHz), wires of this size correspond to  $2.24 \leq z \leq 13.54$ . A series of five 5-turn solenoidal coils were constructed of 16 ga copper wire with the same inter-turn spacing

( $r_{sep} = 2d$ ) and coil height to coil diameter ratio ( $0.3 \leq h/d_{coil} \leq 2.9$ ). The dimensions of the coils are shown in tabular form in Table 1.

TABLE 1 DIMENSIONS OF THE SOLENOIDAL COILS WOUND WITH 16 GA WIRE AND USED TO VERIFY THE THEORETICAL COIL-LOSS MODELS OF CHAPTER 2.

Coil #	Diameter ( $d_{coil}$ )	height (h)	$h/d_{coil}$
A	3.9 cm	1.2 cm	.3
B	2.6 cm	1.2 cm	.5
C	1.1 cm	1.2 cm	1.1
D	0.6 cm	1.2 cm	2.0
E	0.45 cm	1.3 cm	2.9

The coil resistance was characterized over the frequency range  $26 \text{ Hz} \leq z \leq 1 \text{ MHz}$  using an HP4284A LCR meter. The resistance ratio for a straight 16 ga wire is shown in Figure 32.

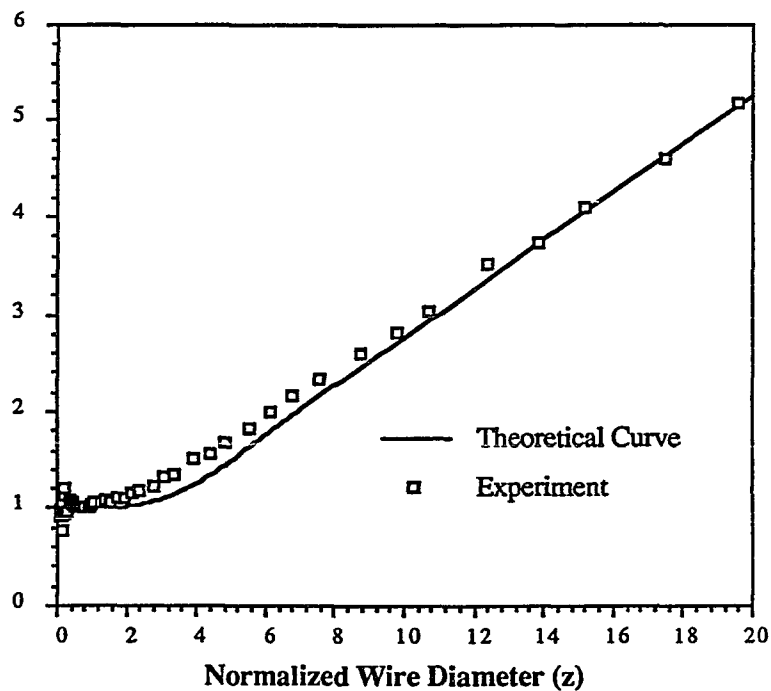


Figure 32 Resistance ratio of a straight, 16 ga copper wire.

The straight-wire losses for the 16 ga wire compare favorably with the theoretical predictions of Chapter 2, with the most-significant variation from theory occurring in the intermediate regime ( $2 < z \leq 7$ ) where the theoretical model is less well-defined. As shown in Figure 32, the experimental results are very well-characterized by the theory in both the microscopic ( $z < 2$ ) and macroscopic ( $z > 7$ ) regimes. As to the coiled-wire losses, the resistance ratio (considering both straight- and coiled-wire losses) of each of the coils (A-E) is shown in Figures 33-37, respectively, as a function of the scaling parameter  $z$ .

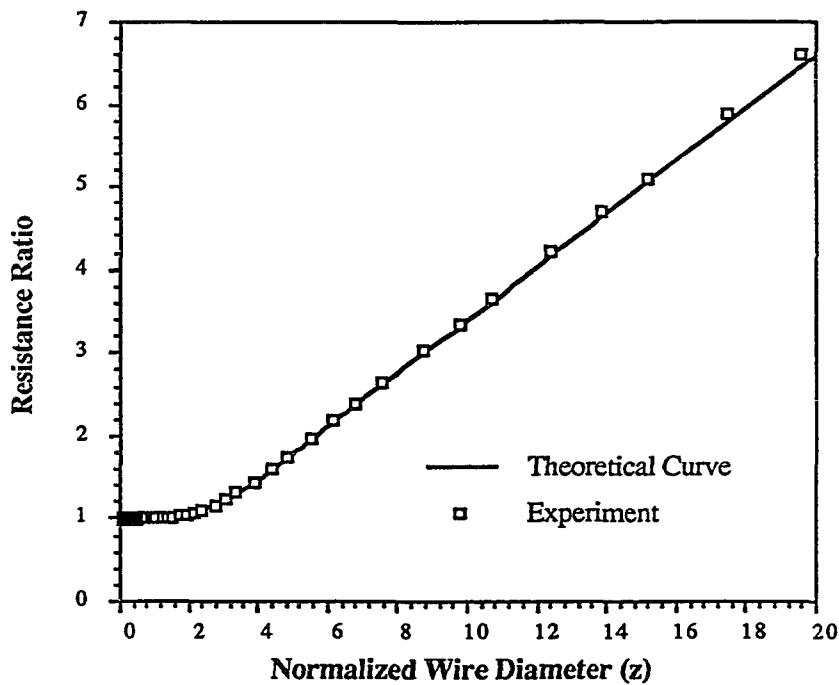


Figure 33 Total resistance ratio for Coil A.

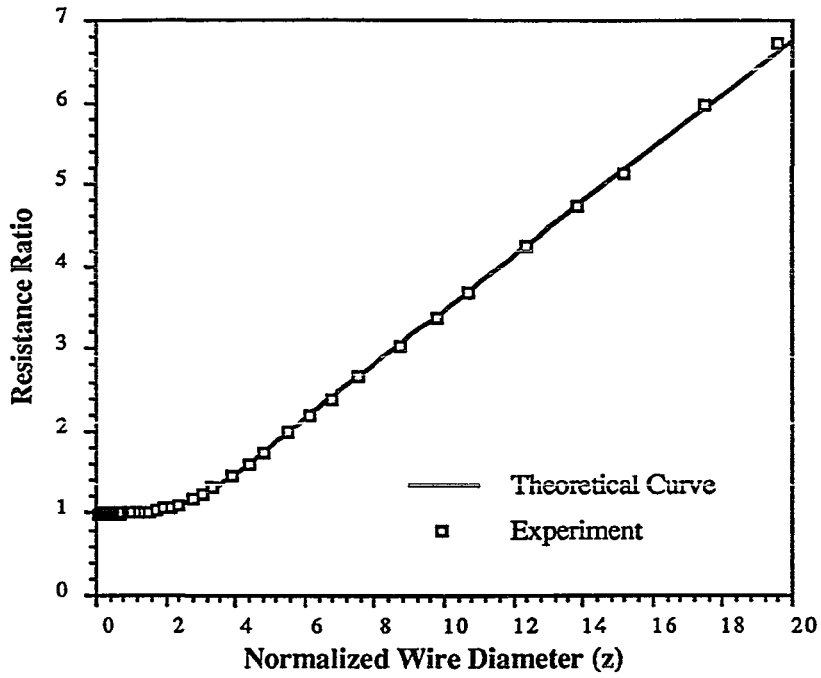


Figure 34 Total resistance ratio for Coil B.

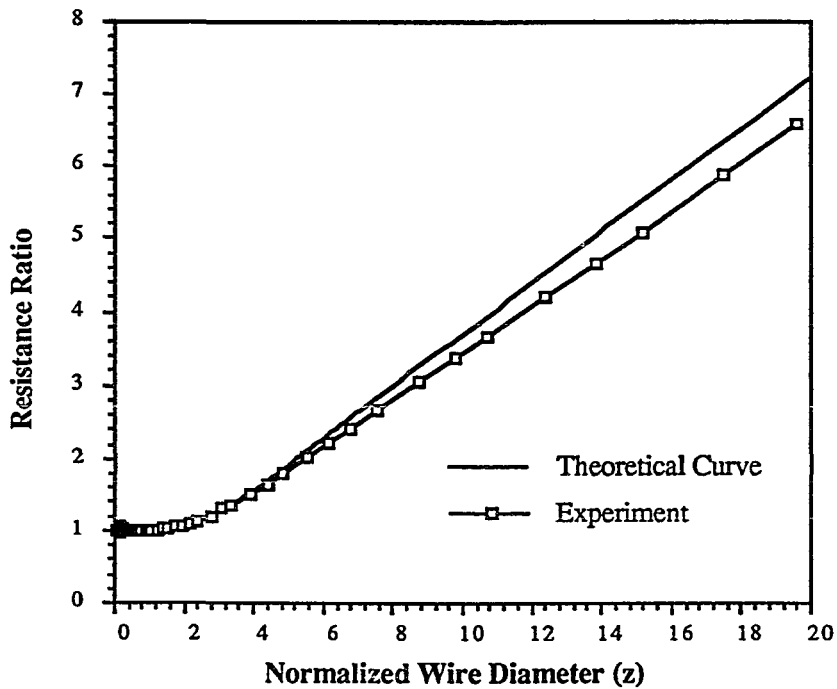


Figure 35 Total resistance ratio for Coil C.

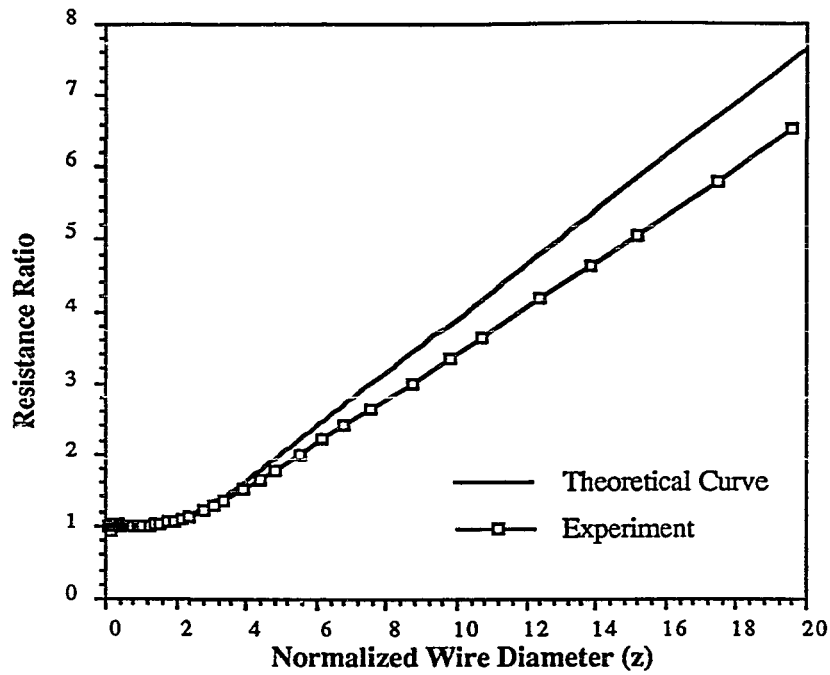


Figure 36 Total resistance ratio for Coil D.

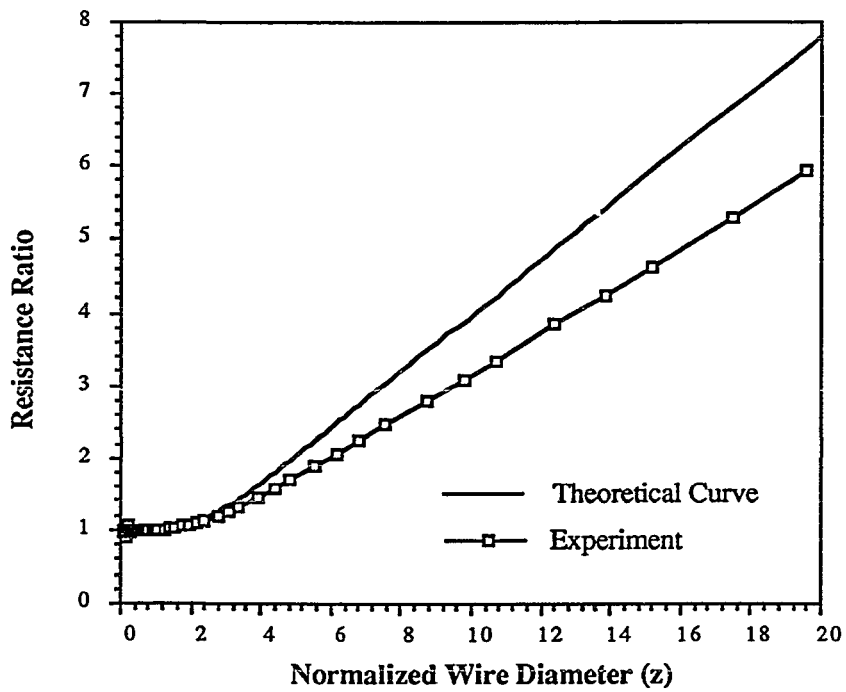


Figure 37 Total resistance ratio for Coil E.

It was stated in Chapter 2 that the theoretically estimated proximity effect losses would likely be in excess of the actual proximity effect losses for coils with  $h/d_{\text{coil}} > 1$ , due to the *end effect*. Furthermore, it was stated that the error due to the *end effect* would be greater for longer coils (with larger values of  $h/d_{\text{coil}}$ ), particularly those with fewer turns (i.e., wrapped using larger diameter wires and larger inter-turn separation). For shorter coils (smaller values of  $h/d_{\text{coil}}$ ), especially those that are more tightly wound and with a greater number of turns, the magnetic field from the opposite side of the solenoid does not have as great an effect, and the magnetic field affecting a given turn is dominated by the field from adjacent turns, with minimal error due to the end effect. Figures 33-34 reveal that the overall losses in Coil A and Coil B are very accurately predicted using the theoretical model. However, the theoretical losses overestimate the actual losses in Coils C-E as shown in Figures 35-37, with the error increasing with larger  $h/d_{\text{coil}}$ . The theoretically predicted losses for Coil E are in error by over 20%. Figure 38 is an error curve for the above graphs and is a measure of the discrepancy between the theoretically calculated losses and the experimentally measured losses as a function of  $h/d_{\text{coil}}$ . It is evident from Figure 38 that the theoretical estimations of total coil loss are in excess of the actual coil losses for values of  $h/d_{\text{coil}} > 0.5$ . Most of the microcoils used for this study fall within the regime  $0.5 \leq h/d_{\text{coil}} \leq 2.0$ , and will have losses which fall short of the theoretical predictions.

From Figure 38 it is evident that the a scaled version of the theoretical loss predicted in Chapter 2 is necessary to account for the end effects of longer solenoidal coils. Furthermore, since the severity of the end effect is dependent on the number of turns, the scaling constant should itself be functionally dependent on the number of turns. We will refer to the scaling constant as the "end effect factor" ( $\zeta$ ). It has been suggested<sup>1,10</sup> that for coils with  $2 < n \leq 10$ ,  $\zeta$  is given by

$$\zeta = \frac{\sqrt{n-1}}{3}$$

The end effect factor can be included in the expression for total coil loss. The microcoils used in this study had an inter-turn spacing of  $r_{sep}/d = 2$ , hence a total loss of the form given by Eq. (37):

$$R_w = R_{dc} \left[ 1 + F + u'k_G G \left[ \frac{d}{2\pi r_{sep}} \right]^2 \left[ \frac{\sqrt{n-1}}{3} \right] \right] \quad (50)$$

where  $R_{dc}$  is the dc coil resistance and the end effect factor has been appended to the proximity effect term. The theoretical losses predicted using Eq. (50) can be compared to the experimental losses in Figures 34-37, and is given in Figure 39.

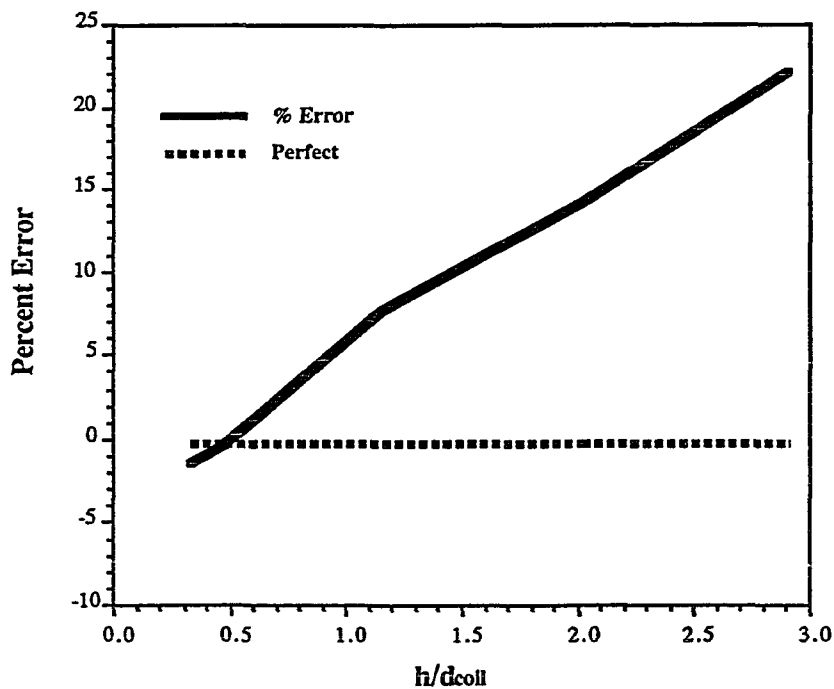


Figure 38 Error in the theoretical calculation of total loss for Coils A-E when compared to empirical results. A positive error indicates that the theoretical estimation exceeds the empirical result.

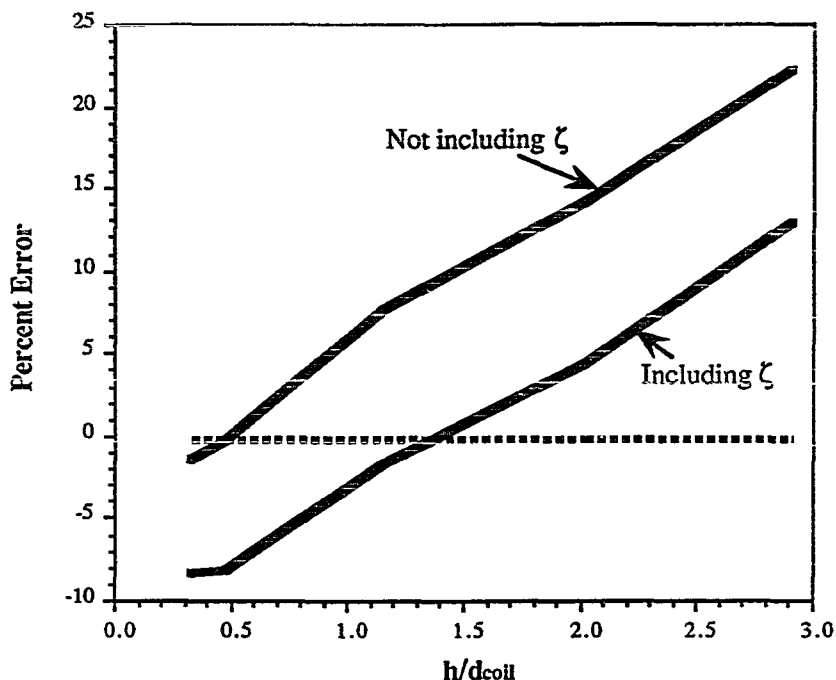


Figure 39 Error in the theoretical calculation of total loss for Coils A-E, including the end effect factor, when compared to empirical results. A positive error indicates that the theoretical estimation exceeds the empirical result.

The theoretical and experimental losses show much better agreement than before the inclusion of the end effect factor, with a maximum error of  $\pm 13\%$ . Furthermore, the error approaches zero at  $h/d_{coil} \cong 1.4$ , approximately in the middle of the size regime ( $0.5 \leq h/d_{coil} \leq 2.0$ ) of the microcoils used in this study. The conclusion to be drawn is that the losses in coils with  $0.5 \leq h/d_{coil} \leq 2.0$ , fewer turns ( $2 \leq n \leq 10$ ), and reasonable inter-turn separation ( $r_{sep} \geq 1.5d$ ), can be predicted to within  $\pm 15\%$  by Eq. (50).

An important aspect of verifying the theory, by using Coils A-E to obtain the graphs presented in this section, is to arrive at a suitable model to predict the loss (and the noise) of 5-turn solenoidal microcoils. It has been shown (Figure 28) that the value of  $u'$  varies substantially with  $h/d_{coil}$  for coils with many turns. The results of Figure 39 would suggest that, for the special case of 5-turn

solenoidal coils within the range  $0.5 \leq h/d_{\text{coil}} \leq 2.0$ , this variation would appear to be less substantial. The value of  $u'$  for a 5-turn coil with  $h/d_{\text{coil}} = 1$  is given from Chapter 2 as  $u' = 3.23$ . If this value of  $u'$  is used for the calculation of theoretical losses in Coils A-E, the error is reduced to less than  $\pm 2\%$  as shown in Figure 40. Therefore, Eq. (50) is used, with a constant value of  $u' = 3.23$ , to represent the losses in the microcoils used in this study. The numerical results provided by this method (for 5-turn solenoidal coils with  $d/r_{\text{sep}} = 0.5$  and  $0.5 \leq h/d_{\text{coil}} \leq 2.0$ ) are equivalent (to within 1%) to the results suggested by Odeblad,<sup>1</sup> which he obtained using empirical data published earlier by Medhurst.<sup>10</sup> The following section describes a computational model that has been developed using the theory of Chapter 2 and the empirical results described above.

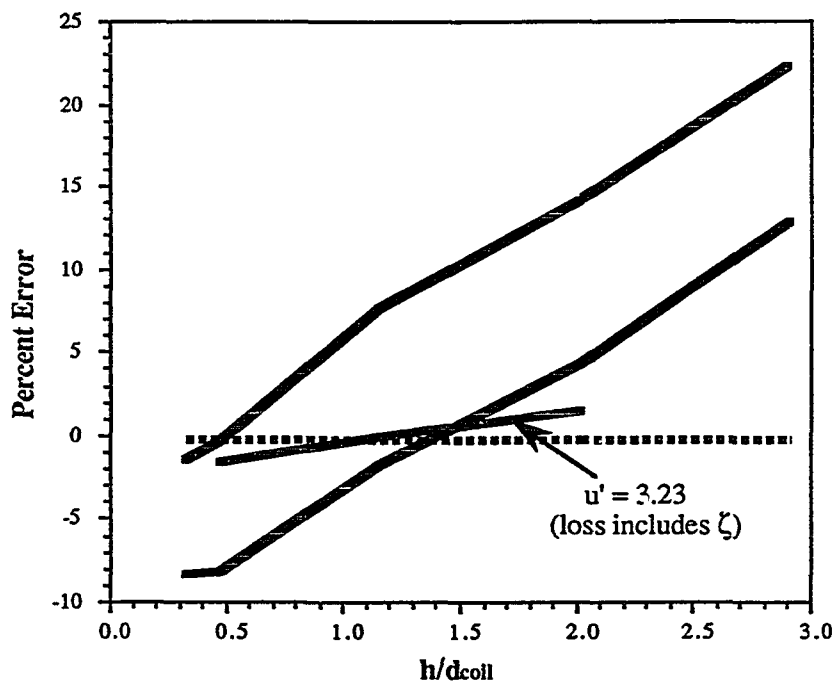


Figure 40 Error in the theoretical calculation of total loss for Coils A-E, using  $u' = 3.23$ , when compared to empirical results. A positive error indicates that the theoretical estimation exceeds the empirical result.

### 3.3.2 Development of a computational model

A computer model has been developed to assist in the prediction of coil performance and signal to noise. The program is written in FORTRAN and designed for execution on an IBM AT class personal computer. Inputs to the program include wire type, coil diameter, and operating frequency, with an output of the expected signal and noise. Additionally, the electrical parameters of the coil (e.g., inductance and self-resonant frequency) are calculated. The program is not adequately sophisticated to determine the coil losses over the entire range  $0.1 \leq z \leq 150$ . Rather, coils with  $z \leq 2.5$  are classified as being within the microscopic regime, and the coil loss is determined by Eq. (44), modified to account for the proper inter-turn spacing ( $r_{sep}/d$ ). Coils with  $z > 2.5$  are classified as being within the macroscopic regime. The loss for these coils is determined using Eq. (50), as described in the previous section. It should be noted that the decision of *either* the macroscopic regime *or* the microscopic regime corresponds to a crude estimation, where a piecewise approximation is used to represent the coil loss. Accordingly, the error will be greatest for coils with the intermediate regime ( $2 \leq z \leq 7$ ). The loss for Coil C ( $h/d_{coil} = 1$ ), predicted using this crude approximation, is compared to the actual loss in Figure 41. A maximum error of 15% for coils in the regime  $2.0 \leq z \leq 3.0$  results from this approximation.

The computer program is designed to array the input parameters to predict coil behavior over a range of input values (e.g.,  $SNR_{puv}$  vs.  $d_{coil}$  for  $100 \mu\text{m} < d_{coil} < 1 \text{ mm}$ ). The program is adequately sophisticated to account for the loss contribution from the leads of the microcoil. For smaller microcoils ( $d \leq 100 \mu\text{m}$ ), the loss in the leads can be substantial and must be taken into account when calculating the SNR.

A postprocessing program was developed to sort the data selectively for output to a plotting routine. Figure 42 is a plot of the magnitude of signal and noise expected from a 5-turn microcoil made of 50 ga gold wire in the macroscopic regime ( $z > 2.5$ ), and is plotted against the diameter of the microcoil.

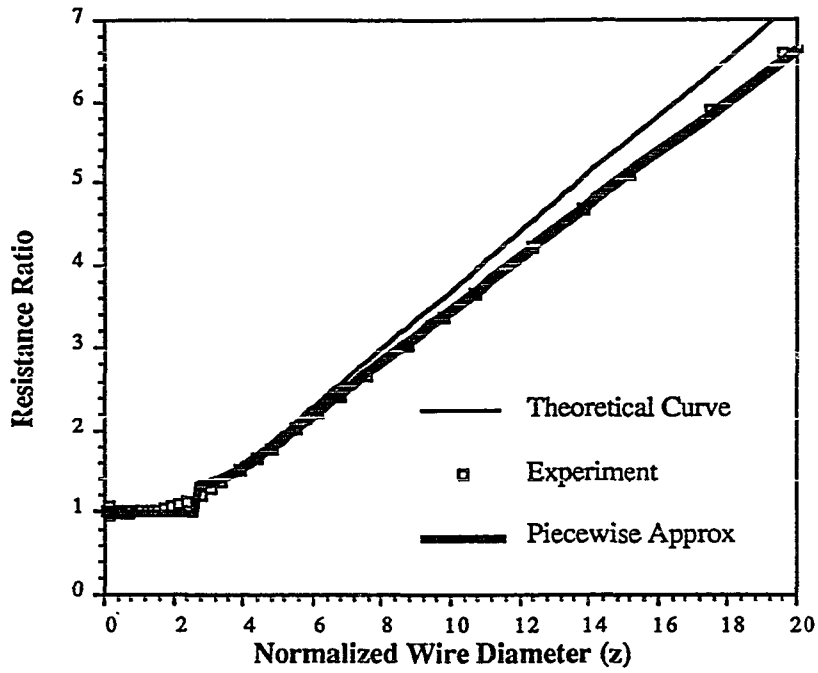


Figure 41 Total resistance ratio for Coil C, using a piecewise approximation in which the microscopic regime corresponds to  $z \leq 2.5$  and the macroscopic regime corresponds to  $z > 2.5$ .

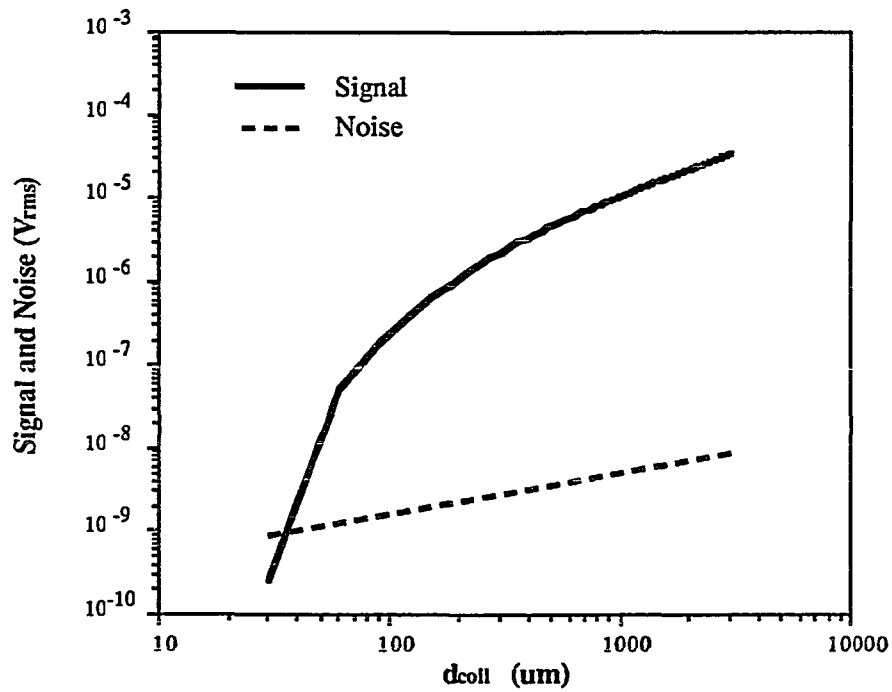


Figure 42 Signal and noise for a 5-turn solenoidal microcoil operated in the macroscopic regime.

Figure 43 is a plot of the normalized SNR for microcoils made of 50 ga gold wire and operated in the macroscopic regime, and clearly demonstrates the inverse variation of the  $\text{SNR}_{\text{puv}}$  with  $d_{\text{coil}}$  as predicted by Eq. (48).

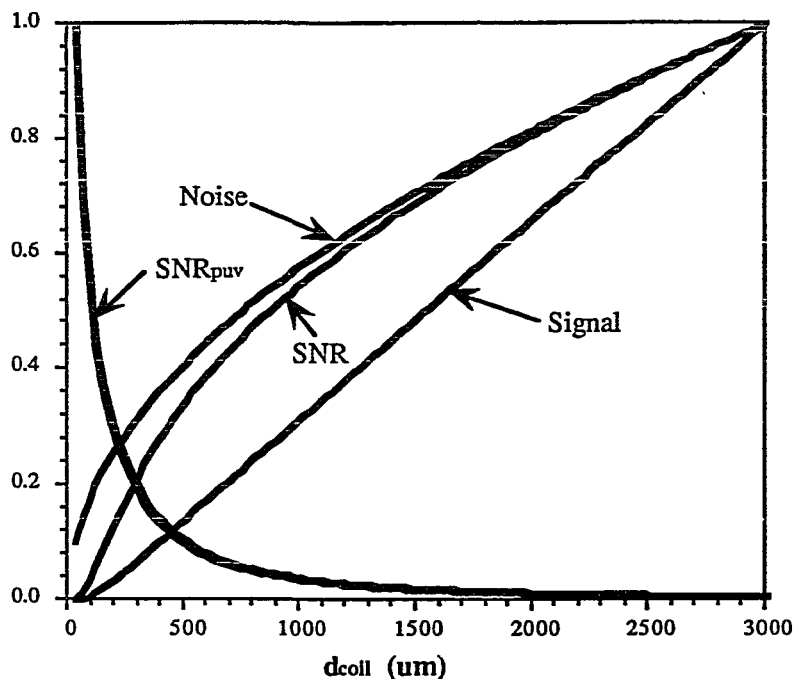


Figure 43 Signal, noise, and  $\text{SNR}_{\text{puv}}$  for a 5-turn solenoidal microcoil operated in the macroscopic regime ( $z > 2.5$ ).

The computer model also provides the theoretical dependence of the electrical parameters of the coil on variations in coil size. The inductance of a 5-turn microcoil wound with 50 ga gold wire is shown in Figure 44 as a function of coil diameter. The inductance of a solenoid is seen from Figure 44 to be directly proportional to the diameter of the solenoid. In Figures 42-44 the wire diameter ( $d$ ) and number of turns ( $n$ ) are assumed to remain constant, hence some minor variation from the condition  $d_{\text{coil}} = h$ . All of the theoretical data in Figures 42-44 correspond to an operating frequency of  $f_0 = 200$  MHz.

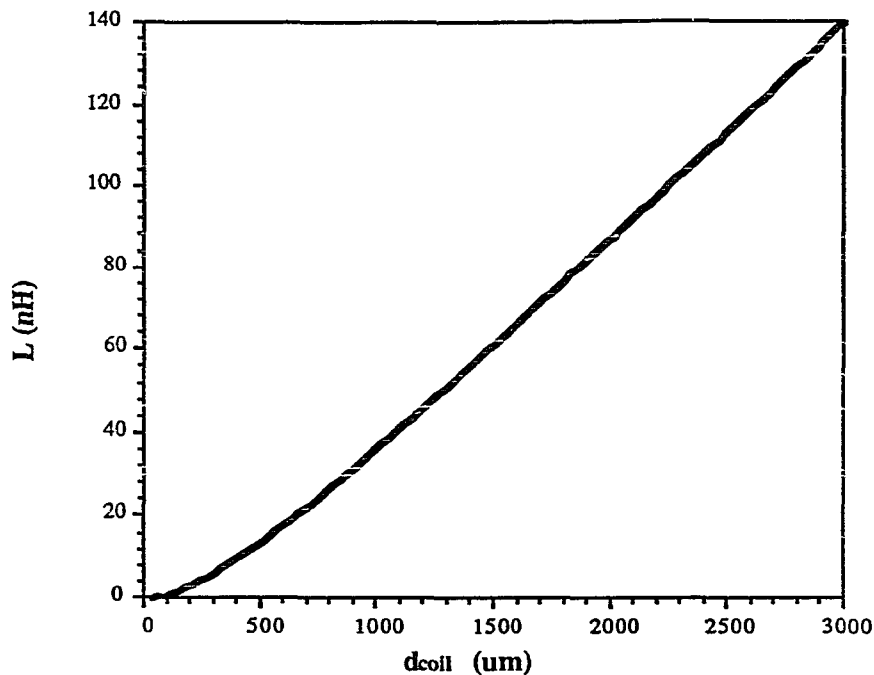


Figure 44 Inductance (L) of a 5-turn solenoidal microcoil.

The computer model was used to predict the theoretical SNR expected for the microcoils. A series of microcoils were constructed for the purpose of SNR testing in  $^1\text{H}$  NMR spectroscopy experiments. The diameters of these microcoils extend from  $38\ \mu\text{m}$  to  $1.8\ \text{mm}$ . The SNR predicted by the computer model is presented in a subsequent section and compared to the results from the NMR experiment. The following section describes the details of the construction of the microcoils.

### 3.3.3 Microcoil fabrication

A series of 5-turn solenoidal microcoils has been constructed, ranging in size from  $1.8\ \text{mm}$  to  $35\ \mu\text{m}$  in diameter. The coils are wound on hollow glass (pulled glass pipet) formers using 42 gauge copper wire, progressing to 50 gauge (1 mil diameter) gold wire and 56 gauge (0.5 mil diameter) gold wire as the coil diameter is decreased as shown in Figure 45.

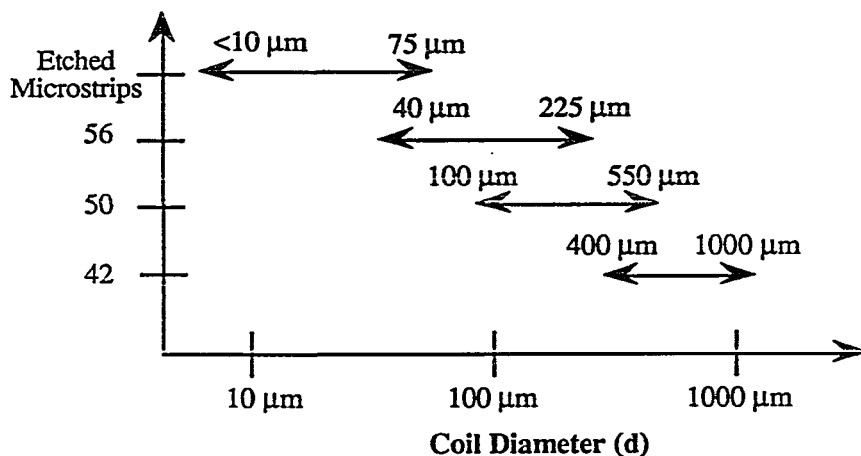


Figure 45 Wire gauge used in winding the microcoils.

The microcoils are wound using special coil positioning equipment and wire manipulation apparatus under a stereo microscope. To begin the winding process, one end of the wire is secured to the glass former using epoxy cement and then weighted to maintain constant tension. A dual set of conductors are simultaneously wound side-by-side onto the former by gently rotating the pin vise. When the appropriate number of turns has been wrapped onto the former, the wire is secured in place by a light coating of either epoxy or Q-dope adhesive. The weights are then disconnected and one of the conductors is carefully removed, leaving only one wire on the former. In such a manner, the inter-turn spacing is maintained at approximately  $r_{sep}/d = 2$ . The microcoil winding process is illustrated in Appendix C, with a completed microcoil illustrated in Figure 46. This particular microcoil is one of the earliest coils constructed, with a diameter of 240 μm and wound using 50 ga gold wire. Green food coloring (predominantly water and propylene glycol) is sealed in the capillary which also serves as the coil former. A droplet of epoxy (not visible in picture) on either side of the sample prevents sample evaporation. Epoxy is also used to seal the wires in place, with some epoxy concentrations visible between turns.

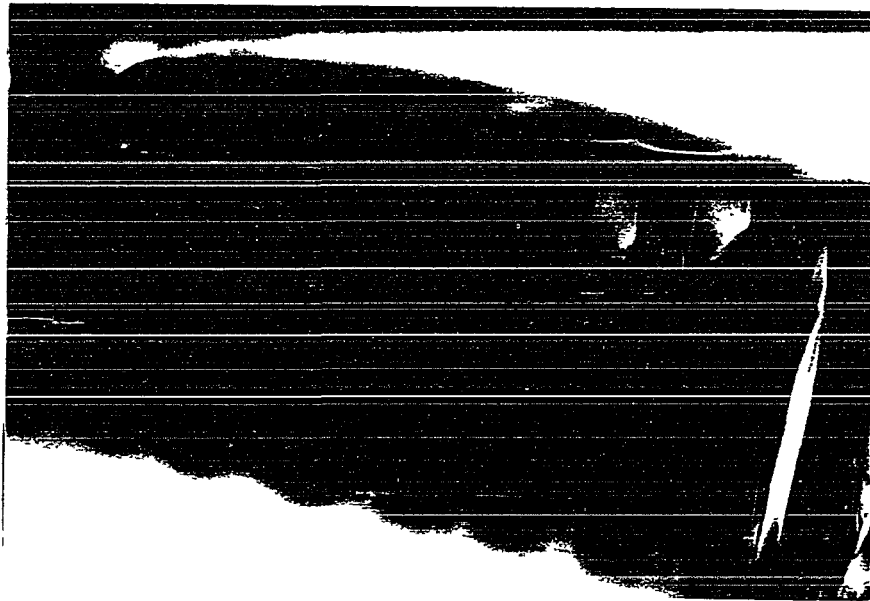


Figure 46 Close-up view of a 240  $\mu\text{m}$  diameter microcoil wound using 56 ga gold wire.

The completed coil is then fixed to a semirigid coaxial cable (UT-85SS).<sup>11</sup> Coaxial mounting is preferred over circuit board mounting for smaller coils because it minimizes the parasitic effects which arise from the mounting assembly. The microcoils are secured by using silver paint or conductive epoxy. We have found both of these electrical connecting processes superior to low-temperature soldering and wire-bonding. In either of the latter processes, the delicate coil wire and the sample are exposed to excessive heat. Conductive paint preserves both the coil and the sample. Several of the completed microcoil assemblies showing both coaxial and circuit-board mounting are shown in Appendix C.

The capacitors which tune and match the coil to the 50  $\Omega$  transmission line should, from an electrical standpoint, be located as close to the coil as possible. The circulating currents which flow in the circuit at resonance can be substantial (much greater than the input current) and can result in large ohmic losses in the component leads. Shorter leads provide a lower loss and higher Q. Additionally,

a standing electromagnetic wave results if the coil ( $Z_c \neq 50 \Omega$ ) is connected remotely to the capacitors with a  $50 \Omega$  transmission line. The points of current maximum in the line can yield substantial ohmic losses due to the high value of local current, even though the loss in the transmission line may be negligible for other applications.

However, the electrical losses in the resonant circuit are not the only consideration. The magnetic susceptibility of the material from which the capacitors are made must be considered in the NMR experiment. A slight variation in the permeability ( $\mu$ ) of the capacitor dielectric from the free-space value ( $\mu_0$ ) can result in a substantial variation in the amplitude of magnetic field ( $B = \mu H$ ). The material chosen as the capacitor dielectric will typically have a large value of permittivity ( $\epsilon$ ) to provide a maximum value of capacitance with a minimum capacitor size as described by

$$C = \frac{\epsilon A}{d_{\text{cap}}} \quad (51)$$

In Eq. (51),  $\epsilon$  is the permittivity of the dielectric,  $A$  is the cross-sectional area of the capacitor plates, and  $d_{\text{cap}}$  is the distance of plate separation. Therefore, a primary consideration in the selection of the dielectric material used in capacitors is the value of  $\epsilon$ , with little or no consideration given to the value of  $\mu$ . Consequently, most capacitor dielectrics have a permeability which is different from that of free-space ( $\mu \neq \mu_0$ ).

A compromise must therefore be made in the electrically optimum circuit by placing the capacitors somewhat remote from the coil and sample so that the local magnetic field homogeneity near the sample is preserved. It was determined that the optimum geometry is that shown in Figure 47, pictured with a  $50 \mu\text{m}$  diameter microcoil made of 56 ga gold wire.



Figure 47 A 50  $\mu\text{m}$  diameter microcoil, connected to an 8 cm UT-85SS<sup>11</sup> semirigid coaxial cable.

An enlarged view of the coil is provided in Figure 48, and shows that good winding uniformity is maintained for coils with diameters as small as 50  $\mu\text{m}$ . The coil is remotely located from the tuning and matching capacitors by a 8 cm section of semirigid coaxial cable (UT-85SS),<sup>11</sup> seen to the right of the coil in Figure 47, and secured with silver paint. Additionally, the tuning and matching capacitors are made of special dielectric materials to provide minimum susceptibility. The effects of the various mounting geometries and their influence on the local susceptibility variation near the sample are demonstrated with NMR results in a subsequent section. As the diameter of the solenoidal coils is reduced below 25  $\mu\text{m}$ , the conductor widths, thicknesses, the capillary diameter used to mount the coil, and the distance between opposite ends of the coil are reduced. Fabrication of coils with diameters less than 25  $\mu\text{m}$  requires microelectronic fabrication. Such coils are not included in this thesis but will be pursued as a continuation of this research.<sup>12</sup>

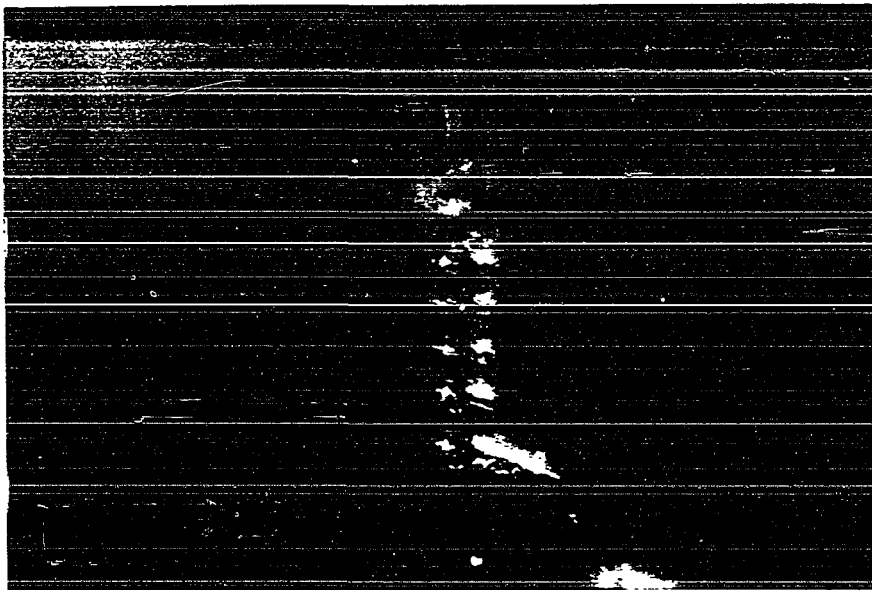


Figure 48 Enlarged view of the 50  $\mu\text{m}$  diameter microcoil shown in Figure 47.

### 3.3.4 Electrical testing

The analysis of microcoils involves the theoretical modeling and testing of the coil's electrical properties (R, L, Q, self-resonant frequency). Experimental data from electrical testing of the microcoils are provided in Appendix D and described in this section. The theory outlined in Chapter 2 was verified using 16 ga wires and larger coils, and is described in an earlier section. A verification of the theory ( $0.1 \leq z \leq 20$ ) using microcoils would require frequencies in excess of 1 GHz and was not performed.

The low-frequency electrical characteristics ( $L$ ,  $R_{dc}$ ) of the coils were tested using a 200 MHz network analyzer (HP3577A) with an S-parameter test set (HP35677A) and an RF vector impedance meter (HP4193A). Typical inductance values for coils with diameters of several hundred microns are on the order of 10 nH with dc resistances of approximately 0.3  $\Omega$ . The theoretical resistance of the microcoils is represented by Eq. (44) (microscopic regime) and Eq. (43) (macroscopic regime). The theoretical inductance of the microcoils is represented by<sup>13</sup>

$$L = \frac{n^2 d_{coil}^2}{46d_{coil} + 100h} \quad (52)$$

where both  $d_{coil}$  and  $h$  are in centimeters and  $L$  is in nH. The measured inductance values closely compare with the theoretical predictions, shown for a series of microcoils in Figure 49.

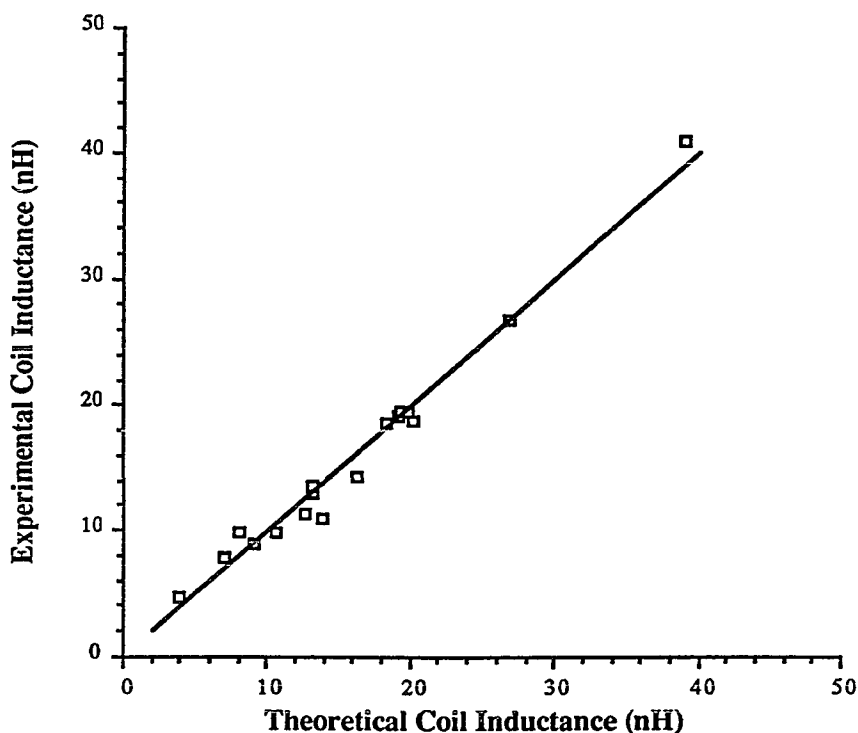


Figure 49 Inductance of microcoils – experiment vs. theory.

Smith chart mapping provides a graphical measurement of the coil impedance and reflection coefficient as a function of frequency. A Smith chart plot showing the input reflection coefficient ( $S_{11}$ ) for a perfect coil is shown in Figure 50. The impedance of the coil at 0 Hz is  $0 \Omega$ , represented by the leftmost point on the curve. As the frequency increases, the  $S_{11}$  plot follows the outer perimeter of the Smith chart, corresponding to a purely inductive reactance ( $0 \Omega$  resistive). As the frequency continues to increase the coil remains inductive until the self-resonant frequency  $f = f_{\text{self}}$ , above which the coil is capacitive. (Self-resonance is described below.) A Smith chart plot of  $S_{11}$  obtained from a  $325 \mu\text{m}$  diameter microcoil made from 50 ga gold wire is shown in Figure 51.

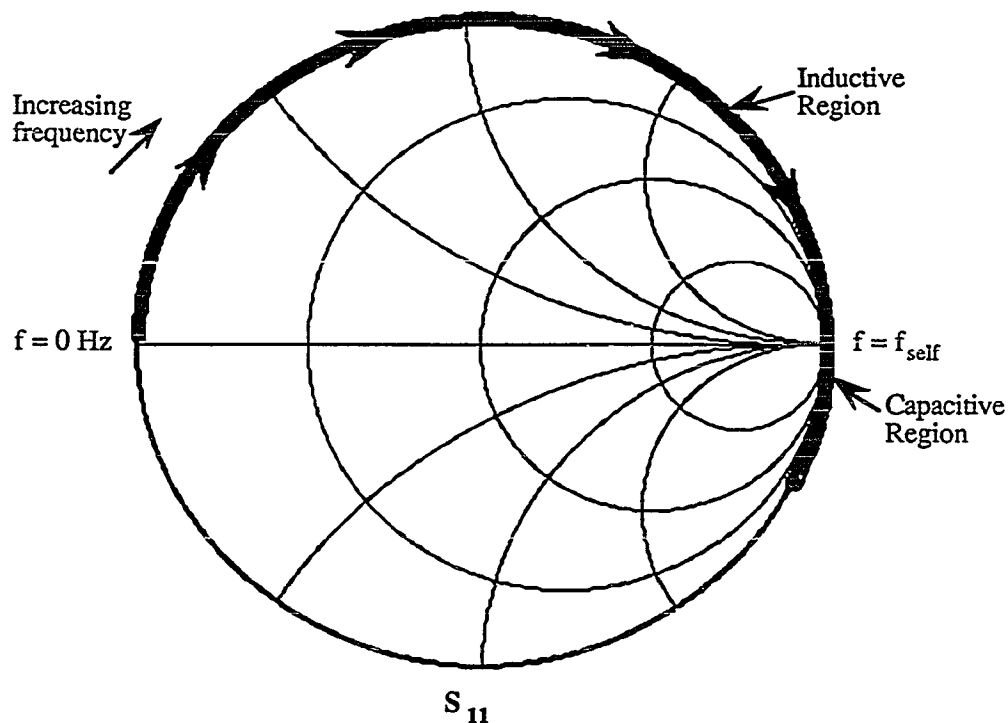


Figure 50 Input reflection coefficient ( $S_{11}$ ) for a perfect coil.

FULL SCALE 1.0000  
 PHASE REF 0.0deg  
 REF POSN 0.0deg

MARKER 200 000 000.000Hz  
 Z MAG (UDF) 193.98E-3  
 Z PHS (UDF) 87.283deg

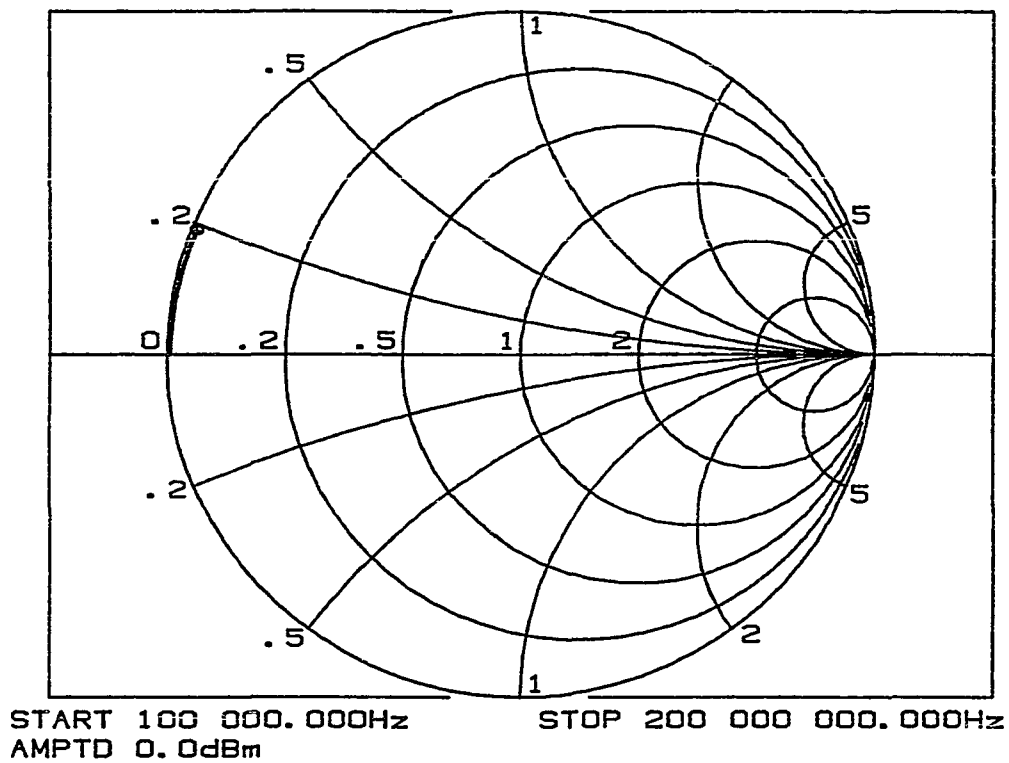


Figure 51  $S_{11}$  for a 325  $\mu\text{m}$  diameter microcoil wound using 50 ga gold wire.

The microcoil self-resonant frequency for coils with diameters greater than 100  $\mu\text{m}$  is determined using a 6 GHz network analyzer (HP8753) and S-parameter test set (HP85047). The concept of self-resonance is illustrated in Figure 52.

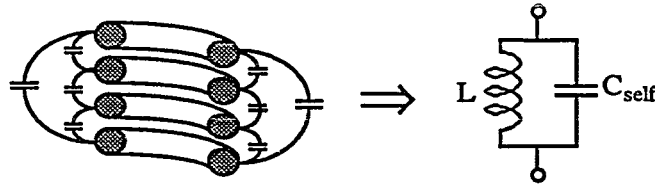


Figure 52 The value of the inter-turn capacitance of a coil and the coil inductance determine the frequency at which the coil will be self-resonant.

There is an inter-turn capacitance which results from the separation of charge between the turns of the solenoid, given by

$$C_{\text{self}} \cong \frac{\epsilon A}{r_{\text{charge}}}$$

where  $\epsilon$  is the permittivity constant of the dielectric (e.g., air or epoxy) between the turns,  $A$  is the effective area of the charge region, and  $r_{\text{charge}}$  is the charge separation. The inter-turn capacitance provides a path for the RF current to flow exterior to the coil winding. This infers that some of the current delivered to the "coil" will actually not pass through the coil and will not contribute to  $B_1$ . Similarly, reciprocity dictates that  $C_{\text{self}}$  will "load" the coil and will reduce the signal received at the preamplifier. At the self-resonant frequency, given by

$$f_{\text{self}} = \frac{1}{2\pi\sqrt{LC_{\text{self}}}}$$

the inductive reactance of the coil cancels the capacitive reactance from  $C_{\text{self}}$ , resulting in a parallel resonant *tank* circuit.

A properly designed coil will have a self-resonant frequency that is well above its intended frequency of operation. At frequencies well below  $f_{\text{self}}$ , the effect of  $C_{\text{self}}$  is negligible. However, at frequencies nearer to  $f_{\text{self}}$ , the losses inherent to the coil are enhanced. Furthermore, the rapid

variation in the net inductance of the tank circuit at frequencies near  $f_{\text{self}}$  results in unstable coil performance and circuit operation. Therefore, operating the coil well below  $f_{\text{self}}$  results in a lower coil noise, higher SNR, and better circuit stability. Typical values for the self-resonant frequencies for microcoils are in the GHz range, well above the intended resonant frequency of 200 MHz. Accordingly, microcoils would be capable of stable operation in extremely high field (greater than 10 T) magnet systems. Smaller microcoils ( $d_{\text{coil}} < 100 \mu\text{m}$ ) have self-resonant frequencies above 6 GHz. For these, a higher frequency network analyzer (e.g., the HP8510) would be required to determine the self-resonant frequency. A Smith chart plot of  $S_{11}$  for a microcoil of  $800 \mu\text{m}$  diameter and a self-resonant frequency of approximately 3.74 GHz is shown in Figure 53.

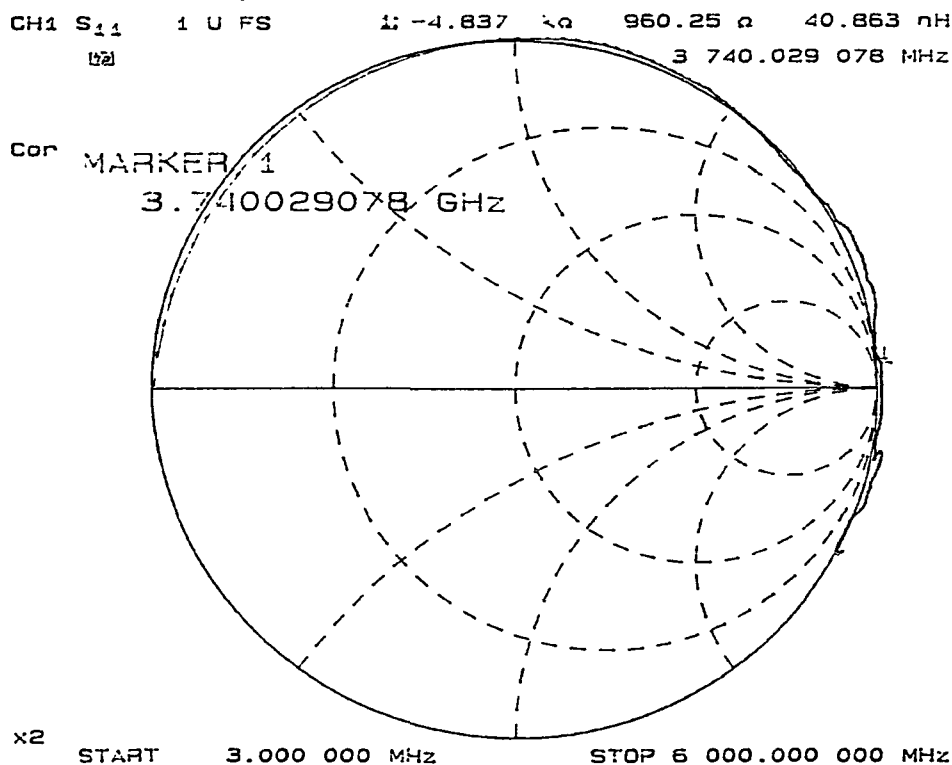


Figure 53 The self-resonant frequency of an  $800 \mu\text{m}$  diameter microcoil is measured using the network analyzer to be 3.74 GHz.

It would seem that the relatively small value of inter-turn separation would yield a large value of  $C_{\text{self}}$  and low self-resonant frequency. However, it is the effective current path that must be considered when determining  $r_{\text{charge}}$ .<sup>10</sup> The current in the wire of the solenoid is unevenly distributed in accordance with the flux linkage between turns as shown in Figures 27 and 28. Therefore, as shown in Figure 54, the value of  $r_{\text{charge}}$  can be substantially greater than  $r_{\text{sep}}$ , resulting in a smaller value of self-capacitance.

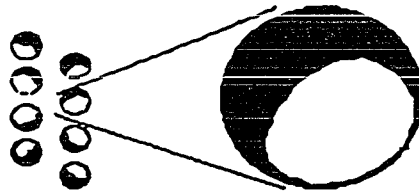


Figure 54 The effect of current crowding causes the actual value of inter-turn capacitance of a solenoidal coil to be less than that which would result from a uniform current distribution.

The microcoils are resonated at 200 MHz (4.7 T) using standard nonmagnetic chip capacitors in a parallel resonant tank circuit. For a fixed number of turns, microcoil inductance decreases with coil diameter as shown in Figure 49, and can be as low as several nH for a microcoil with  $d_{\text{coil}} \cong 100 \mu\text{m}$ . The value of capacitance required for resonance varies inversely with inductance as given by

$$f_o = \frac{1}{2\pi\sqrt{LC_{\text{tune}}}} \quad (53)$$

and can be unreasonably large for smaller diameter microcoils. As seen by this relationship, the use of higher magnetic field strengths and higher resonant frequencies permits the use of a smaller, more

physically compact resonating capacitance. Therefore, in addition to providing a higher signal-to-noise ratio, operating at higher resonant frequencies will minimize parasitic lead effects.

The resonant tank circuit, comprised of the microcoil and a parallel resonating capacitance ( $C_{\text{tune}}$ ), must be matched to a  $50 \Omega$  impedance to provide an efficient energy transfer between the microcoil and the transmitter/receiver circuitry. There are a wide range of options available to the circuit designer when constructing an impedance transformation circuit. Often, reactive components (i.e., inductors and capacitors) are used in the matching circuit. Such components provide the necessary phase shift of the voltage and current electromagnetic waves to accomplish impedance transformation, while (ideally) contributing no additional resistance (loss) to the circuit. In general, there is a tradeoff between the number of components required. A greater number of components will provide a more smooth transition between the two impedances. Such a circuit would be capable of operation over a specified bandwidth and with a specified  $Q$ . The use of a smaller number of components in the impedance transformation circuit implies that a smaller number of circuit parameters can be simultaneously controlled. The simplest impedance matching circuits are limited to operation at a single frequency. In this study, impedance transformation is accomplished using a single capacitor ( $C_{\text{match}}$ ) in series with the tank circuit as shown in Figure 55, and provides a  $50 \Omega$  impedance at  $\omega_0 = 200 \text{ MHz}$ .

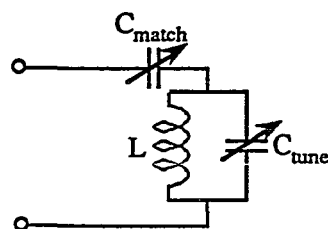


Figure 55 Impedance transformation to  $50 \Omega$  using a series matching capacitor ( $C_{\text{match}}$ ).

The processes of tuning and matching using the Smith chart and a network analyzer are shown in Figure 56.

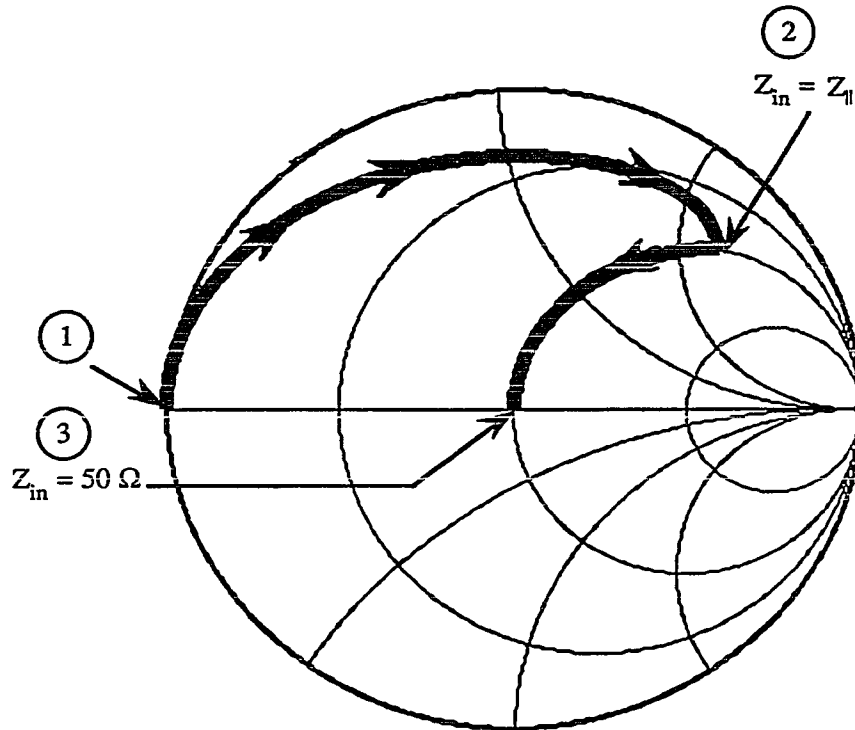


Figure 56 Tuning and matching using the Smith chart.

As the frequency increases from zero (point 1), the parallel combination of  $C_{\text{tune}}$  and  $L$  approaches a resonant condition. The objective is to adjust  $C_{\text{tune}}$  so that the input reflection coefficient curve passes through the  $50 \Omega$  circle on the Smith chart at  $\omega = \omega_0$  (point 2). The net impedance ( $Z_{||}$ ) looking into the parallel combination at point 2 is of the form  $Z_{||} = 50 \Omega + j\omega_0 L_{\text{eff}}$  where  $L_{\text{eff}}$  is the *effective* inductance of the network. The matching capacitor is intended to add a negative reactance given by  $1/\omega_0 C_{\text{match}} = -\omega_0 L_{\text{eff}}$ . The resulting input impedance of the tank circuit at frequency  $\omega_0$  is  $Z_{\text{in}} = R_{\text{in}} = 50 \Omega$  (point 3).

The resonant frequency and circuit  $Q$  for a variety of microcoils were measured using a network analyzer. The  $Q$  of an ideal parallel tank circuit is given by

$$Q_{\text{circuit}} = \frac{\omega_0}{\omega_2 - \omega_1} \quad (54)$$

where  $\omega_2$  and  $\omega_1$  are the 3 dB points of the resonant characteristic curve, that is, the frequencies at which the transfer function of the circuit is reduced in magnitude by 3 dB. The circuit Q can be determined from the Smith chart as shown in Figure 57.

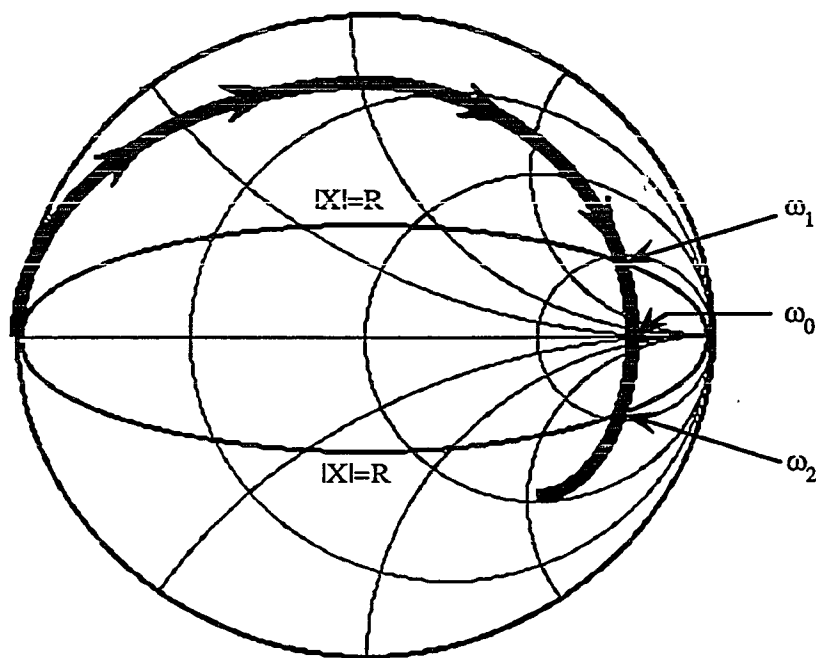
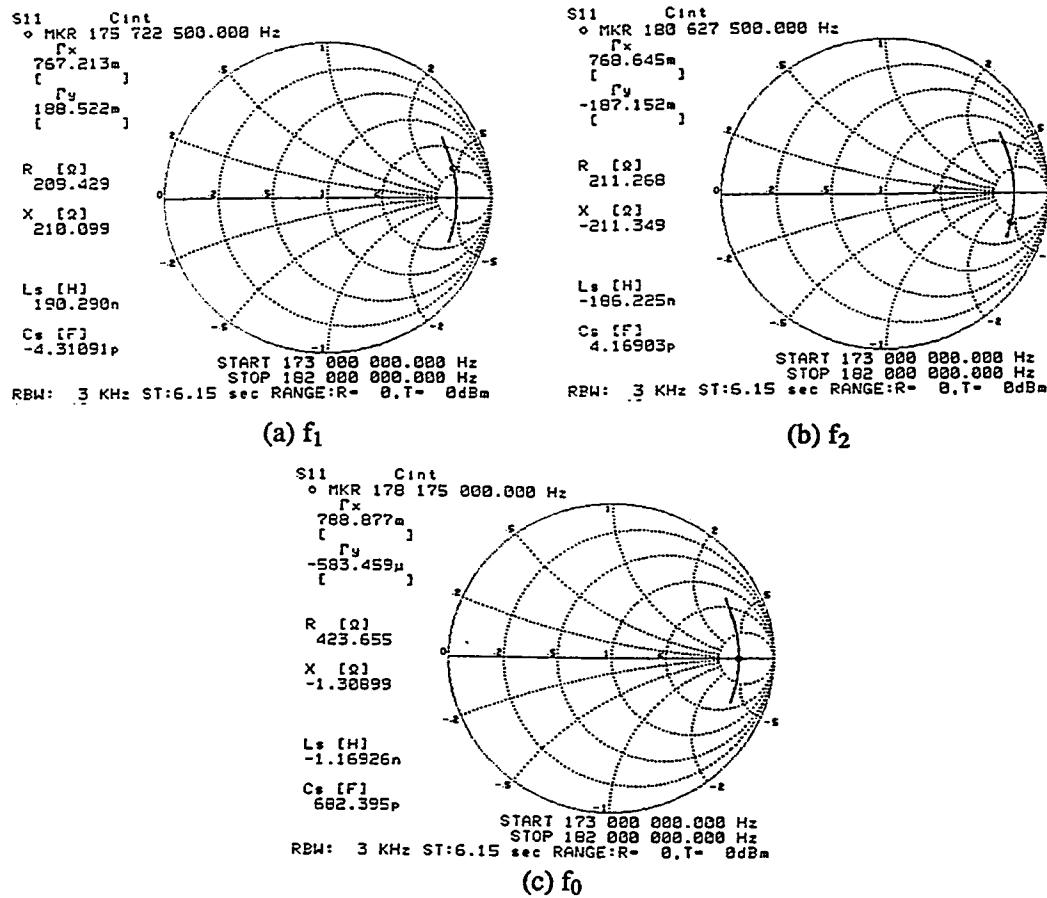


Figure 57 The circuit Q is defined (for an ideal parallel or series RLC resonant tank circuit) by Eq. (54) and can be determined using the Smith chart.

The overall circuit Q is related to the Q of the circuit components by  $(1/Q_{\text{circuit}}) = (1/Q_c) + (1/Q_{\text{cap}})$ . Both the formula for  $Q_{\text{circuit}}$  and the formulae for the component Q's ( $Q_c = \omega L/R_c$  and  $Q_{\text{cap}} = 1/\omega R_{\text{cap}}C$  where  $R_{\text{cap}}$  is the resistance associated with the capacitor and its leads) require that  $Q \gg 1$  to be valid. Typical microcoil  $Q_c$  values are 30-70, well below the capacitor Q ( $Q_{\text{cap}} = 1000$  or more). Therefore,  $Q_c$  can be determined by measuring  $Q_{\text{circuit}}$  of the resonant network. As shown in Figure 58, a circuit Q of 36.3 was measured for a 643  $\mu\text{m}$  diameter microcoil built for use at 4.7 T ( $f_0 = 200$  MHz), in good agreement with the theoretical prediction of 33.5. Assuming that the inductance of the coil is accurately characterized by Eq. (52) and that additional losses from the

electrical connection and the mounting assembly are minimal, the determination of  $Q_c$  provides a measure of the high-frequency loss in the microcoil ( $R_c = \omega L/Q_c$ ).



$$Q = \frac{f_0}{f_2 - f_1} = \frac{178.175 \text{ MHz}}{180.6275 \text{ MHz} - 175.7225 \text{ MHz}} = 36.325$$

Figure 58 The  $Q$  of a 643  $\mu\text{m}$  diameter microcoil, measured using  $S_{11}$  using the Smith chart.

There is an additional advantage provided by using the technique of measuring  $Q_{ckt}$  to determine  $R_c$ . The resistive impedance of microcoils is low, typically less than 1  $\Omega$ . The reactive

impedance, however, can be considerably higher (typically by two orders of magnitude). An accurate calculation of the resistive impedance component of a predominantly reactive device (e.g., a coil) is difficult. This is primarily due to the inherent inaccuracy which results when trying to measure a vector component whose magnitude is much less than the net vector magnitude. At resonance, however, the reactive component of the coil impedance cancels with the reactive component of the capacitor impedance, and the resistive component of the coil (and capacitor) impedance is transformed to a higher value. Consequently, the coil resistance can be more accurately determined using the Q measurement technique.

A higher value of resistance at resonance does not necessarily imply that a deteriorated SNR will be achieved with resonant coils. The resistance, and hence the noise, is transformed at resonance, but so also is the signal. However, for the purpose of determining the coil resistance, the higher value of coil resistance near resonance is more easily measured and with greater accuracy than is possible off-resonance. It should be noted, however, that the capacitor leads and connecting wires will contribute additional loss at resonance, as circulating currents will flow in the tank circuit, including both the coil and the resonating capacitor. Hence, an accurate measurement of coil loss using the Q technique requires that the capacitor leads be short (i.e., the capacitor Q be much higher than the coil Q) and that the electrical connections between the coil and the capacitor be as short as possible.

A subset consisting of eight of the microcoils used in this study was chosen for empirical determination of microcoil loss using the HP4195A network analyzer and the Q measurement technique. The Smith chart plots of  $S_{11}$  for the microcoils, showing the measurement of L and Q, are provided in Appendix D. The results are shown in Figure 59, where the empirically measured microcoil resistance (determined using the HP4195A and the Q measurement technique at 200 MHz) is compared to the theoretical resistance (calculated using the computer model which has been described in a previous section). The coil diameter and the wire gauge used in wrapping the coil are shown in Figure 59 for each of the data points. The maximum discrepancy in the error between theoretical predictions and experimental data is 32%. However, the error is evenly distributed, with

an average error of less than 1% but with a standard deviation of 20%. As shown in Appendix D, the most-significant error occurred for the coil of smallest resistance ( $0.2215 \Omega$ , theoretical).

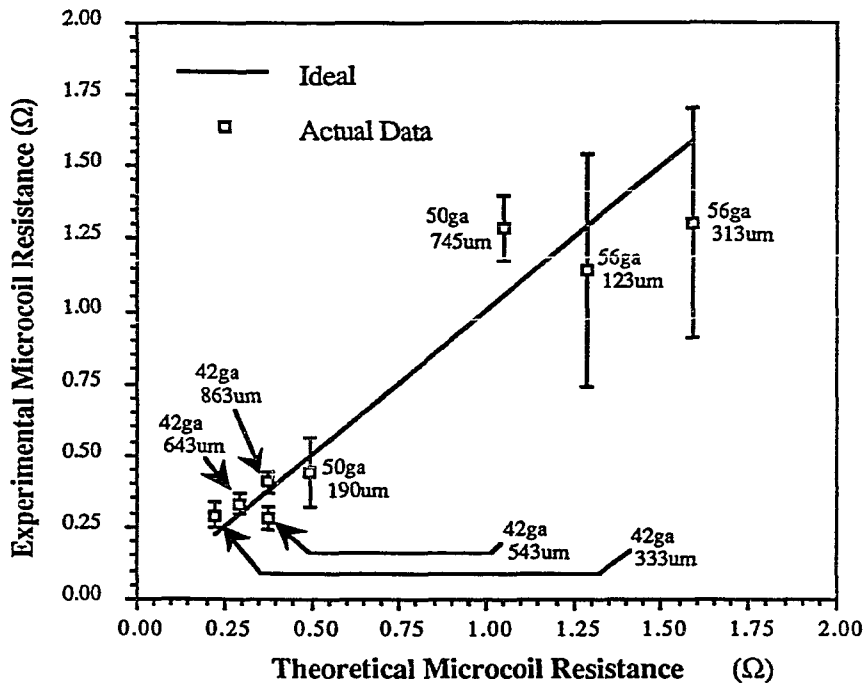


Figure 59 Resistance of microcoils – experiment vs. theory.

There are several factors which could be responsible for the error in Figure 59. First, the parasitic loss (e.g., from the electrical connection) would most significantly affect coils with smaller resistance. Second, as explained in Section 3.3.2, the piecewise approximation used for the computer model could yield 15% error in the theoretical estimation of resistance. The lead lengths of the coil (when connected to the resonating capacitor) were measured with a scale under the microscope and were taken into account in the theoretical calculation of  $R_c$ . The error bars in Figure 59 correspond to a 1 mm error in the measurement of the total lead length of the coil. Inaccuracy in the measurement of the lead lengths is a third source of error. A fourth source of error is microscopic imperfections in the delicate microcoil assemblies. It is shown in Section 3.3.5 that similar errors occurred when using

microcoils in NMR experiments. Therefore, a further discussion of the error is postponed until the end of this section.

### 3.3.5 Verification using NMR

The microcoils were tested for their signal-to-noise performance in a  $^1\text{H}$  NMR experiment at 4.7 T ( $f_0 = 200$  MHz). NMR testing and evaluation were performed using a SISCO SIS/200 33 cm bore 4.7 T superconducting magnetic resonance spectrometer/imaging system. The sample consisted of water doped with 5 mM  $\text{CuSO}_4$  ( $T_1 \cong 100$   $\mu\text{sec}$ ) and was loaded into the capillary. The coils were used both to transmit and to receive. NMR testing consisted of spectroscopic data collection only, as the magnitude of the received signal and noise is sufficient to determine the SNR.

At the beginning of an NMR experiment, a pulse calibration must be performed to determine the energy that is required to achieve a tip angle of  $\alpha = \pi/2$ . A typical pulse calibration profile is shown in Figure 60.

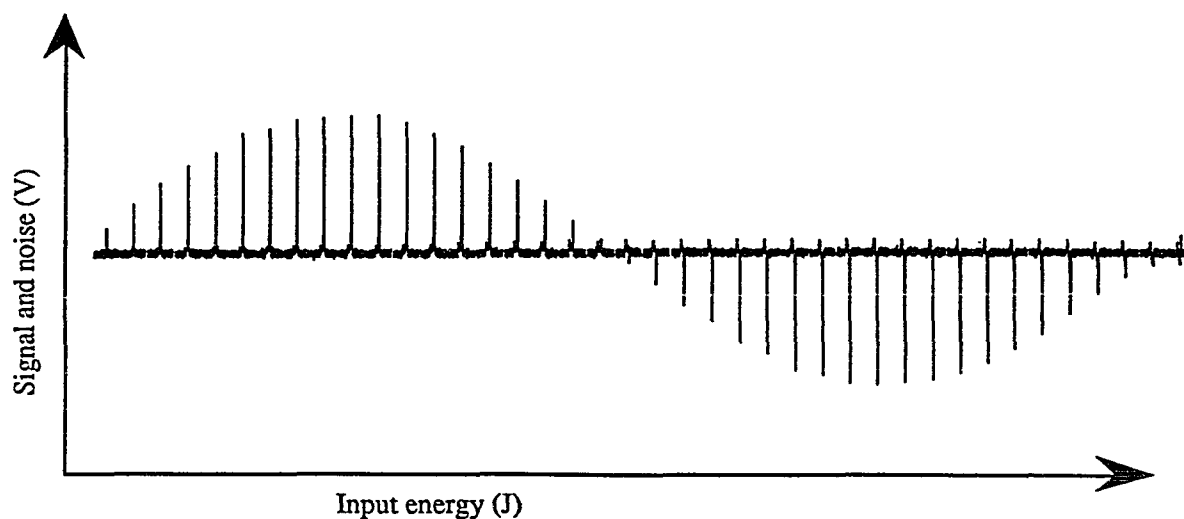


Figure 60 A typical pulse calibration profile, obtained from a 190  $\mu\text{m}$  diameter microcoil.

The vertical axis of a single spectrum represents the magnitude of the received signal and noise and the horizontal axis represents the receiver frequency bandwidth ( $\Delta f$ ). The entire pulse calibration profile is a collection of many individual spectra, with each successive spectrum corresponding to a higher input energy level. The profile in Figure 60 was obtained from a microcoil with 190  $\mu\text{m}$  diameter. As explained in Chapter 2 and shown in Figure 5, the magnitude of the received signal is greatest when the individual magnetic moment vectors are phase coherent and when the bulk magnetization vector  $m_s$  is tipped by an angle of  $\alpha = \pi/2$ . Hence, in Figure 60, the vertical axis represents the magnitude of the received signal and noise and the horizontal axis represents the energy delivered to the coil. As the RF energy supplied to the coil and sample is increased,  $\alpha$  continues to increase, with a maximum signal reception occurring when  $\alpha = p\pi/2$  where  $p$  is an odd integer. As shown in Figure 60, a signal is not received when  $\alpha$  is a multiple of  $\pi$ .

The cyclic nature of the pulse profile should continue indefinitely. In practice, however, the overall magnitude of the spectroscopic signal decreases at higher values of  $p$  where  $0 \leq p\alpha \leq 2\pi$  and  $p$  is an integer. This is due to the fact that the inherent  $B_1$  inhomogeneity in a real coil will be enlarged by a factor of  $p$ , and will result in a reduced sensitive volume for the coil and a lower received signal strength. Therefore, the decaying signal strength for repetitive cycles of the pulse profile is representative of the  $B_1$  homogeneity of the RF coil. The coils most commonly used for NMR (saddle coils or birdcage coils) suffer from  $B_1$  inhomogeneity and low sensitivity. Consequently, the signal strength is rapidly attenuated, and the pulse profile is rarely extended past the first cycle. Solenoidal coils, however, have the best sensitivity and  $B_1$  homogeneity of the common coil geometries. This should be reflected in the pulse profile obtained using microcoils. Figure 61 is a pulse profile obtained using a 570  $\mu\text{m}$  microcoil, extended to 4.5 cycles.

The SNR is measured by comparing the relative magnitude of the signal and noise received following  $\pi/2$  excitation for the series of microcoils. It was explained in Chapter 2 that the measurement of the NMR signal (FID) must take place immediately following the  $\pi/2$  pulse. The FID is digitally sampled using an analog-to-digital converter (ADC), with the sampled data points (SDF) stored in a computer for postprocessing following data collection. It can be assumed that no relaxation

of the sample magnetization occurs during excitation. Similarly, the first SDP of the FID can be assumed to be representative of the true signal magnitude, with minimal relaxation effects. However, there is a time required, following excitation, for the excitation currents in the resonant circuit and the mechanical vibrations of the coil to cease. This is commonly referred to as the *ringdown time* of the coil. The first several SDP of the FID are spoiled during ringdown. Consequently, some relaxation of the sample magnetization does occur before any useful SDP can be acquired. Relaxation results in a signal spectrum that is broadened in accordance with  $T_2^*$ , which includes the effects of  $T_2$  relaxation, dephasing of the signal from spin-spin coupling, and local inhomogeneities in the magnetic field. Accordingly, the height of the spectral signal is reduced as the baseline is broadened. In the absence of other relaxation effects, the signal magnitude to use in the calculation of the SNR could be obtained by multiplying the height of the spectral signal by its width.

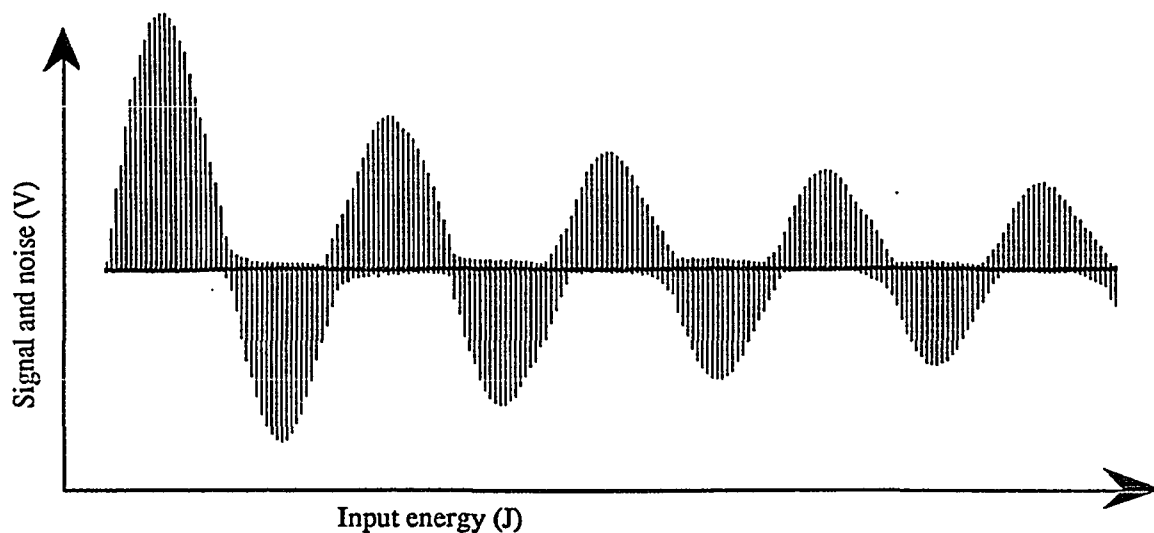


Figure 61 A typical pulse calibration profile, obtained from a 570  $\mu\text{m}$  diameter microcoil, extended to 4.5 cycles.

However, susceptibility variations that arise from the the mounting assembly and from the coil itself lead to further relaxation effects and further broaden the FID. It is difficult to maintain consistency when mounting the microcoils. The leads of microcoils wound with 42 ga copper wire are sufficiently rigid to support the weight of the microcoil. Such is not the case for microcoils wound with the smaller gold wire. These microcoils are suspended by supports placed at the ends of the capillary former. The inconsistency in the mounting geometries and the variations in the coil materials (copper and gold) result in a susceptibility broadening that is not uniform for all coils.

The geometry of the mounting assembly had a significant effect on the linewidth of the signal. The following figures represent the lineshape of the spectroscopic signal obtained from a  $^1\text{H}$  NMR spectroscopy experiment using 500  $\mu\text{m}$  diameter microcoils with various mounting geometries. Each of the coils contained 5 mM  $\text{CuSO}_4$  ( $T_1 \cong 100 \mu\text{sec}$ ). For the larger coils ( $d_{\text{coil}} > 200 \mu\text{m}$ ), a single (nonselective) excitation pulse was used to excite the sample. However, for the smaller coils, signal averaging was employed to provide a better overall SNR, with as many as 2048 acquisitions. In Figure 62, the tune and match capacitors are placed adjacent to the coil, with minimal coil lead length. Furthermore, the capacitors that were used are not specifically intended for magnetic applications. The spectral signal is significantly broadened, with a linewidth in excess of 1 kHz. In Figure 63, special, nonmagnetic capacitors were used, and the capacitors were removed from the coil by an 8 cm section of UT-85SS<sup>11</sup> coaxial transmission line. The line broadening that is present in Figure 62 is severely reduced in Figure 63, with a linewidth less than 100 Hz. In Figure 64, the coil leads are lengthened, removing the coil from the transmission line and minimizing susceptibility effects due to the transmission line. The signal linewidth is shown to be less than 10 Hz. However, some broadening remains at the base of the signal, due to susceptibility variations near the coil (e.g., the coil itself, the coil former, and air bubbles within the sample).

The value used for the (peak) signal in the calculation of the SNR is obtained by integrating the spectroscopic signal over the frequency band. This method provides a uniform measure of the signal, regardless of the line broadening which has occurred. The value of the integral represents the height of the delta function which would have resulted from the first SDP in the absence of relaxation.

## SUSCEPTIBILITY EFFECTS

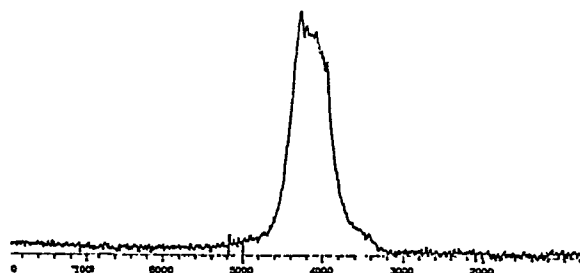
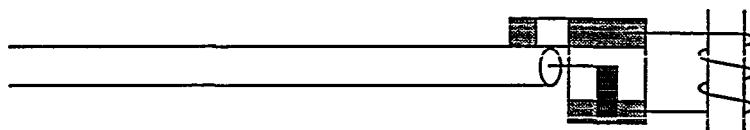


Figure 62 The signal spectrum acquired using 5mM  $\text{CuSO}_4$  in a  $^1\text{H}$  NMR spectroscopy experiment, using a 500  $\mu\text{m}$  diameter microcoil wound using 42 ga copper wire. The coil was placed in the immediate vicinity of the tuning capacitors (*not* nonmagnetic) and the transmission line. Significant line broadening resulted.

## SUSCEPTIBILITY EFFECTS

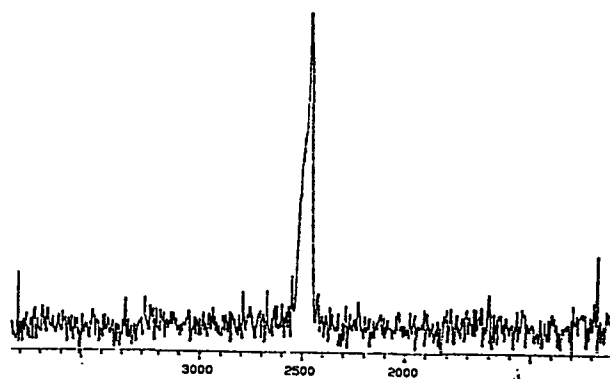
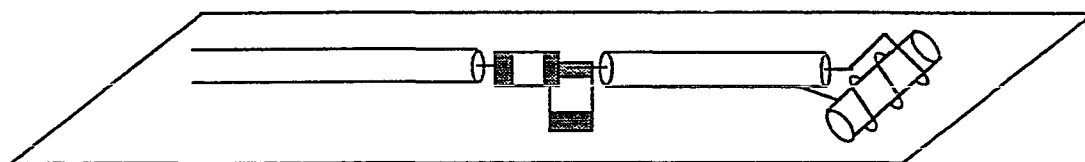


Figure 63 The signal spectrum acquired using 5mM  $\text{CuSO}_4$  in a  $^1\text{H}$  NMR spectroscopy experiment, using a 500  $\mu\text{m}$  diameter microcoil wound using 42 ga copper wire. The coil was separated from the tuning capacitors (nonmagnetic), but remained in the near vicinity of the transmission line. The line broadening is not as severe as that of Figure 62.

## SUSCEPTIBILITY EFFECTS

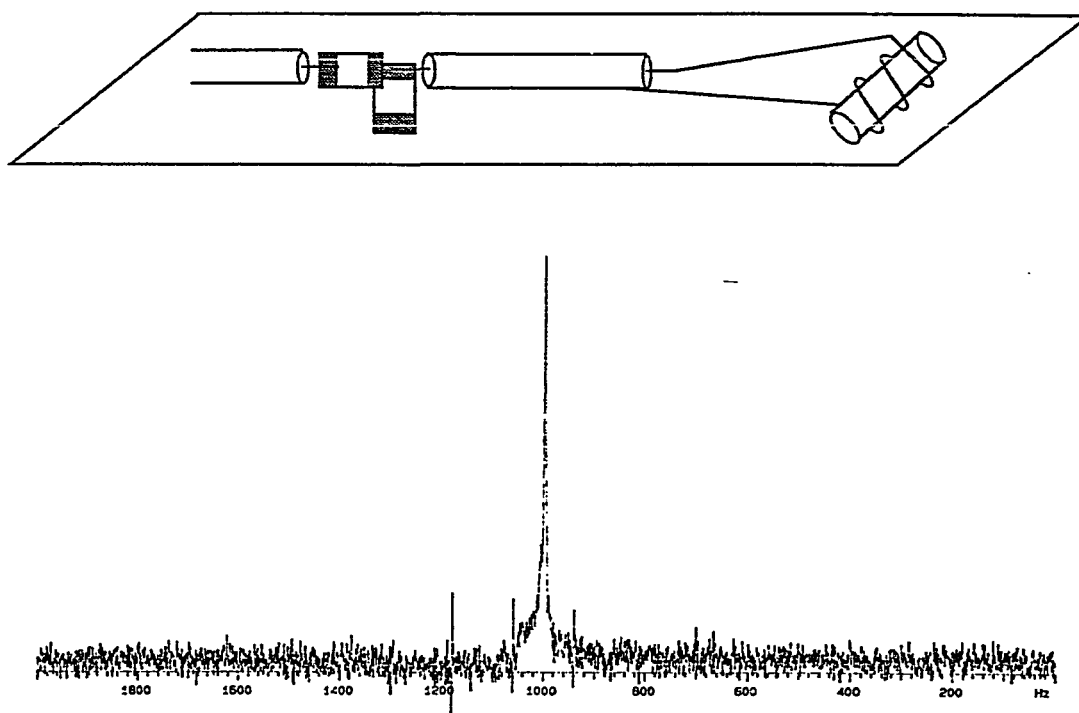


Figure 64 The signal spectrum acquired using 5mM  $\text{CuSO}_4$  in a  $^1\text{H}$  NMR spectroscopy experiment, using a 500  $\mu\text{m}$  diameter microcoil wound using 42 ga copper wire. The coil was removed from both the tuning capacitors (nonmagnetic) and the transmission line. This provided the optimal geometry for minimum susceptibility effects.

The value of the noise used in the calculation of the SNR is determined by simple measurement of the peak noise in the FID spectrum. The ratio of the signal to the noise provides the empirical SNR to compare with the theoretical results from the computer program. The theoretical and experimental  $SNR_{puv}$  obtained for the microcoils are plotted in Figure 65 against the coil diameter.

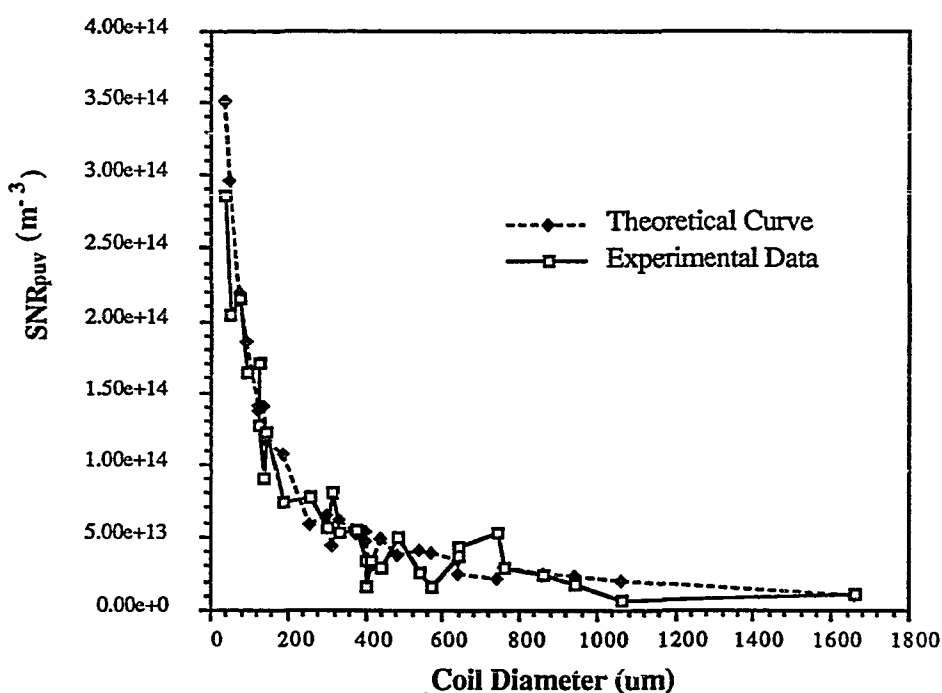


Figure 65  $SNR_{puv}$  vs.  $d_{coil}$ .

For the smaller microcoils, in which signal averaging was employed to provide a better overall SNR, the measured SNR was reduced by  $N^{1/2}$ , where  $N$  is the number of acquisitions. Additionally, the specific lead length and volume of each microcoil assembly are considered in the theoretical calculation of the  $SNR_{puv}$ , and the experimental data have been scaled by

$$SNR_{puv} \Big|_{coil} = SNR \Big|_{measured} \frac{\sqrt{\frac{R_c + R_{lead}}{R_c}}}{v_s} \quad (55)$$

where  $R_c$  is the resistance of the coil,  $R_{lead}$  is the resistance of the coil leads, as given by the computer program, and  $v_s$  is the sample volume. In this manner, a relative comparison can be made between the theoretical and experimental  $SNR_{puv}$  for the microcoils. Furthermore, an adjustment has been made to account for the noise factor of the preamplifier. The noise factor is defined by

$$NF = \frac{SNR_{in}}{SNR_{out}}$$

Often, the noise factor is specified in dB as  $NF_{dB} = 10 \log_{10} NF$ . An ideal preamplifier will have a  $NF = 1$  ( $NF_{dB} = 0$ ). However, real preamplifiers will have noise figures greater than this, with the rule-of-thumb being that a "good" preamplifier have a  $NF_{dB} \leq 1$  dB. The preamplifier used in this thesis was measured as  $NF_{dB} = 1.89$  dB. The eight microcoils which were chosen to be representative of the complete series of microcoils and to be used in the electrical verification of coil resistance (Section 3.3.4) are indicated in Figure 66. Additionally, the  $SNR_{puv}$  plot of Figure 65 is displayed in logarithmic form in Figure 67, where an inverse variation with  $d_{coil}$  should appear as a straight line with a slope of -1.

The average error in the  $SNR_{puv}$ , as shown in Figures 65-67, is roughly 1%. However, the standard deviation of the error is high, approximately 48%. This fluctuation in error is analogous to that observed in Figure 59 of the previous section. There are several sources from which error could arise. The theoretical calculation of coil loss was made using the "piecewise" approximation, represented by Figure 42, and could account for as much as 15% error in coils wound with 56 ga gold wire. Furthermore, the resistance of the leads of the microcoils was substantial, and for the smaller coils the lead resistance was several times greater than the coil resistance. The resistance of the coil leads was determined by measuring the lead lengths under the microscope and by using the straight-wire loss model. The error involved in the measurement of the lead lengths (and in the  $SNR_{puv}$ ) would be higher for the smaller coils as shown in Eq. (55) and in Figure 68, where error bars are included to represent an error of +/- 1 mm in the measurement of lead length.

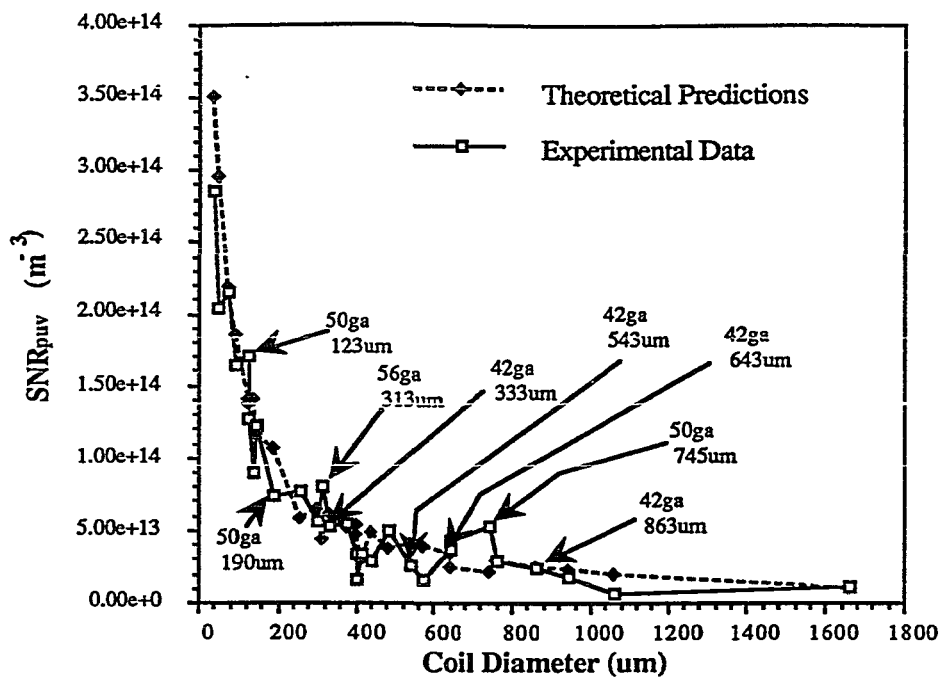


Figure 66 The  $SNR_{puv}$ , obtained using the microcoils in NMR experiments, with the 8 microcoils chosen for resistance testing in Section 3.3.4 indicated by the arrows.

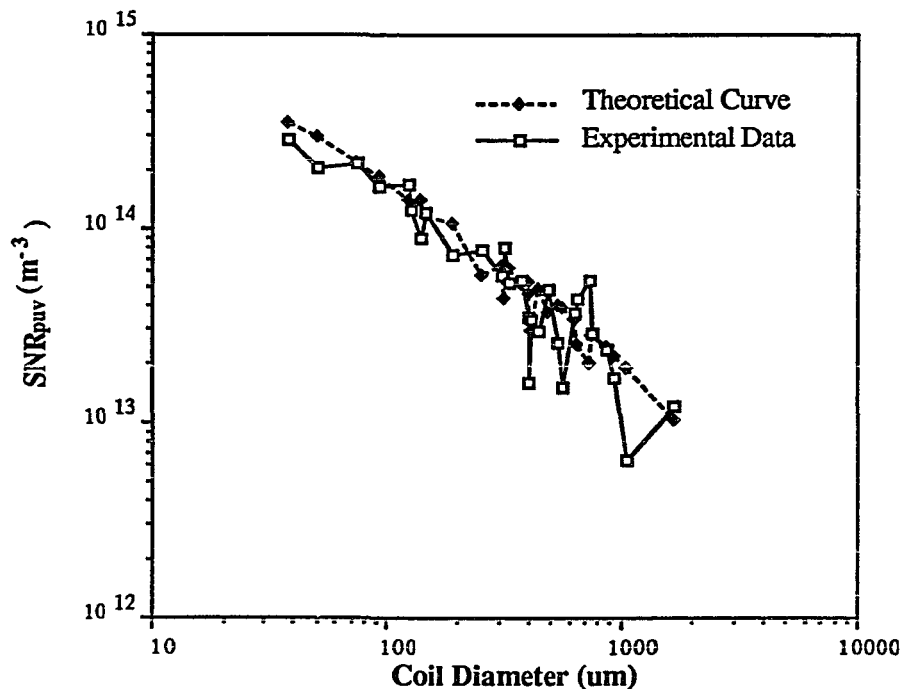


Figure 67 A logarithmic plot of  $SNR_{puv}$  vs. coil diameter. A  $1/d$  variation in  $SNR_{puv}$  appears as a straight line with a slope of -1.

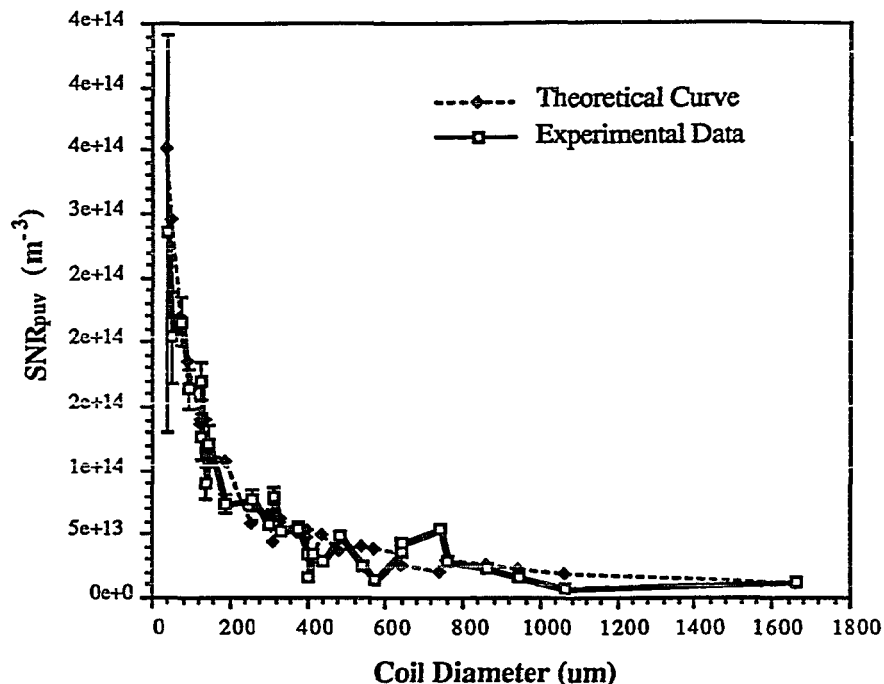


Figure 68  $SNR_{puv}$  for the series of microcoils, with error bars to indicate a 1 mm inaccuracy in the measurement of the length of the leads.

A second source of error arises from the measurement technique in which the signal and noise in the NMR experiment are calculated from the spectroscopic NMR signal. The "signal" is determined by integrating over the spectrum of the FID using software routines available on the SIS/200. The initial and final values of the integration are determined by the user. In this manner, baseline errors can be minimized. There is some error associated with the measurement of the signal, as the initial and final values of the integral must be properly chosen by the user. However, for slight adjustments in the initial and final values of the integral, we observed less than 5% variation in the magnitude of the measured signal. The measurement of the noise is less accurate than the measurement of the signal. The noise is determined by measuring the average peak spectral variation over the portion of the spectrum that does not contain the signal. We found that the noise could not be measured with better than 10% accuracy, and was as high as 20% for spectra in which the baseline was not well-behaved.

Third, the RF coil assemblies were not RF shielded, and there could have been error from external interference, although this error would likely be less than 10%.

Perhaps the most significant error results from the handling of the delicate coil assemblies. Microscopic "dents" or other imperfections in the wires of the coils would likely be unnoticed. Considering the technique of microcoil fabrication in which tweezers are used to hold, bend, and guide the wire as it is wrapped onto the glass capillary, such imperfections seem likely. The electrical connection of the coil to the UT-85SS<sup>11</sup> semirigid transmission line could have contributed to the loss. The larger coils, wound with 42 ga copper wire, were soldered to the transmission line, whereas the more delicate coils, wound with 50 ga and 56 ga gold wire, were secured using silver paint. Many factors could influence the quality of the connection, including the cleanliness of the surface and of the wires, and could have contributed to the error.

The error is almost equally distributed around the theoretical curve in Figures 65-67, and the overall trend of the experimental curve compares well with the theoretical curve. An experiment could be performed where several series of identical coils are constructed and tested in the NMR experiment. This would provide a statistical average whereby the errors indicated above could be further quantified. The symmetrical nature of the error in the theoretical SNR when compared to experiment would suggest that a more accurate experimental measurement could be made using this technique. Furthermore, the coils could be dismounted and remounted to the test assembly, and retested to compare the actual error which can result from the electrical connections. Such a procedure could also be advantageous for the electrical testing described in the previous section and represented in Figure 59.

### 3.4 Summary

The theoretical description of the thermal coil noise derived in Chapter 2 has been tested using larger coils wound with 16 ga wire at lower frequencies and using the scaling parameter  $z = d/\delta$ . The resistance model for coils with substantial wire separation ( $r_{sep}/d \geq 1.5$ ) and height-to-diameter

ratios of  $0.5 \leq h/d_{\text{coil}} \leq 2.0$  has been shown to be valid to within 25% when the end effect is not considered. By including an end effect factor ( $\zeta$ ) to account for the weaker field experienced by the turns of wire at the ends of the coil, the error is reduced to within 13%. A technique has been proposed whereby the empirical data from the larger coils are used to "finely tune" the theoretical model by adjusting the specific value of  $u'$  used in Eq. (50). In this manner, the error in the measurement of coil loss in the larger coils is reduced to within 2%.

The results of the complete theoretical description of coil loss for 5-turn solenoidal coils with  $r_{\text{sep}}/d = 2.0$  were incorporated into a computer program to assist in predicting the electrical characteristics of smaller coils. A "piecewise" approximation was used in the computer model, with an error of nearly 15% when calculating the loss in coils wound with 56 ga wire and used at 200 MHz ( $z \cong 2.2$ ). A series of microcoils with  $38 \mu\text{m} \leq d_{\text{coil}} \leq 1.8 \text{ mm}$  were constructed and tested. Eight of the microcoils were selected for resistance measurement using the Q measurement technique and an HP4195A network analyzer. The experimental data agreed with theoretical predictions, with a maximum error of 32%, but an average error of less than 1%. The standard deviation of the error was roughly 20%. The complete series of microcoils was used in  $^1\text{H}$  NMR spectroscopy experiments at 4.7 T (200 MHz) to evaluate the SNR for the coils. Similar to the results of electrical testing of microcoil resistance, the experimental data from SNR testing compared favorably with the predictions of the computer model, with an average error of 1%. The statistical error for the individual data points was symmetrically distributed about the theoretical value with a standard deviation of nearly 50%. This large spread in error could result from a variety of factors, including the approximations used in the theoretical model, the resistance of the coil leads, and the specific peculiarities inherently different for each individual coil assembly (e.g., the quality of the electrical connection). Further quantitation of the microcoil loss model would involve the testing of a series of similar microcoils. In such a manner, a statistical average coil performance could be obtained.

The good agreement of the average experimental  $\text{SNR}_{\text{puv}}$  from  $^1\text{H}$  NMR spectroscopy experiments (Figures 65-67) and from electrical testing using the Q measurement technique (Figure 59), with that theoretically predicted using the noise model (Eq. (50)), supports the noise

model chosen to characterize microcoils and the methodology used in this study to characterize coils of various geometries, materials, and intended frequencies of operation. The overall trend of the experimental SNR compares well with the theoretical expectations of Eqs. (48) and (49), and supports the claim that further enhancement to the SNR can be achieved using microcoils with diameters less than 38  $\mu\text{m}$ .

### 3.5 References

- <sup>1</sup>E. Odeblad, Micro-NMR In High Permanent Magnetic Fields, (Karolinska Institute, Dept. of Obstetrics and Gynecology, Stockholm, 1966).
- <sup>2</sup>L. Tippie and W. Clark, "Low-temperature Magnetism of Quinolinium (TCNQ)<sub>2</sub>, a Random-exchange Heisenberg Antiferromagnetic Chain. I. Static Properties," Phys. Rev. B **23**, 5846 (1981).
- <sup>3</sup>J. Sanny and W. Clark, "Microwave Electron Spin Resonance Spectrometer with operation to 54 mK in a Dilution Refrigerator," Rev. Sci. Instrum **52**, 539 (1981).
- <sup>4</sup>H. Mahdjour, W. Clark, and K. Baberschke, "High-sensitivity Broadband Microwave Spectroscopy with Small Nonresonant Coils," Rev. Sci. Instrum. **57**, 1100 (1986).
- <sup>5</sup>W. House, "NMR Microscopy," I.E.E.E. Trans. Nuc. Sci. **31** 570 (1984).
- <sup>6</sup>L. Hedges, "Microscopic Nuclear Magnetic Resonance," Ph.D. Thesis, State University of New York at Stony Brook, 1984.
- <sup>7</sup>J. Aguayo, S. Blackband, J. Schoeniger, M. Mattingly, and M. Hintermann, "Nuclear Magnetic Resonance Imaging of a Single Cell," Nature **322**, 190 (1986).
- <sup>8</sup>Z. Cho, C. Ahn, S. Juh, and H. Lee, "Nuclear Magnetic Resonance Microscopy with 4  $\mu\text{m}$  Resolution: Theoretical Study and Experimental Results," Med. Phys. **15** (6), 815 (1988).
- <sup>9</sup>X. Zhou, C. Potter, P. Lauterbur, and B. Voth, "3D Microscopic NMR Imaging with (6.37 $\mu\text{m}$ )<sup>3</sup> Isotropic Resolution," Abstracts, 8th Annual Meeting SMRM, Amsterdam, 286 (1989).
- <sup>10</sup>R. Medhurst, "H.F. Resistance and Self-Capacitance of Single-Layer Solenoids," Wireless Eng. **35**, 80 (1947).
- <sup>11</sup>Rosenberger Micro-coax, Box E, Collegeville, PA 19426.
- <sup>12</sup>"The Development of Microdomain RF Coils for NMR Microscopy," National Science Foundation Grant No. CA40293 (1991).
- <sup>13</sup>F. Terman, Radio Engineers' Handbook (McGraw-Hill Book Company, New York, 1943).

## 4. CONCLUSION

The objective of this study has been to extend the analysis of NMR RF coil design to microscopic domains. We have shown that the signal-to-noise ratio achieved in an NMR microscopy experiment can be considerably enhanced with the use of microcoils. We have shown that an analysis of the loss in microcoils is relatively straight forward and generally becomes clearer as the size of the coil is reduced. The increase in loss associated with the skin effect and the proximity effect in larger coils is not significant in smaller coils, where simple ohmic loss dominates and a direct current resistance model can be assumed.

The approach that we have taken to determine the loss in microcoils involves a scaling parameter ( $z$ ), which represents the diameter of the wire used in winding the coil relative to the skin depth of the coil at the frequency of operation. This provides a means whereby an accurate measurement of the coil loss can be made using larger coils at lower frequencies, and then scaled to apply to microcoils operated at higher frequencies. The advantages offered by this method include the construction and handling of larger, more durable coils and the use of sophisticated instrumentation available for accurate measurement of coil loss at lower frequencies. Additionally, there is less error involved in the testing of coil loss at lower frequencies, as the coil  $Q$  is smaller and the error due to parasitic effects is less. For example, the loss in 5-turn solenoidal coils with height-to-diameter ratios from 0.5 to 2.5 was predicted within 2% using this procedure. A further advantage of this methodology is that it can be applied to any coil geometry, and provides a means of tailoring the coil loss models to accurately represent the loss that occurs with a specific geometry.

This thesis has addressed the theoretical concerns of using microcoils for NMR microscopy. A series of microcoils with diameters from 1.8 mm to 38  $\mu\text{m}$  were constructed and used in NMR spectroscopy experiments at 4.7 T (200 MHz) to provide empirical verification of the SNR achieved using such coils. Of the common coil geometries used for NMR (e.g., saddle, birdcage, and solenoidal), solenoidal coils possess the best sensitivity and magnetic field homogeneity. Therefore, the microcoils used in this study were 5-turn, solenoidal coils. The results from NMR experiments

indicate that the SNR in microcoils can be predicted with an average error of 1%. Furthermore, the results of this study demonstrate that an enhanced SNR ratio can be achieved with microcoils as small as 38  $\mu\text{m}$ , and support the continued reduction of coil size for further enhancement in the SNR. However, there are additional concerns that must be considered in microscopic NMR. The absolute SNR measured using a 50  $\mu\text{m}$  diameter microcoil filled with 5 mM  $\text{CuSO}_4$ , with a sample volume of roughly  $(40 \mu\text{m})^3$ , was 1.34. This implies that approximately 64 separate acquisitions would be required to achieve an SNR of 10. Typical biological tissues, in the absence of contrast agents and doping agents, have  $T_1$  relaxation times on the order of several tenths of a second, e.g., 0.5 sec. The time (between acquisitions) required for the sample to return to equilibrium is generally accepted as  $5T_1$ . This implies a total acquisition time of  $[64 \text{ acq} \times (5 \times 0.5 \text{ sec})] = 160 \text{ sec}$ , i.e., 2.67 min. Smaller samples will require even longer acquisition times, as the overall SNR decreases with the volume of the sample. This is an important concern, considering that the acquisition time should be minimized to prevent unwanted biological changes (e.g., death) from occurring within the sample during the acquisition window. Furthermore, some processes (e.g., diffusion) that can be measured using microcoils and NMR are time-dependent. Therefore, regardless of the advantages of enhanced SNR and the shorter acquisition times offered by microcoils (when compared to larger coils), the overall SNR and the acquisition time permitted for a particular application must be considered when assessing the lower limits of microscopic NMR.

A second limitation to the further enhancement of the SNR achieved using smaller microcoils is that the diameter of the coil must be significantly greater than the diameter of the conductor used to wind the coil ( $d_{\text{coil}} > 5d$ ). For example, the mechanical stress that results in a bent wire becomes significant when the radius of curvature of the bend approaches the radius of curvature of the wire. This results in an increased wire resistance and an increased coil loss. This increase in loss would be difficult to quantitate, and would likely not be as important to the overall degradation of coil performance as would the deterioration of the magnetic field homogeneity and coil sensitivity that would result when  $d_{\text{coil}} \cong d$ . The magnetic field of the coil begins to deviate substantially from that of a solenoid when the central region of the coil is not well-removed from the individual conductors.

Current advances in microelectronic fabrication technology have provided means of etching conductors with widths as small as  $0.1\ \mu\text{m}$ . This would infer an absolute limit of  $0.5\ \mu\text{m}$  for the smallest microcoil that can be built using current methods of fabrication.

The use of microcoils in microscopic NMR imaging and spectroscopy provides an increased signal-to-noise ratio, and may provide the tools for localized examination of biological structures and chemical reactions, as well as new information on the molecular dynamics of NMR active chemical species (e.g.,  $^1\text{H}$ ,  $^{31}\text{P}$ ,  $^{13}\text{C}$ ,  $^{19}\text{F}$ ,  $^{23}\text{Na}$ ) in biological structures at the cellular level. The resolution achieved in NMR imaging experiments is directly related to the  $\text{SNR}_{\text{puv}}$ . However, there are additional factors which must be considered which compete against resolution enhancement at reduced geometries, including diffusion effects and susceptibility variations.

## APPENDIX A.

### SAMPLE NOISE

Conducting samples are electrically lossy, and one must be careful to include the sample contribution when calculating the total experimental noise. Sample noise may be considered to result from the Brownian motion of the electrolytes within the conducting medium. The Nyquist formula may be used to determine the sample noise in the same manner used to determine the coil noise. The difficult task becomes finding the effective resistance of the sample. Hoult and Lauterbur have investigated sample noise in a paper published in 1978.<sup>1</sup> In this study, they assume a 100 mM concentration of saline solution, representative of that found in the human body, and found that a spherical sample of this concentration had an effective noise resistance given by

$$R_s = \frac{2\pi\omega_0^2 B_1^2 b^5}{15\rho_{\text{sample}}}$$

where  $b$  is the sample radius and  $\rho$  is its resistivity. The total noise resistance is the sum of the coil and sample noise resistances ( $R_{\text{noise}} = R_c + R_s$ ) where the macroscopic coil resistance model can be used to determine  $R_c$  in the size regime where the consideration of sample noise is important. From Eq. (43) of the text

$$R_c = \frac{3\rho n^2 d_{\text{coil}} \xi}{2h\delta} \quad n \gg 1$$

where  $n$  is the number of turns,  $h$  is the coil height (length),  $\xi$  is the proximity effect factor,  $\delta$  is the skin effect factor,  $\rho$  is the resistivity of the wire, and  $d_{\text{coil}}$  is the coil diameter. The coil resistance ( $R_c$ ) is seen to be independent of coil size, provided that  $d_{\text{coil}} \cong h$ .

The sample resistance ( $R_s$ ), however, is heavily dependent on sample diameter, varying as  $b^5$  for biological samples. Larger samples have a higher effective resistance than smaller samples, and

tend to "load" the coil much more severely than a smaller sample does, i.e.,  $R_s \gg R_c$ . Coil loading is really a consequence of the principle of reciprocity, in which the electrolytes of the sample are perturbed by the electric and magnetic field of the coil. Currents are induced when the lines of force of a varying magnetic field thread through a conducting mass. The electrolytes in the sample serve as the charge carriers for this current. Analogous to proximity effect, the eddy currents induced in the sample by the magnetic field of the coil result in an increased effective coil impedance and is termed "coil loading." Coil loading is a useful concept, for it provides a relatively easy method of measuring  $R_s$ . The overall quality factor of the loaded coil ( $Q_{\text{loaded}} = \omega L / (R_c + R_s)$ ) is reduced over that of the unloaded coil ( $Q_c = \omega L / R_c$ ) by an amount  $R_c / (R_c + R_s)$ . The value of  $Q_{\text{loaded}}$  can be easily measured using a network analyzer and magnetic field probes with the sample inserted in the coil, and compared with  $Q_c$  which is measured in the same manner but with the sample removed. This process can be used to determine the value of  $R_s$  experimentally.

There is a point of intersection, a "critical diameter," above which the sample noise dominates the noise of the coil and below which the sample noise may be neglected. It has been shown that  $d_{\text{critical}} \cong 7$  mm at 300 MHz when using a 5-turn solenoidal RF coil with the optimum Q geometry.<sup>2</sup> A plot of sample noise and coil noise versus coil and sample diameter at 300 MHz is shown in Figure A.1. This plot clearly demonstrates that sample noise can be neglected when using microdomain coils with "typical" biological samples.

The signal-to-noise ratio in an NMR experiment immediately following a  $\pi/2$  pulse has been given as

$$\text{SNR} = \frac{\text{rms signal}}{\text{rms noise}} = \frac{k_0 B_{1,y} v_s N \gamma \hbar^2 i(i+1) \omega_0^2 / 3kT_s}{\sqrt{8k\Delta f (R_c T_c + R_s T_s)}}$$

By factoring out the experimental constants in the above equation and by substituting in the

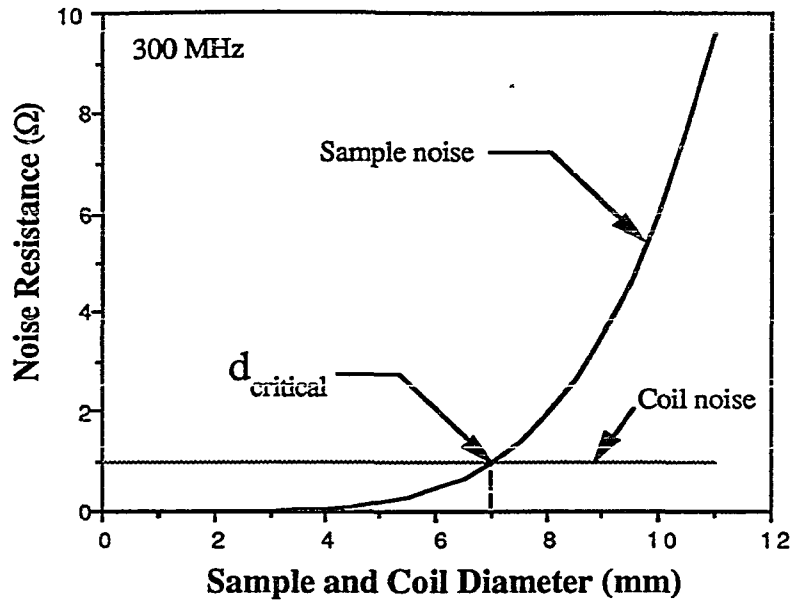


Figure A.1 Coil and sample noise resistance, considering a solenoidal (cylindrical) geometry and biological samples.

expressions for  $R_c$  and  $R_s$ , the SNR is given by

$$\text{SNR} \propto \frac{\omega_0^2 B_1 v_s}{\sqrt{\epsilon n^2 \omega_0^{1/2} + \beta \omega_0^2 B_1^2 b^5}}$$

where  $\epsilon$  and  $\beta$  are constants and where  $\delta \propto 1/\sqrt{\omega_0}$ . For the regime in which sample noise dominates ( $d \gg d_{\text{critical}}$ )

$$\text{SNR} \propto \frac{\omega_0^2 B_1 v_s}{\sqrt{\beta \omega_0^2 B_1^2 b^5}} \propto \frac{\omega_0 b^3}{b^{5/2}} = \omega_0 b^{1/2}$$

It is evident that although the signal from the sample decreases with volume ( $b^3$ ), the noise also decreases at nearly the same rate ( $b^{5/2}$ ), resulting in an overall SNR that varies as the square root of the sample diameter. This small variation in SNR with sample size is normally not severe, and may be compensated by a variety of means, including temporal averaging of the FID. This provides an increased SNR by averaging the signals from repeated acquisitions. The signals from each successive acquisition are correlated while the noise is uncorrelated. Thus, an SNR increase of  $\sqrt{n_{\text{acq}}}$  is achieved, where  $n_{\text{acq}}$  is the number of signal acquisitions.

For the regime in which coil noise dominates ( $d \ll d_{\text{critical}}$ )

$$\text{SNR} \propto \frac{\omega_0^2 B_1 v_s}{\sqrt{\epsilon n^2 \omega_0^{1/2}}} \propto \omega_0^{7/4} B_1 b^3$$

This regime shows a much greater variation of SNR with sample size, varying as  $b^3$ . The reduction in signal is not compensated by a lower noise because the coil noise now dominates and remains insensitive to changes in sample and coil diameter. The overall SNR decreases for smaller sample volumes, and is one of the primary limitations of submillimeter NMR.

## A.1 References

- <sup>1</sup>D. Hoult and P. Lauterbur, "The Sensitivity of the Zeugmatographic Experiment Involving Human Samples," *J. Magn. Reson.* **34**, 425 (1979).
- <sup>2</sup>Z. Cho, C. Ahn, S. Juh, and H. Lee, "Nuclear Magnetic Resonance Microscopy with 4  $\mu\text{m}$  Resolution: Theoretical Study and Experimental Results," *Med. Phys.* **15** (6), 815 (1988).

## APPENDIX B.

### ADDITIONAL CONCERNS

Figure B.1 illustrates some of the factors that must be considered in the submillimeter NMR experiment. At extremely small coil and sample diameters ( $d \ll 100 \mu\text{m}$ ), false signals may arise due to water adsorbed onto the coil and from protons in the coil support and insulation (e.g., in the epoxy used to hold the wires of the solenoid secure). Water vapor may condense within the coil itself, leading to a false signal. In addition, the interaction between the water molecules and the glass (capillary) coil former may lead to a local decrease in the relaxation times at the sample-former interface. This would be particularly important at the large surface area-to-volume ratios encountered at these extremely small dimensions.<sup>1</sup> For a solenoid, the surface area-to-volume ratio is given by

$$\frac{\text{Surface Area}}{\text{Volume}} = \frac{\pi d_{\text{coil}}}{(\pi d_{\text{coil}}^2)/4} \propto \frac{1}{d_{\text{coil}}}$$

and is drastically increased for submillimeter coils.

There are other effects which may be significant at extremely small diameters. As the sample protons which provide the NMR signature diffuse into different regions of the sample, the received information is effectively smeared. In the absence of diffusional barriers (e.g., cell membranes), an average free diffusion length can be defined by

$$(\Delta r)_{\text{free}} \propto \frac{1}{\sqrt{D\tau_{\text{acq}}}}$$

where  $D$  is the free diffusion constant and  $\tau_{\text{acq}}$  is the time over which the NMR signal is acquired.

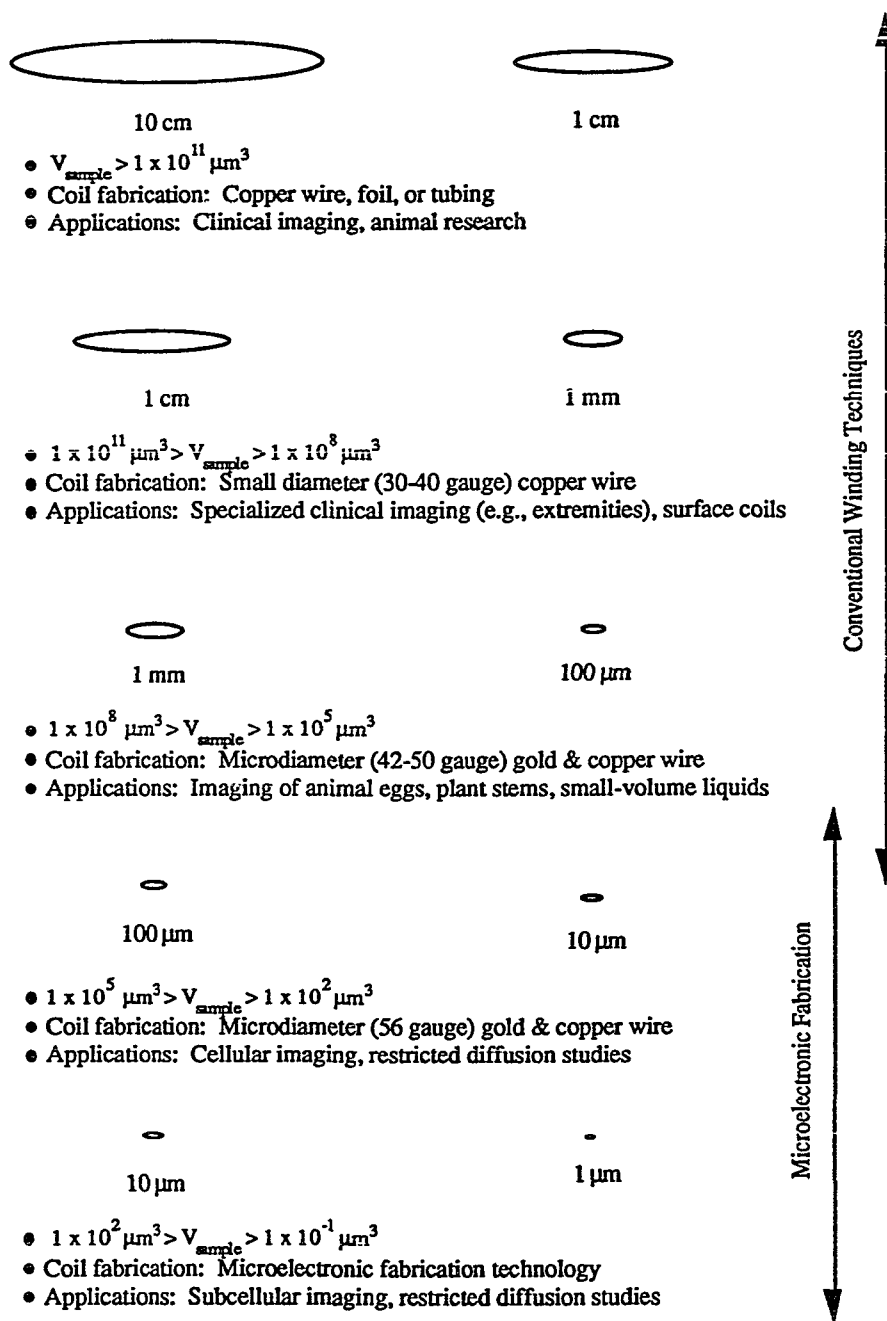


Figure B.1 Additional concerns in submillimeter NMR.

Typically,  $(\Delta r)_{\text{free}} \cong$  several  $\mu\text{m}$ . This may pose limitations when attempting high-resolution NMR imaging. This is primarily because an element of magnetization accumulates a phase shift as it traverses a region to which a magnetic field gradient has been applied. This accumulated phase shift leads to artifacts in the NMR image and to a loss in the SNR due to incomplete rephasing.

There has been considerable recent advancement in the theoretical description of restricted diffusion in the presence of nonpermeable or semipermeable barriers. Hyslop and Lauterbur<sup>2</sup> have shown from theoretical calculations and computer simulations that motional narrowing occurs in the presence of diffusional barriers, and that an enhanced spectral peak will appear at a distance  $(\Delta r)_{\text{restricted}}$  from such a barrier. For an impermeable barrier within a sample subjected to magnetic field gradient  $G$

$$(\Delta r)_{\text{restricted}} = \sqrt[3]{\frac{10\gamma_p D}{\gamma G D_w}} \quad (\text{B.1})$$

where  $\gamma_p$  and  $\gamma$  are the proton and sample gyromagnetic ratios, respectively, with  $D_w$  and  $D$  being the free diffusion coefficients of water and of the sample, respectively. They have concluded that restricted diffusion could affect NMR images with resolutions of  $10 \mu\text{m}$ .

An even greater and potentially more far-reaching effect that has a detrimental influence on the SNR in the NMR experiment, especially at microscopic dimensions, is magnetic susceptibility variations. Variations in the magnetic susceptibility ( $\chi$ ) between the different materials comprising the coil assembly – the wire, glass, epoxy, and the sample – may lead to a localized nonlinear distortion of the main magnetic field around the region of the coil assembly. The concept of a susceptibility induced magnetic field distortion may be best understood by considering a spherical shell with  $\chi \neq 0$  (i.e.,  $\mu_{\text{shell}} = \mu_0(1+\chi) \neq \mu_0$ ) placed in a uniform magnetic field  $\mathbf{B}_0$  as shown in Figure B.2.

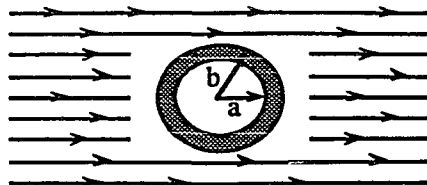


Figure B.2 A spherical shell immersed in a uniform static magnetic field.

The local  $\mathbf{B}$  field at the shell can be found via the scalar potential  $\Phi_m$  where

$$\mathbf{B} = \mu\mathbf{H} = -\mu\nabla\Phi_m$$

and where  $\Phi_m$  satisfies Laplace's equation

$$\nabla^2\Phi_m = 0$$

in the region of interest. The net magnetic field  $\mathbf{B}_{\text{outer}}$  which results outside the spherical shell is a superposition of the main field  $\mathbf{B}_0$  and a dipole field  $\mathbf{B}_d$  (see Figure 7) with the dipole moment  $\mathbf{m}$  oriented parallel to  $\mathbf{B}_0$  ( $\hat{\mathbf{a}}_z\mathbf{B}_{\text{outer}} = \hat{\mathbf{a}}_z\mathbf{B}_0 + \hat{\mathbf{a}}_z\mathbf{B}_d$ ). Due to the overwhelming magnitude of the main field ( $\mathbf{B}_0$ ), only the components of the dipole field which are oriented parallel to  $\mathbf{B}_0$  will have a measurable contribution to the overall magnetic field. Inside the shell,  $\mathbf{B}_{\text{inner}}$  is uniform, oriented parallel to  $\mathbf{B}_0$  with a magnitude given by<sup>3</sup>

$$\mathbf{B}_{\text{inner}} = \frac{9\mu}{(2\mu+1)(\mu+2) - 2\frac{a^3}{b^3}(\mu-1)^2} \mathbf{B}_0$$

For the special case of  $\mu \gg 1$ , the inner field is proportional to  $\mu^{-1}$  and vanishes for an infinitely permeable material. This effect is known as magnetic shielding. The lines of  $\mathbf{B}$  tend to pass through the region of highest permeability and are shown in Figure B.3.

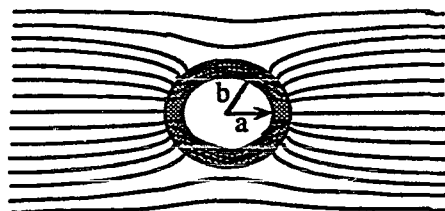


Figure B.3 Magnetic shielding.

The local distortion of  $B_{\text{outer}}$  and the elimination of  $B_{\text{inner}}$  resulting from the susceptibility discontinuity at the boundaries of the shell are quite evident.

This phenomenon occurs in NMR, albeit to a lesser extent, when the main magnetic field  $B_0$  encounters the materials of a coil assembly or even the sample itself. Susceptibility discontinuities arise at the interface of two different media, e.g., the sample-air interface and the wire-coil former interface. The result is that the sample is not subjected to a perfectly uniform static magnetic field. Consequently, the received NMR signal lineshape is broadened in accordance with the local  $B$  field. A common method employed at larger (macroscopic) dimensions to correct for magnetic field inhomogeneity is magnetic field *shimming*, which is performed using magnetic field shim coils. By properly positioning the shim coils in the magnet, a dc current can be used to correct for bulk susceptibility distortions, i.e., those which globally affect the sample and originate well outside of the sample region.

A far more serious problem arises when local susceptibility discontinuities occur within the sample itself or at the sample boundary. In microscopic NMR, the relatively small ratio of sample volume to surface area implies that a great deal of the sample is located adjacent to significant susceptibility variations, e.g., along the wall of the capillary around which a length of wire has been secured. Furthermore, contaminants may pose a serious problem. For example, the presence of minute air bubbles in a sample volume is common. At the small sample volumes encountered in microscopic NMR, an air bubble could occupy a substantial fraction of the sample volume. Thus, the presence of air bubbles will not only decrease the overall filling factor of the coil but will also cause

significant distortion of the magnetic field lines due to discontinuity of permeability at the sample-air interface, and will result in a broadened spectral linewidth.

The difficulties arising from diffusion and susceptibility distortions are not mutually exclusive. A linear, uniform magnetic field gradient was assumed in Eq. (B.1). In the presence of local susceptibility distortions, the field gradient will not be uniform. A much more complicated model which accounts for both phenomena simultaneously would be required to represent the physical situation accurately.

## B.1 References

- <sup>1</sup>E. Odeblad, Micro-NMR In High Permanent Magnetic Fields, (Karolinska Institute, Dept. of Obstetrics and Gynecology, Stockholm, 1966).
- <sup>2</sup>W. Hyslop and P. Lauterbur, "Effects of Restricted Diffusion on Microscopic NMR Imaging," J. Magn. Reson. **94**, 501 (1991).
- <sup>3</sup>J. Jackson, Classical Electrodynamics, (John Wiley & Sons, New York, 1975).

## APPENDIX C.

### CONSTRUCTION OF MICROCOILS

The microcoils used in this study were constructed manually, with the use of a dissecting microscope. A series of solenoidal microcoils have been constructed, ranging in size from 38  $\mu\text{m}$  to 2 mm diameter. The coils are wound on hollow glass (pulled capillary pipet) formers using 42 ga copper wire, and 50 ga and 56 ga gold wire. Conventional winding techniques are implemented,<sup>1</sup> similar to those used in wrapping larger coils. The glass capillary onto which the coil is wound is first secured in a pin vise supported by an adjustable micro-manipulation stand. The capillary can serve as the sample holder as well as the coil former. The sample can be preloaded into the capillary before the coil is wound, or it can be inserted into the finished coil assembly. Figure C.1 is a picture taken by a microscope camera of a capillary with 400  $\mu\text{m}$  diameter. The capillary has been preloaded with a cylindrical silicone sample. The silicone appears white in color in Figure C.1, and is suspended in epoxy cement for the purpose of maintaining a fixed position. Some air bubbles are trapped within the epoxy, and are visible in the picture.

To begin the winding process, a set of dual wires are secured side-by-side to the glass former using epoxy and are weighted to maintain constant tension as they hang from the capillary. The end of the wires that is secured to the capillary should be somewhat removed from the region of the capillary intended for the coil, as this will provide one of the coil's leads. For the smaller wires, a piece of tape will suffice for the weight. The pin vise is gently rotated as the wires are simultaneously wound onto the capillary, with each subsequent turn placed immediately adjacent to the previous turn as shown in Figure C.2. The wire used in winding this particular coil is 50 ga gold wire. The use of dual wires provides a uniformity to the winding that would be difficult to achieve if only a single wire were wound. The number of turns wrapped onto the capillary should be slightly greater than the number of turns desired in the final coil.

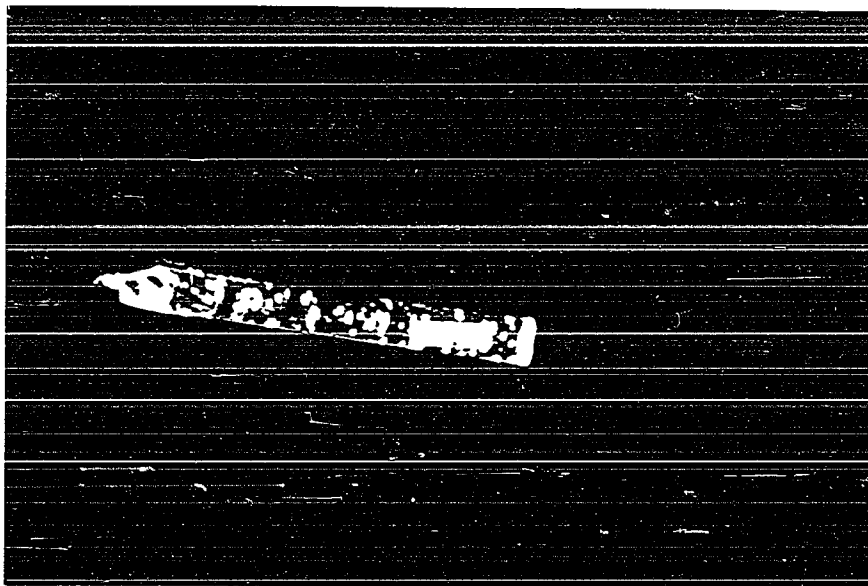


Figure C.1 A 400  $\mu\text{m}$  diameter capillary, loaded with a silicone sample.

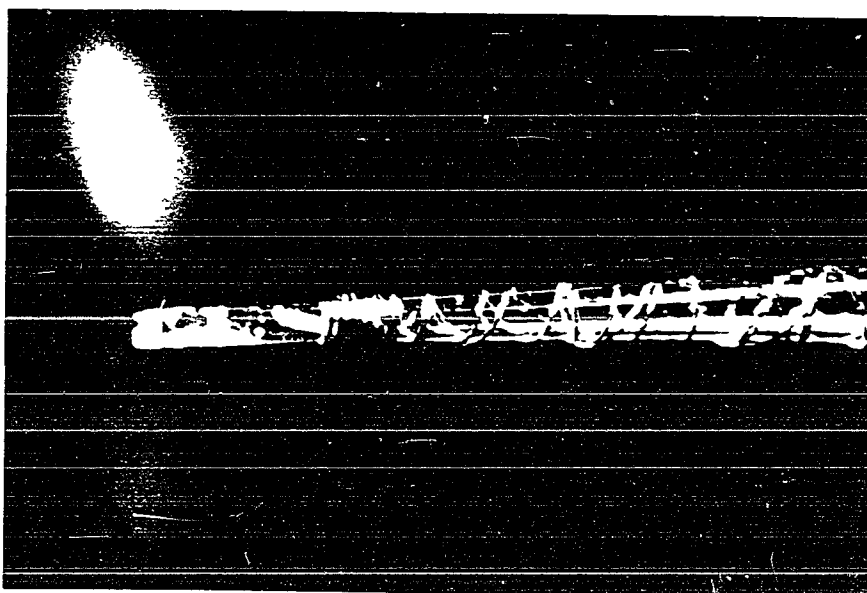


Figure C.2 A dual set of copper wires are wound onto the glass capillary.

With the wires held in place by the weights, a light coating of epoxy is applied to the wires as shown in Figure C.3. It is imperative that the coating be as thin as possible, as the subsequent steps in the construction of the coil require removal of some of the turns from the capillary. When the epoxy coating has dried, the weights are disconnected, leaving one end of the wires accessible. Microscopic tweezers are used to grasp one of the wires, and the pin vise is gently rotated in the direction opposite to that used when wrapping the wires, thereby removing the wire from the capillary as shown in Figure C.4. This results in a coil with more than the desired number of turns but with a uniform wire spacing of  $r_{\text{sep}} = 2d$ . With one of the wires completely removed, a second light coating of epoxy is applied to the assembly, as shown in Figure C.5.

The end of the wire secured to the capillary at the beginning of the winding process is unfastened from the capillary, leaving both ends of the wire accessible. The tweezer is used to remove a portion of the wire from the capillary. Wire can be removed using either of the two leads. In such a manner, the wire is removed until the number of turns desired for the final coil remains and the coil is positioned directly over the sample, shown in Figure C.6. A final coating of epoxy is applied to the coil, to protect the coil from damage that could result from handling the coil and from securing the coil to the tuning and matching capacitors in the resonant circuit. As such, this final coating can be considerably thicker than the previous coatings. In Figure C.7, an enlarged view of the completed, 9-turn solenoid is provided. Early coils were constructed with as many as 20 turns, with the later coils used in NMR testing having 5 turns.

Another early coil, a 20-turn solenoidal coil of 110  $\mu\text{m}$  diameter, was wound using 56 ga copper wire and is shown in Figure C.8. The minute overall size of the coil can be appreciated when compared to a hair, located adjacent to the coil in the picture. The completed microcoil must be resonated at 200 MHz for use in NMR spectroscopy experiments at 4.7 T. Early microcoils were secured to copper-clad circuit boards as illustrated in Figure C.9 for a 240  $\mu\text{m}$  coil wound using 50 ga gold wire. The coil in Figure C.9 is soldered to a copper board. The tuning and impedance matching capacitors are also soldered to the copper board, and a BNC coaxial connector is secured to connect the resonant circuit to a transmission line, as shown in Figure C.10.

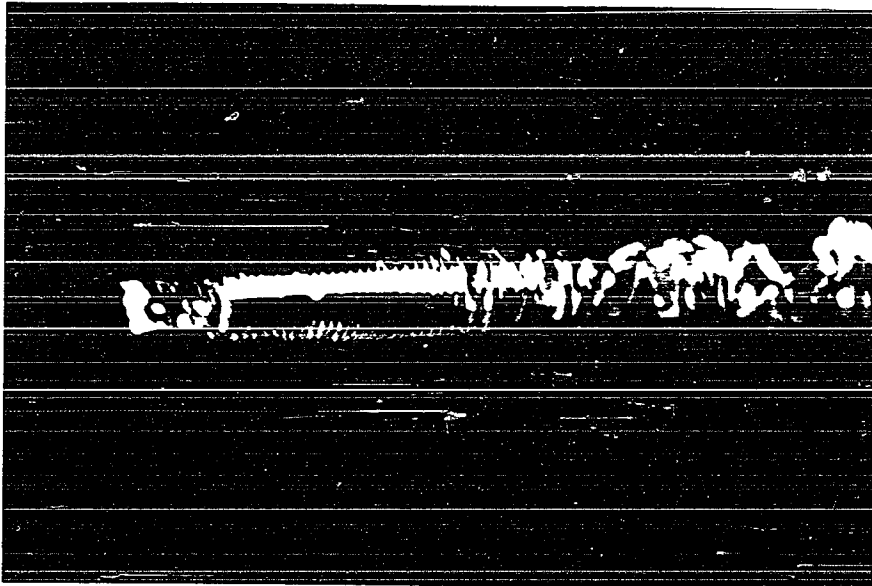


Figure C.3 After the wires have been wound onto the capillary, a light coat of epoxy is applied to secure the wires.

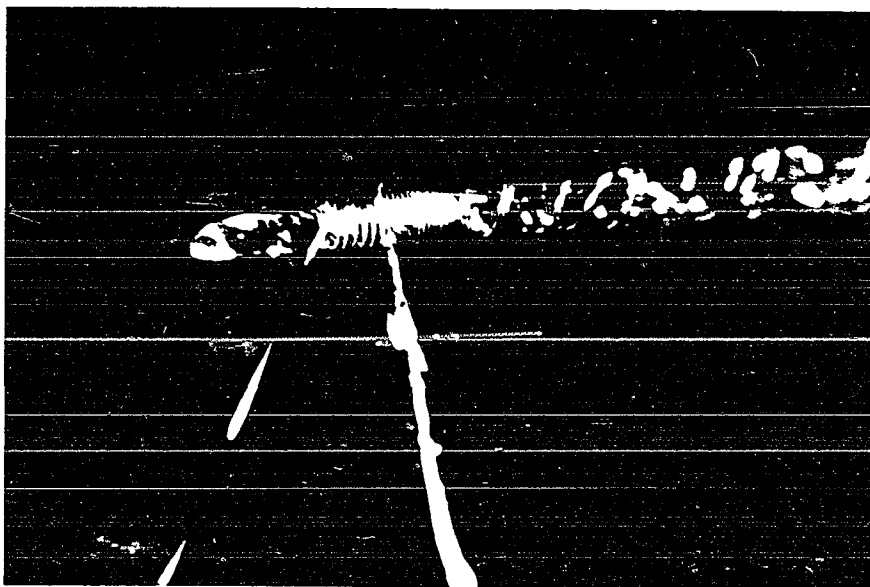


Figure C.4 One of the wires is carefully removed, leaving a single wire.



Figure C.5 The coil which results has a uniform inter-turn spacing of  $2d$ .



Figure C.6 The coil length can be adjusted by removing some of the turns. A final coat of epoxy is applied for rigidity.

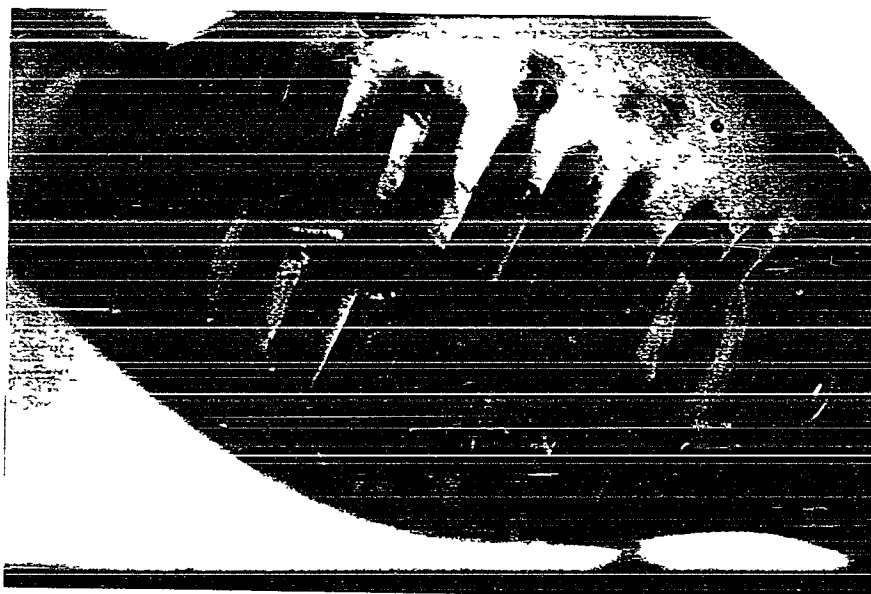


Figure C.7 A close-up view of the completed 463  $\mu\text{m}$  diameter microcoil.

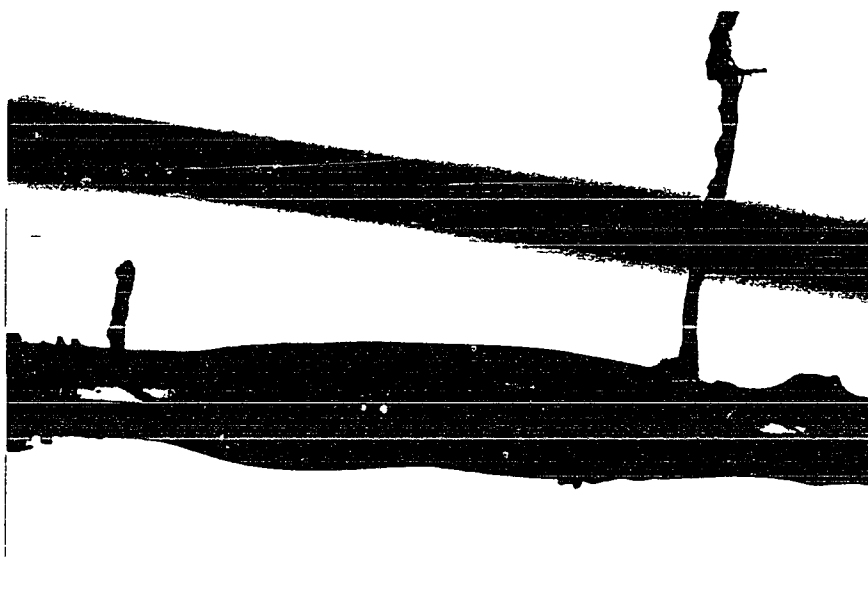


Figure C.8 A 20-turn, 110  $\mu\text{m}$  diameter microcoil and a human hair.

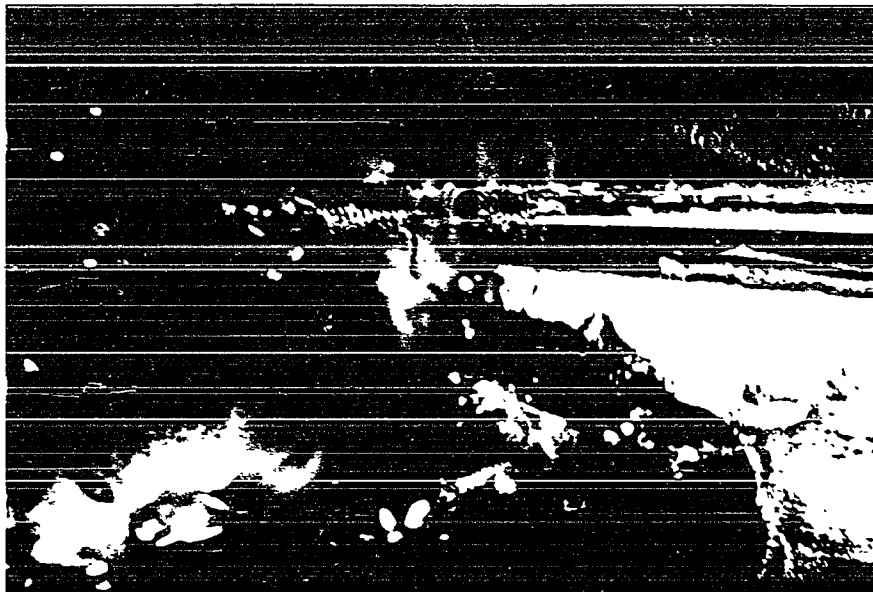


Figure C.9 A 240  $\mu\text{m}$  diameter coil, soldered to a copper-clad board.

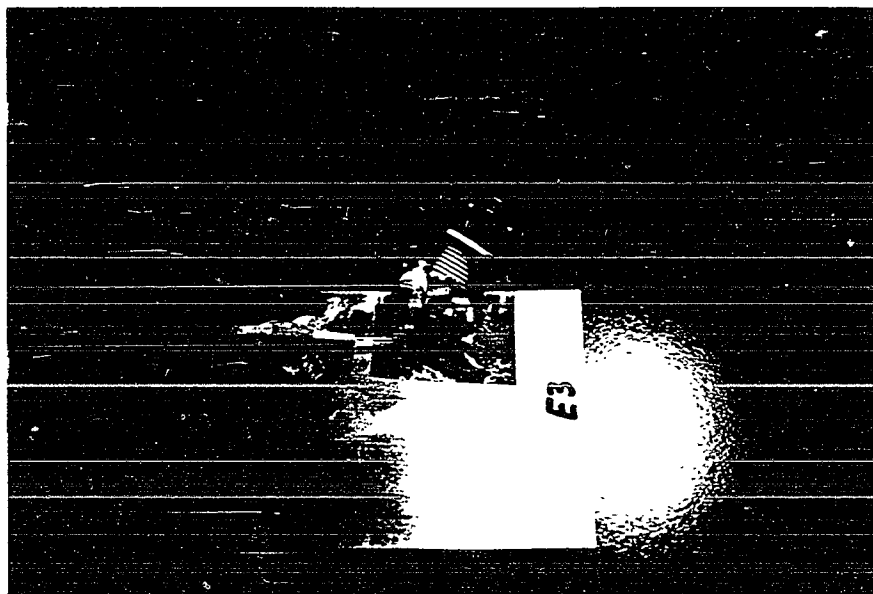


Figure C.10 The completed assembly includes the coil and the tuning and impedance matching capacitors.

The capacitors used for tuning and impedance matching are special "nonmagnetic" capacitors, designed for minimum susceptibility. (In this context, "nonmagnetic" applies equally to the dielectric as well as the conductive end-caps). The entire assembly is inserted into the magnet for the NMR experiment.

The coils used in later studies were secured using silver conducting paint, as extreme caution is required when soldering to insure that the heat from the soldering iron does not melt the delicate gold and copper wires. Furthermore, the sample inside the capillary is frequently damaged, and sometimes ejected from the capillary, from the radiant heat from the heated wire. Silver paint provided a good electrical contact, and minimized the damage to the coil and sample. A smaller (2.2 mm diameter), semirigid coaxial cable was also used and served as a mount to which the coil and capacitors could be secured. Chip capacitors are used in this mounting in accordance with the reduced geometry. A completed coil assembly is illustrated in Figure C.11, where a 320  $\mu\text{m}$  microcoil (wound using 50 ga gold wire) is secured using silver paint. The capacitors were presoldered to the transmission line for rigidity.

The semirigid coaxial cable affords a more compact circuit geometry; consequently, the parasitic effects arising from the leads of the coil are minimized. However, the susceptibility of the capacitors is significant, and even in the case of the special nonmagnetic capacitors can lead to an FID spectrum that is substantially broadened. A compromise is achieved by using the smaller coaxial cable to mount the coil, with the tune and match capacitors well-removed from the coil region. Figure C.12 is a picture of such an assembly, where the coaxial cable has been soldered to a narrow copper-clad board, to which the tune and match capacitors are fixed. The resonant circuit is electrically connected to the NMR spectrometer via a flexible coaxial cable as shown in the picture, and the entire assembly is inserted into the magnet for NMR testing. The assembly shown in Figure C.12 is that used for NMR experiments using microcoils to obtain the results presented in this thesis.



Figure C.11 A 320  $\mu\text{m}$  diameter coil, secured to a semirigid coaxial transmission line using silver paint. The tuning and matching capacitors are chip capacitors.

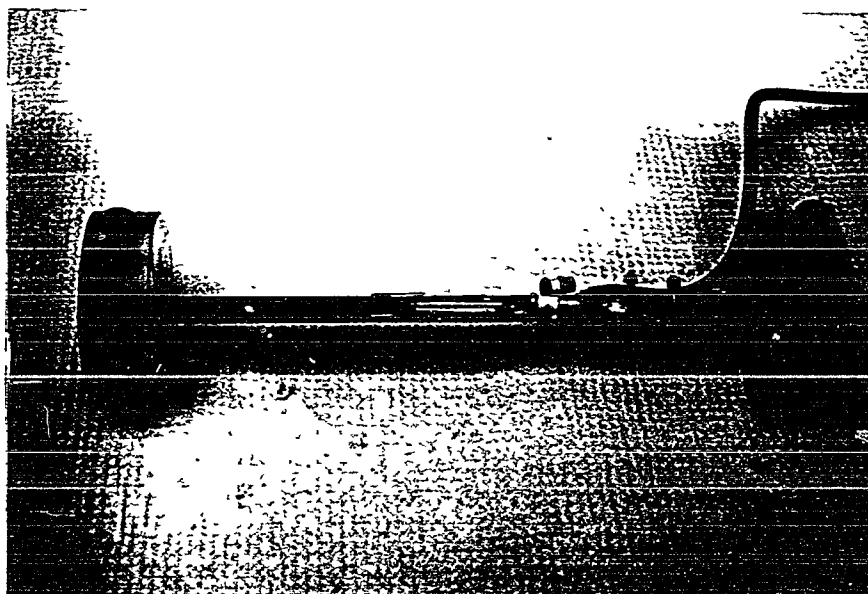


Figure C.12 The completed assembly, where the microcoil is separated from the variable tuning and matching capacitors.

## C.1 References

<sup>1</sup>H. Mahdjour, W. Clark, and K. Baberschke, "High-sensitivity Broadband Microwave Spectroscopy with Small Nonresonant Coils," Rev. Sci. Instrum. **57**, 1100 (1986).

## APPENDIX D.

### MICROCOIL RESISTANCE MEASUREMENT

Eight of the microcoils were selected for resistance measurement using the HP4195A network analyzer, as described in the text. This appendix presents the Smith chart plots for the eight coils, providing the inductance ( $L$ ) and the  $Q_c$  of the coil, from which the coil resistance is determined:

$$R_c = \frac{2\pi f L}{Q_c} \quad (\text{D.1})$$

where  $f$  is the frequency of interest. The specifications of the coils are given in Table D.1.

Table D.1 MICROCOILS TESTED USING THE Q MEASUREMENT  
TECHNIQUE TO DETERMINE  $R_c$ .

Coil #	Diameter (diam)	Wire Gauge
J19	123 $\mu\text{m}$	56
J15	190 $\mu\text{m}$	50
J17	313 $\mu\text{m}$	56
J22	333 $\mu\text{m}$	42
J7	543 $\mu\text{m}$	42
J6	643 $\mu\text{m}$	42
J10	745 $\mu\text{m}$	50
J4	863 $\mu\text{m}$	42

The first step in the Q measurement technique is to determine the coil inductance. The microcoils were fixed to a UT-85SS semirigid coaxial cable, and then the coil impedance ( $Z_c$ ) at 200 MHz was measured with the network analyzer. As explained in the text, the measurement of the reactive component of the coil impedance (i.e., the inductance) is relatively straightforward, as typical microcoil reactance values are on the order of 10  $\Omega$ . However, the value of the resistive component of microcoil impedance (at 200 MHz) is roughly two orders of magnitude less than that of the reactive component. (An exception is microcoils wound with 56 ga wire, as explained below.) Therefore, the determination of  $R_c$  from a simple measurement of  $Z_c$  at 200 MHz is not accurate. The Smith chart plots of  $S_{11}$  corresponding to the inductance measurements for each of the microcoils are shown in the

(a) figures for each coil (e.g., Figure D.2(a) is the Smith chart plot of  $S_{11}$  corresponding to the inductance measurement of Coil J15).

The second step in this technique is to resonate the microcoil with a capacitor, at a frequency ( $f_{res}$ ) close to 200 MHz. As explained in the text, the reactive component of the resonant circuit impedance is zero at resonance, and the resistive component of the resonant circuit impedance is the coil resistance, transformed to a higher value by the resonant phenomenon. The coil resistance can be extracted from the circuit Q by using Eq. (D.1), where  $Q_{ckt} \equiv Q_c$ . This provides a more accurate measurement of the resistive component of the microcoil impedance. Ideally, the value of  $f_{res}$  should be exactly 200 MHz, but this would require a resonating capacitor that could be finely tuned. The resonating capacitors used for this measurement were small Murata chip capacitors<sup>1</sup>, with typical lengths of 1-2 mm. Such capacitors minimize the parasitic impedances that result from excess lead lengths. Tunable capacitors are somewhat larger than several mm, and were not used. However, the theoretical resistance was determined from the computer model at the experimental resonant frequency ( $f_{res}$ ) to provide an accurate comparison of theoretical and experimental measurements.

The HP4195A network analyzer displays on its screen the value of resistive and reactive impedance (R and X, respectively) for the device under test. This is quite useful, as the exact value of the resonant frequency (i.e., where  $X = 0$ ) and the upper and lower 3 dB points (i.e., where  $X = R$ ) of the resonant curve are readily available. The (b) figures show the resonant frequency of the coil, and the (c) and (d) figures show the lower and upper 3 dB points, respectively. The coil Q is determined using

$$Q_c = \frac{f_{res}}{f_{upper} - f_{lower}} \quad (D.2)$$

from which the resistance is determined using Eq. (D.1) and the measured value of microcoil inductance. (Inductance remains relatively constant with frequency, and the value of L at 200 MHz can be used in Eq. (D.1), provided that  $f = f_{res}$  is close to 200 MHz, e.g., within 20%. In both the theoretical calculation and the experimental measurement, the value of  $R_c$  included the leads of the

microcoil. A comparison of theoretical and experimental results is provided in Table D.2, and is graphed in Figure 59 of the text.

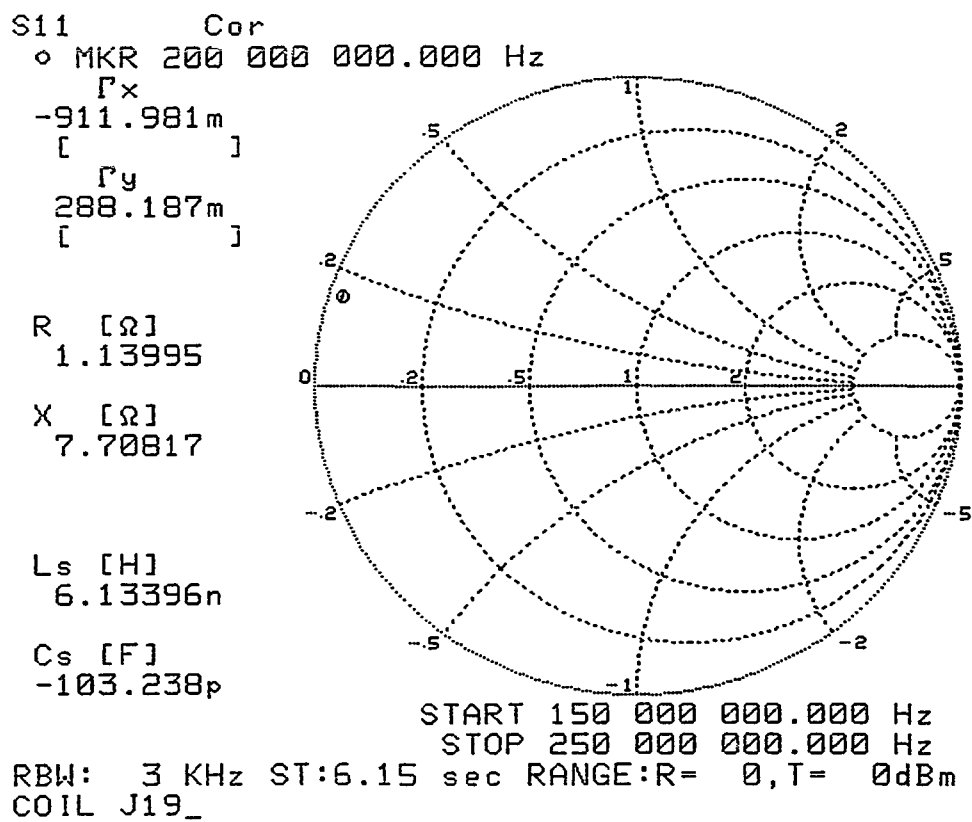
Table D.2 MICROCOIL RESISTANCE VALUES – EXPERIMENT VS. THEORY.

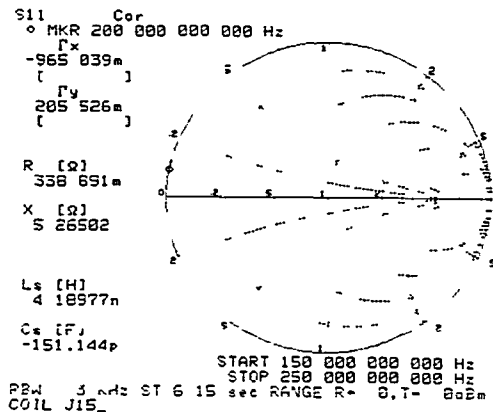
Coil #	$R_c$ (Theory)	$R_c$ (Exp)	% Error
J19	1.29 $\Omega$	1.14 $\Omega$	11.6 %
J15	0.441 $\Omega$	0.497 $\Omega$	11.3 %
J17	1.59 $\Omega$	1.30 $\Omega$	18.2 %
J22	0.222 $\Omega$	0.292 $\Omega$	-31.5 %
J7	0.377 $\Omega$	0.282 $\Omega$	25.0 %
J6	0.299 $\Omega$	0.333 $\Omega$	-11.4 %
J10	1.05 $\Omega$	1.28 $\Omega$	-21.9 %
J4	0.378 $\Omega$	0.407 $\Omega$	-7.6 %

The Smith chart plots showing  $S_{11}$  for the eight microcoils for the determination of L ((a) figures),  $f_{res}$  ((b) figures),  $f_{lower}$  ((c) figures), and  $f_{upper}$  ((d) figures) are provided below in Figures D.1 – D.8, and were obtained using the network analyzer. An exception is for Coil J17 and Coil J19, for which a single Smith chart plot of  $S_{11}$  is obtained. These coils are wound with 56 ga wire, and are too delicate to accurately fix to a resonating capacitor (with minimum coil lead lengths). However, the resistance of coils wound with smaller wire is higher, and a more accurate measurement of  $R_c$  is possible, directly from the  $S_{11}$  measurement of coil impedance, than is possible with coils wound with wires of larger diameter. Hence, the Q measurement technique was not used for Coils J17 and J19.

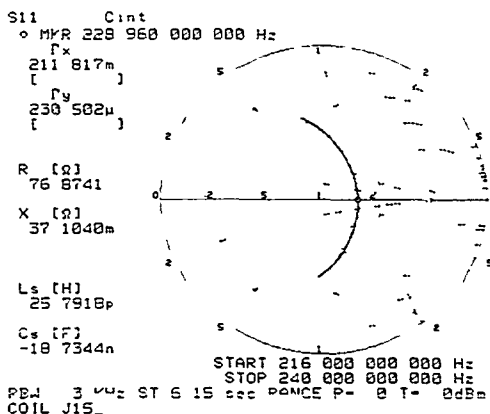
## D.1 References

<sup>1</sup>Murata Erie North America, Inc., 2200 Lake Park Drive, Smyrna, GA.

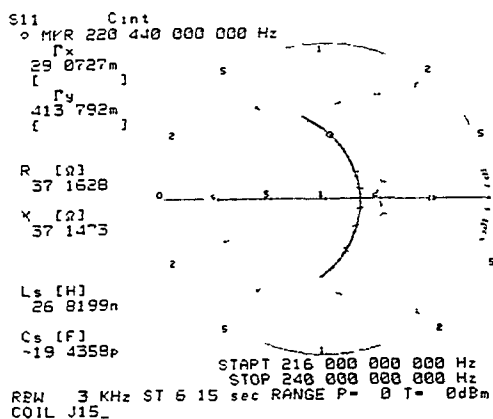
Figure D.1 S<sub>11</sub> for Coil J19.



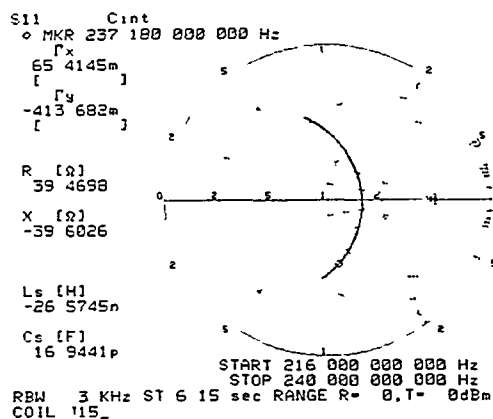
(a)



(b)



(c)



(d)

Figure D.2 S<sub>11</sub> for Coil J15: (a) L, (b) f<sub>res</sub>, (c) f<sub>lower</sub>, (d) f<sub>upper</sub>.

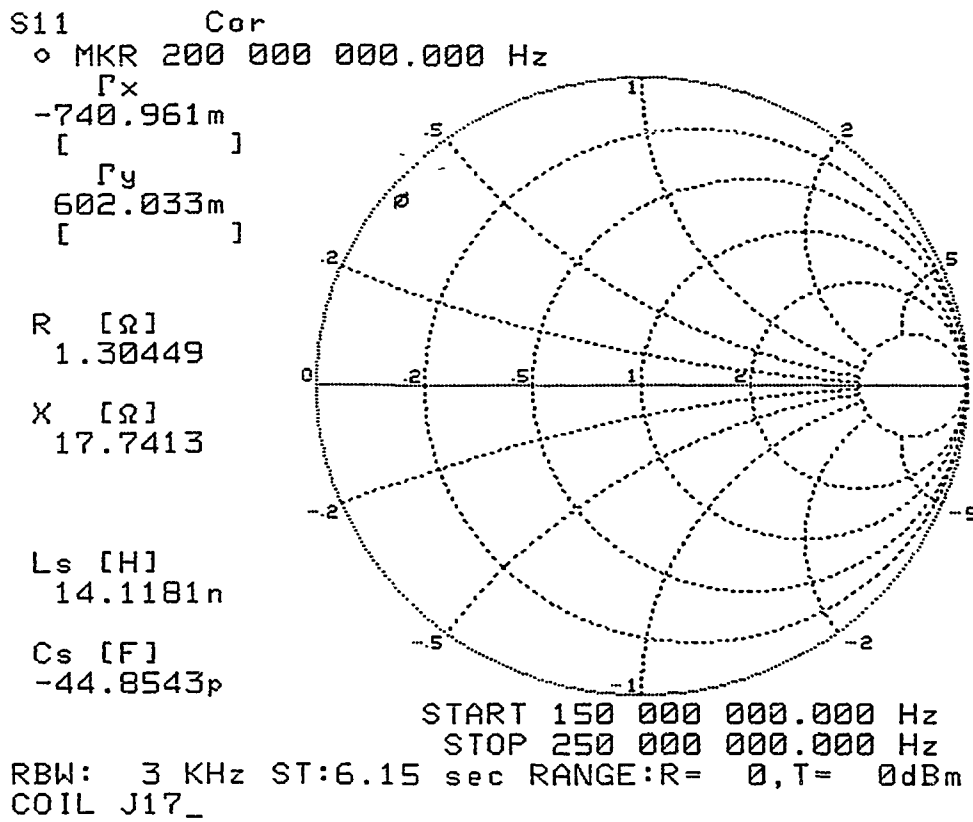
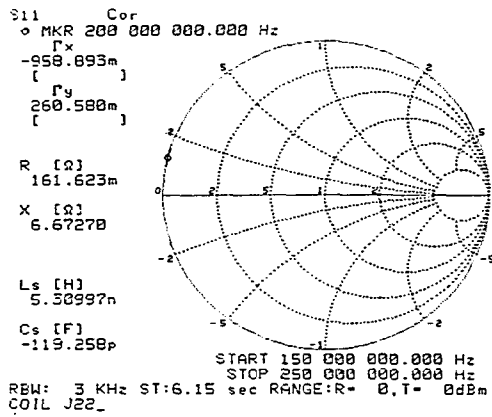
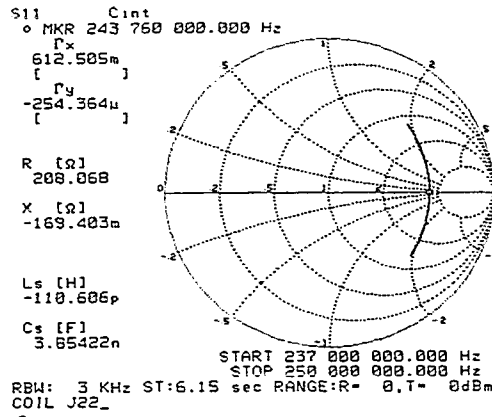


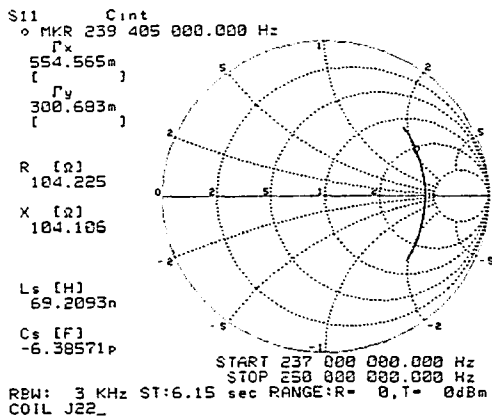
Figure D.3 - S<sub>11</sub> for Coil J17.



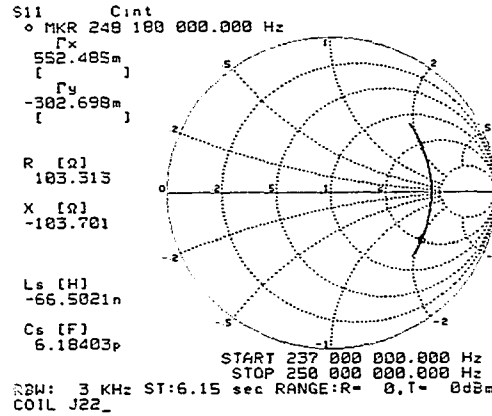
(a)



(b)

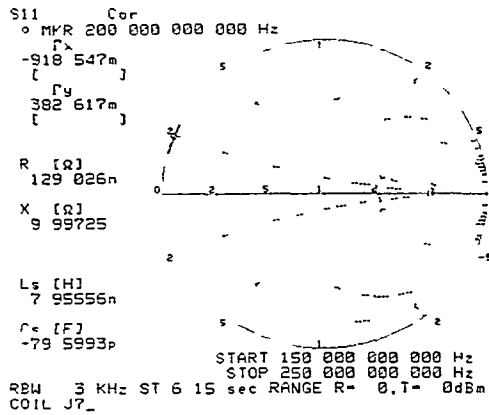


(c)

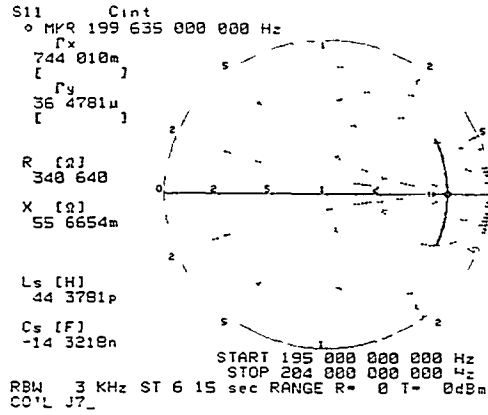


(d)

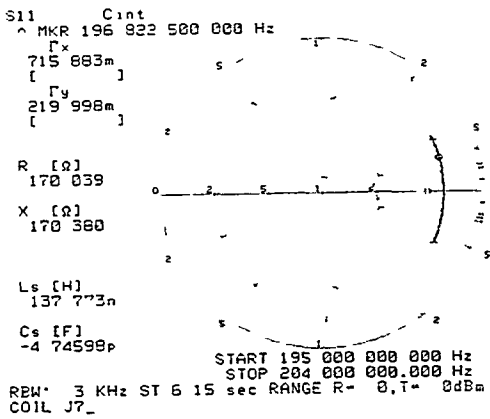
Figure D.4  $S_{11}$  for Coil J22: (a) L, (b)  $f_{res}$ , (c)  $f_{lower}$ , (d)  $f_{upper}$ .



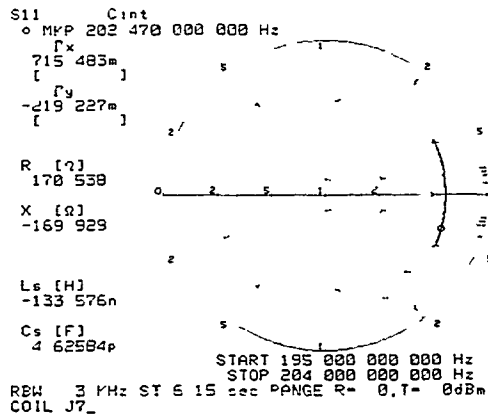
(a)



(b)

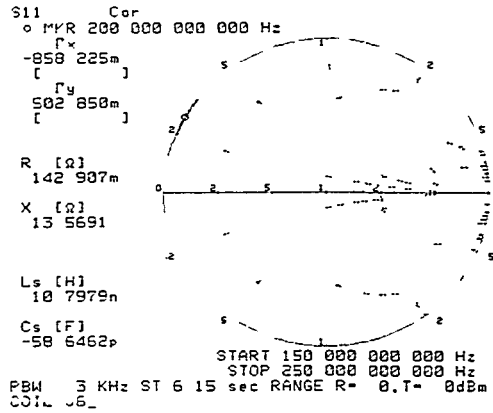


(c)

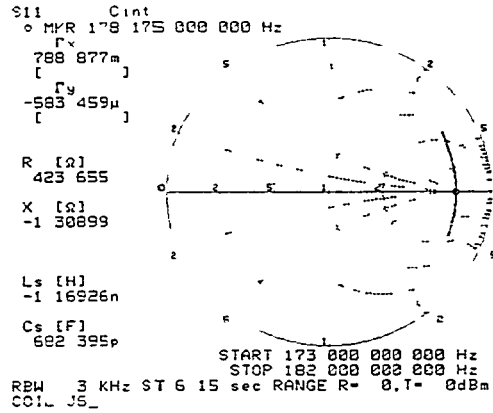


(d)

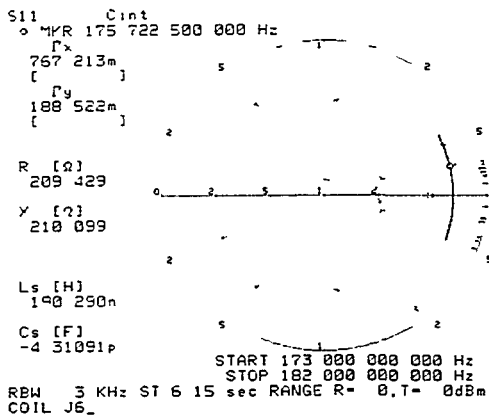
Figure D.5 S<sub>11</sub> for Coil J7: (a) L, (b) f<sub>res</sub>, (c) f<sub>lower</sub>, (d) f<sub>upper</sub>.



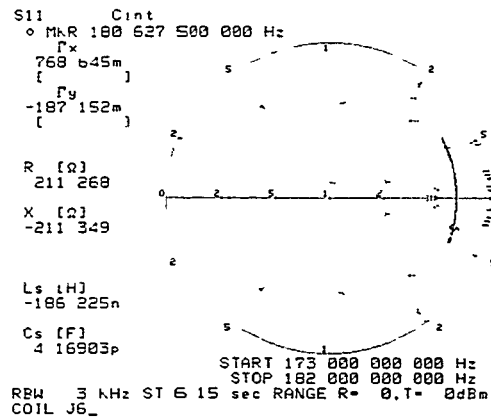
(a)



(b)

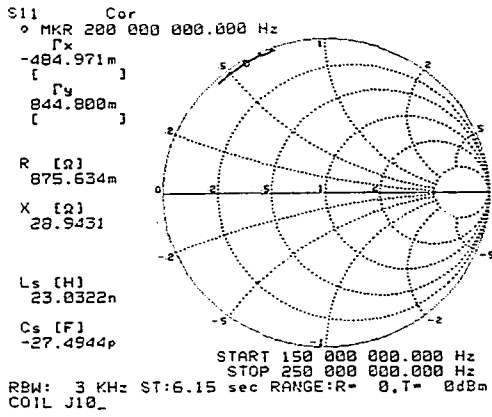


(c)

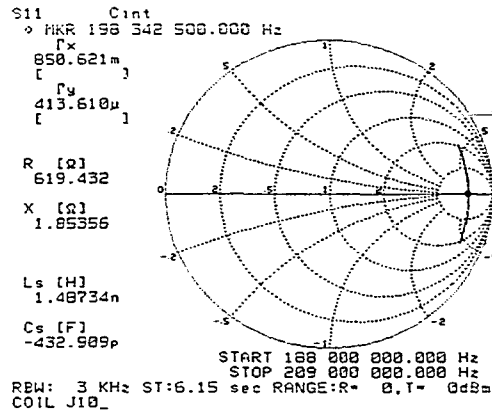


(d)

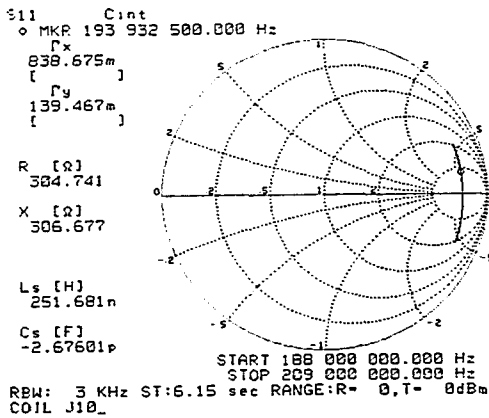
Figure D.6  $S_{11}$  for Coil J6: (a) L, (b)  $f_{res}$ , (c)  $f_{lower}$ , (d)  $f_{upper}$ .



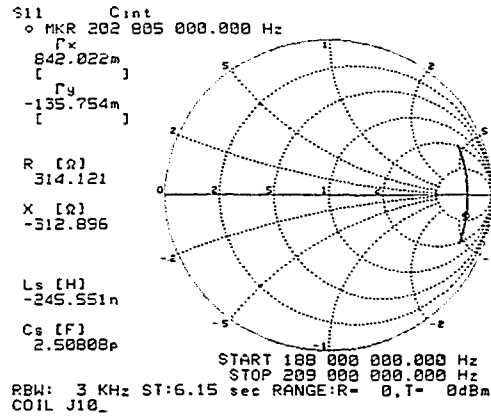
(a)



(b)

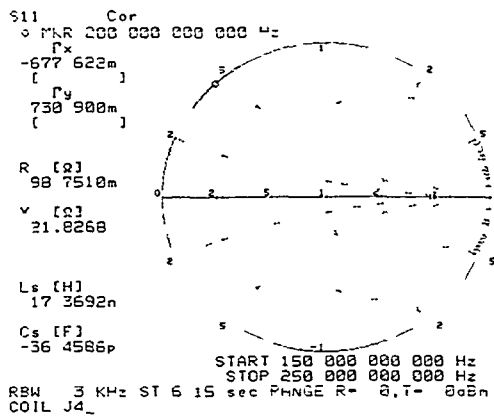


(c)

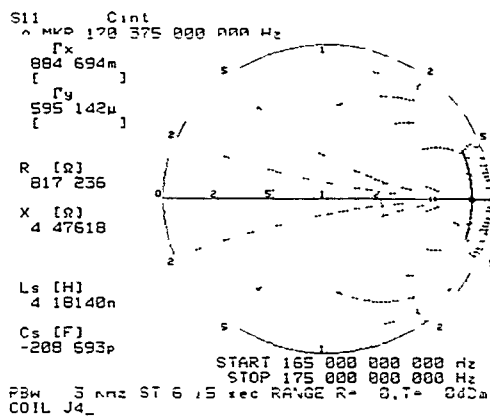


(d)

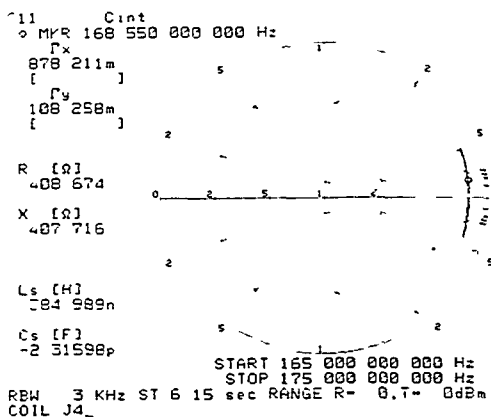
Figure D.7 S<sub>11</sub> for Coil J10: (a) L, (b) f<sub>res</sub>, (c) f<sub>lower</sub>, (d) f<sub>upper</sub>.



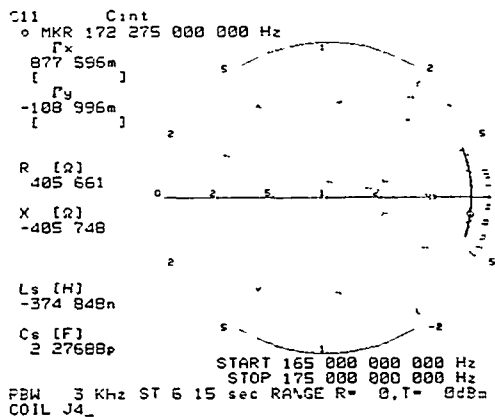
(a)



(b)



(c)



(d)

Figure D.8  $S_{11}$  for Coil J4: (a)  $L$ , (b)  $f_{res}$ , (c)  $f_{lower}$ , (d)  $f_{upper}$ .

## VITA

Timothy Peck was born on June 28, 1963, in Chambersburg, PA. He attended Rochester Institute of Technology in Rochester, NY, from which he received a Bachelor of Science degree in Electrical Engineering (1986) with high honors. A scholarship from Landis Tool Company, Waynesboro, PA, provided financial assistance for his education as well as summer and co-operative education employment. Additionally, he was employed as a co-operative education student by Hewlett-Packard Company for a total period of two years, the majority of which was spent in the RF and microwave products division as a design engineer. He attended the University of Illinois at Urbana-Champaign from 1986 to 1992. While at the University he received a Master of Science degree in Electrical Engineering (1988), and was a recipient of the Harold Olesen Award for Excellence in Undergraduate Teaching by Graduate Students. He graduated with the Ph.D. degree in Electrical Engineering in 1992.